2016

The Study of a Flame Propagation in a Rectangular Duct with a Locally Stratified Flow-Field

Indika Gallage
University of Windsor

Follow this and additional works at: https://scholar.uwindsor.ca/etd

Recommended Citation

The Study of a Flame Propagation in a Rectangular Duct with a Locally Stratified Flow-Field

By

Indika Gallage

A Thesis

Submitted to the Faculty of Graduate Studies

Through the **Department of Mechanical, Automotive and Materials Engineering**

In Partial Fulfillment of the Requirements for the Degree of Master of Applied Science at

the University of Windsor

Windsor, Ontario, Canada

2016

The Study of a Flame Propagation in a Rectangular Duct with a Locally Stratified Flow-Field

by

Indika Gallage

APPROVED BY:

_____

Dr. Randy Bowers

Department of Mechanical, Automotive and Materials Engineering

_____

Dr. Vesselina Roussinova

Department of Mechanical, Automotive and Materials Engineering

_____

Dr. Andrzej Sobiesiak, Advisor

Department of Mechanical, Automotive and Materials Engineering

Nov 25, 2016

DECLARATION OF CO AUTHORSHIP AND PREVIOUS PUBLICATIONS

I. Co- Authorship Declaration

I hereby declare that this thesis incorporates material that is result of joint research, as follows:

This thesis also incorporates the outcome of a joint research undertaken in collaboration with Zakaria Movahedi, Xisheng Zhao and Dale Haggith under the supervision of professor Andrzedj Sobiesiak. The collaboration is covered in Chapters 4, 5, 6 and 7 of the thesis. In all cases, the key ideas, primary contributions, experimental designs, data analysis and interpretations, were performed by the author, and the contribution of co-authors was primarily through the provision of reviewing the material and by providing advice on improving the ideas to be conveyed.

I am aware of the University of Windsor Senate Policy on Authorship and I certify that I have properly acknowledged the contribution of other researchers to my thesis, and have obtained written permission from each of the co-author(s) to include the above material(s) in my thesis.

I certify that, with the above qualification, this thesis, and the research to which it refers, is the product of my own work.

II. Declaration of Previous Publications

This thesis includes three original conference papers that have been previously published in conference proceedings

Thesis Chapter	Publication title/full citation	Publication status*
Chapter 4,5&7	*Gallage I, Mohavadi Z, Zhao X, Haggith D., Sobiesiak A. Investigation of the premixed flame propagation across the varied Composition Field on a Rectangular Duct. Proceedings Combustion Institute Canadian Secretion, University of Windsor, Ontario, Canada: 2014*	*Published and presented - Conference Paper*
Chapter 4,5&7	Gallage I, Sobiesiak A, Mohavadi Z. Flame Propagation in a Rectangular Duct Filled with Stratified Air and Fuel Mixtures. Proceedings Combustion Institute Canadian Section, University of Saskatchewan, SK, Canada: 2015	*Published and presented - Conference Paper*

| Chapter 4,5,6&7 | Gallage I, Mohavedi Z, Sobiesiak A. The effect of stratification on the 1st inversion of a Premixed Flame Propagating in a Rectangular Duct. Proceedings Combustion Institute Canadian Section., University of Waterloo, ON, Canada: 2016. | *Published and presented - Conference Paper* |

I certify that I have obtained a written permission from the copyright owners to include the above-published materials in my thesis. I certify that the above material describes work completed during my registration as a graduate student at the University of Windsor.

I declare that, to the best of my knowledge, my thesis does not infringe upon anyone's copyright nor violate any proprietary rights and that any ideas, techniques, quotations, or any other material from the work of other people included in my thesis, published or otherwise, are fully acknowledged in accordance with the standard referencing practices. Furthermore, to the extent that I have included copyrighted material that surpasses the bounds of fair dealing within the meaning of the Canada Copyright Act, I certify that I have obtained a written permission from the copyright owners to include such materials in my thesis.

I declare that this is a true copy of my thesis, including any final revisions, as approved by my thesis committee and the Graduate Studies office, and that this thesis has not been submitted for a higher degree to any other University or Institution.

ABSTRACT

This work reports on an experimental investigation of a flame propagating through a propane-air mixture in a rectangular duct where the ignition end is kept shut. Flame propagation through a homogeneous charge with equivalence ratios 0.8, 0.9, 1.0 and 1.1 was investigated initially. The flames were tested with the exit end fully open and fully closed. In all the cases, propagation of the flame occurs through a series of acceleration and deceleration periods. This movement was termed the "Leap Frog" phenomenon. The flame develops a shape called the "tulip flame" at the first period and "flame inversions" during the subsequent periods. The formation of the tulip flame and inversions occur right after the acceleration period in a sequence, suggesting that the Leap Frog phenomenon is influenced by the Rayleigh–Tayler (R-T) instability. Flame images of the tulip flame occurrence are qualitatively similar to the interface evolution of two fluids during the R-T instability. The pressure variation at the ignition end of the duct correlates well with the tulip and inversion formations; with a peak pressure at the inversions and tulip flame formation positions. The pressure was filtered with a low pass filter of 25Hz. This frequency is less than the first harmonic of the longitudinal acoustic frequency of the duct, suggesting that acoustic pressure oscillations do not heavily influence the Leap Frog phenomenon.

Next, the flame propagating through a stratified medium, was examined (initial equivalence at 1.1) for the open–exit end condition. Stratification was achieved by air and propane injections to the duct. Also, a mixture the same as the initial charge was injected to the propagating flame to identify effects of pure flow perturbation. Large quantities of air, fuel and mixture were injected when the flame front was within 200 mm from the injector. The flames extinguished at the first inversion for fuel injections of more than 34.6 mg, while the tulip flame position was unchanged. However, for air injections of more than 37 mg, the flames did not extinguish and the tulip flame position was displaced downstream. The flame behavior was similar to large air injections with mixture injections. However, a threshold mass of mixture could not be determined. The tulip flame was displaced when the flames were within 100 mm from the injector at the start of injection. When less than 34.6 mg of fuel and less than 37 mg of air were injected, the tulip flame was not displaced nor did the flames extinguish; but the position of the first inversion shows a good correlation with the injection timing. These experiments suggest that the flame propagation reverts to the "Leap Frog" phenomenon irrespective of extreme stratification and heavy perturbations, suggesting a single dominating factor influencing the formation of the tulip flame and inversions in all of these extreme conditions. It is postulated that the R-T instability is this factor.

DEDICATION

This MASc thesis

is dedicated

to the people who share their valuable knowledge

gained through hard work.

ACKNOWLEDGEMENTS

TABLE OF CONTENTS

LIST OF FIGURES

LIST OF TABLES

LIST OF ABBREVIATIONS

BNC   Bayonet Neill–Concelman (a connection type)

CCD   Charge Coupled Device

CIS   Calibration input sensitivity of Amplifier [mV/pC]

DAQ   Data Acquisition

DNS   Direct Numerical Simulations

FPD   Flame Propagation Duct

FPS   Frames Per Second

LES   Large Eddy Simulation

LIS   Laser Induced Florescence

PIV   Particle Image Velocimetry

RANS   Reynolds Averaged Navier Stoke's Equation

SLPM   Standard Liters Per Minute

SLPS   Standard Liters Per Second

SMLPS   Standard Millie Liters Per Second

STP   Standard Temperature and Pressure

R-T   Rayleigh - Taylor

TTL   Transistor-Transistor Logic (A pulse type)

$(\dot{Q}/V)_{cal}$ Calibration coefficient for the NI DAQ Assistant (flow meter)

$[AFR]_s^{Vol}$ Volumetric Air to Fuel Ratio at Stoichiometry (when the exact number of fuel and air are involved in the reaction).

$[AFR]^{Vol}$ The volume ratio of Air to Fuel of an oxidation reaction

$[FAR]_s^{Vol}$ Volumetric Fuel to Air Ratio at Stoichiometry (when the exact number of fuel and air are involved in the reaction).

$[FAR]^{Vol}$ The volume ratio of Fuel to Air of an oxidation reaction

NOMENCLATURE

Symbol	Description	Units if applicable
	English Letters	
A	An imperial constant which is approximated to 1/3	
a	Acceleration	m/s^2
C_0	the speed of sound (or pressure wave)	
CIS	Calibration input sensitivity of Amplifier	mv/Pc
C_p	Heat Capacity at Constant Pressure	
D_F	Final Distance at the end of time interval t	mm
D_I	Initial Distance at start of time interval t	mm
D_{th}	Thermal Diffusivity	m^2/s
e	Energy	J
E	Gas expansion coefficient ($\rho u/\rho b$)	
e_1	Instrument error #1	
$E1,2$	The mean efficiency with which body 2 transfers energy to body 1	
f	The resonant frequency of the modes nx, ny and nz	
f_{12}	Fluidity (the inverse of Dynamic Viscosity)	1/P
h	Enthalpy	J
h_k	Enthalpy of k	J
h_s	Sensible Enthalpy	J
I	Turbulent Intensity	
k	The kinetic energy of the flow.	
K	Wavenumber of the perturbation	
L_{calc}	Calculated sample length using the scale	mm
Le	Lewis number	
L_{pix}	The sample number of pixels to calculate the length and error.	Pixels
l_t	The integral length scales of a turbulent flow.	
LT_{mm}	Actual Length for calibration of image	mm
LT_{pix}	Some pixels between two points of known displacement.	Pixels
lx	Width of the tube	
ly	Height of the tube	
lz	Length of the tube	
m_1	Mass of body m1	g
m_2	Mass of body m2	g
M_{air}	Molar Mass of Air	kg/Kmol or g/mol

Symbol	Description	Units if applicable
M_i	Molar Mass of component i	g/mole or kg/kmol
m_{inj}	mass injected	mg
n_a	A number of Air Molecules.	mole
n_f	A number of Propane Molecules.	mole
nx	Oscillating modes in the x direction	
ny	Oscillating modes in the y direction	
nz	Oscillating modes in the z direction	
P1	Static Pressure at the Inlet	N/m2
P2	Static Pressure at the outlet	N/m2
P_a	Partial Pressure of Air.	bar
P_f	Partial Pressure of Fuel.	bar
p_i	Momentum fraction	
P_T	Total pressure.	bar
Q	Heat of reaction	
Q	Volumetric Flow Rate	m3/s
$\dot{Q}_1$	Smallest flow of calibration	SMLPS
$\dot{Q}_2$	Largest flow of calibration	SMLPS
q_i	Heat Flux	
r	Radius of the restriction	m
R	Universal Gas constant	8.317 x 10^3 J/kg/Kmol/K
Re(r)	Reynolds number in a flow with eddy size, r	
Re_k	Reynolds number in a flow corresponding to the Kolmogorov scale.	
Re_t	Turbulent Reynolds number	
R_r	Reaction Rate	s^{-1}
S	Selected Scale	mv/bar
S_a	Absolute Speed	
S_c	Consumption Speed	
SC	Scale used in image processing	mm/Pixel
S_d	Displacement Speed	
S_L	Laminar Flame Speed	m/s
ST	Sensitivity of Transducer	Pc/Bar
t	Time	s
T	Temperature	
t	Time	S
t	Time interval	ms
t sphere	Time taken for the flame to form a spherical shape in the duct	s

Symbol	Description	Units if applicable
t_{Tulip}	Time taken to start the formation of the tulip flame	s
t_{Wall}	Time taken for the flame to reach the walls of the duct	s
u	Velocity	m/s
U_ρ	Uncertainty of density	Kg/m^3
$U_{(Q/V)cal}$	Uncertainty of calibration coefficient for the NI DAQ Assistant (flow meter)	SLPM/V
$u'(r)_{rms}$	The characteristic RMS velocity of motion of eddy size, r	
U_0	Zero Order Uncertainty	
U_{CIS}	Uncertainty of CIS	%
U_D	Design Stage error	
U_{D10V}	Design Stage error of NI DAQ card for 10V	mV
U_{D5V}	Design Stage error of NI DAQ card for 5V	mV
U_{D5v}	Design Stage uncertainty of NI6035 -5V	V
U_{DAmp}	Design Stage error of Kistler dual mode amplifier	mV
U_{DF}	Uncertainty of Distance measurement for DF	mm
U_{DI}	Uncertainty of Distance measurement for DI	mm
u_i	Velocity in the direction i	m/s
U_{Lcalc}	Uncertainty of the calculated distance from image processing	mm
U_{Lmm}	Uncertainty of actual length measurement	mm
U_{Lpix}	Uncertainty of the pixel count	Pixels
U_m	Uncertainty of mass injected	mg
U_{pa}	Error of reading the partial pressure of air	Psi
U_{pf}	Error of reading the partial pressure of fuel	Psi
u_{Q1}	Overall Uncertainty of flow rate Q1	SMLPS
u_{Q2}	Overall Uncertainty flow rate Q2	SMLPS
U_S	Uncertainty of S	%
U_{SC}	Calculated Uncertainty of the scale used in image processing	mm/Pixel
U_{ST}	Uncertainty of transducer sensitivity at full scale	%
U_t	Assume zero	S
$U_{V(D1-D2)}$	Uncertainty of calculated velocity	m/s
u_{V1}	Overall Uncertainty voltage V1	V
u_{V2}	Overall Uncertainty voltage V2	V
v'	Fluctuating velocity of a turbulent flow	
$\bar{v}$	Mean velocity of a turbulent flow.	
$V_{(D1-D2)}$	Mean Velocity at time t	m/s

Symbol	Description	Units if applicable
V_1	Voltage for $\dot{Q}1$	V
V_2	Voltage for $\dot{Q}2$	V
V_{5v}	Voltage reading of LabVIEW DAQ card	V
V_{ki}	Diffusion Velocity of k in the direction i	m/s
xi	Mole fraction of component i	
y_k	Mass fraction of kth element	
Y_F	Fuel mass fraction	
Z_{tip}	The distance of the flame tip from the point of ignition	m

Greek Letters

Symbol	Description	Units if applicable
α	Atwood Number	
$\varDelta$	Delta Operator.	
δ	Flame thickness	μm
ε	The dissipation of energy	
η	Absolute or Dynamic Viscosity of the Fluid	Ns/m^2 =10 Pois (P)
η12	Dynamic viscosity of the mixture of substance 1 and 2	Ns/m^2 =10 Pois (P)
η_{Air}	Dynamic or Absolute Viscosity of air.	Ns/m^2 =10 Pois (P)
η_k	Kolmogorov scales	
$\eta_{mixture}$	Dynamic or Absolute Viscosity of the premix with a known Φ.	Ns/m^2 =10 Pois (P)
$\eta_{Propaner}$	Dynamic or Absolute Viscosity of Propane.	Ns/m^2 =10 Pois (P)
K	Strain	(m^2/m^2)
κ	Flame stretch	s^{-1}
λ	Thermal Conductivity	w/m.K
ν	Flow kinetic viscosity	m^2/s
ρ	Density	Kg/ m^3
ρ_b	Density of Products (burnt gasses)	Kg/ m^3
ρ_u	Density of reactants (Undernet charge)	Kg/ m^3
σ	Density ratio of unbent to burnt ρu/ρb	
τ_{ij}	Viscous stress	N/m2
Φ	Equivalence Ratio.	
$\dot{\omega_T}$	Heat release Term	

CHAPTER 1

1. INTRODUCTION

1.1. MOTIVATION

The investigation of flames propagating through stratified mixtures is required to understand and improve some combustion devices. In these devices, a stratified charge is desirable or unavoidable in operation. In reciprocating engines, flame propagation through a stratified charge has attracted attention in the direct injection stratified charged engine (DISC) and the direct injection spark ignition (DISI) engine. The stratification of charge in a spark ignited engine contributed to the reduction of emissions and fuel consumption [1,2]. The reduction of soot and NO_x while maintaining high fuel efficiencies at part load conditions is achieved through stratification in HCCI engines. These HCCI engines use charge stratification as a solution to control and power challenges [3]. Stratification is unavoidable for the operation in some combustion devices. For instance, with the requirement of air cooling through the liner or flame tube of a gas turbine, the stable operation throughout a wide range of air-fuel ratios (a stratified medium) is required [4]. The understanding of flame propagation through a stratified medium by fundamental studies will help understand more complex situations found in practical combustion devices.

1.2. OBJECTIVE

- Investigate various flame propagation patterns and flame configurations for flames propagating in a rectangular duct;
    - When the medium is homogeneous with equivalence ratios of 0.8, 0.9, 1.0 and 1.1 to determine a base case for stratification.
    - When the medium is stratified.
- Understand the flame propagation under each condition based on the experimental results obtained.

1.3. STRATEGY

The stratification along the duct is achieved by injecting air or fuel to the duct using gaseous injectors.

The duct used for the present work had a cross section of 25mm x 50mm and length of 1840mm and shown in Fig. 1. It is fitted with a spark plug at one (closed) end and injecting nozzles located
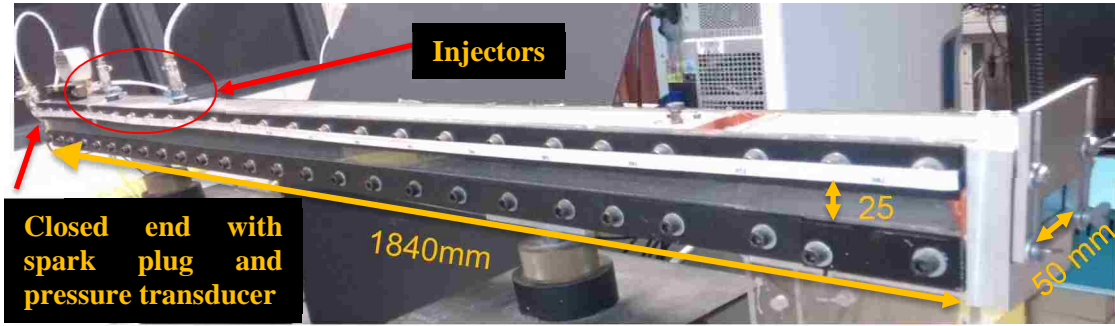
Fig. 1: Image of the flame propagation duct

at 300mm and 600mm from the spark end to create stratification along the duct. The duct is fitted with transparent windows on its two sides of 25mm height for the traveling flame to be visible.

A high speed-imaging camera (CCD) is used to capture the images of the flame moving through the duct. An image processing software (ProAnalyst) is used to process and interpret the images captured. A LabVIEW program is used in conjunction with a data acquisition (DAQ) card to trigger the ignition electrodes, injectors and the CCD.

A pressure transducer captures the pressure variation at the ignition end, during the flame travel. A flow meter upstream of the injector is used to record the mass of air or fuel injected. The capturing of data is triggered using the LabVIEW program. The program enables the synchronization of data capturing with the ignition and injection.

The analysis of reacting flows is quite complex and almost impossible to predict when the reacting flows are turbulent. The findings of the thesis are intended to provide more understanding of the reacting flow through a rectangular duct. In this work the jumping motion of the propagating flame or the "Leap Frog"[5] pattern and the formation of the " Tulip-Flame "[6] and subsequent inversions in a stratified as well as in a homogeneous medium are investigated. The flame propagating patterns and the details of the formation of the tulip flame and inversions are used to explain the effects of stratification.

CHAPTER 2

2. ON LAMINAR AND TURBULENT FLAMES

2.1. REACTING FLOWS

A flame propagating through a duct is a reacting flow problem. A reacting flow may consist of all the characteristics of fluid flow, as well as of reactions taking place between flowing reactants. The reactions (combustion) affect the flow and the reactions taking place are in turn affected by the flow. This thesis is mainly focused on gaining an understanding of the reacting flow, through experiments. Methods of theoretically analyzing the flame propagation, the definition of certain important parameters, instabilities and a brief account of how a flame is computationally simulated are discussed. The flame propagation considered in this work behaves as laminar and turbulent premixed flames. Fig. 2 shows images of the flame at 20 ms from its start, when it resembles a laminar flame structure; whereas at 40.1 ms it shows a turbulent structure. Details of both regimes are presented.
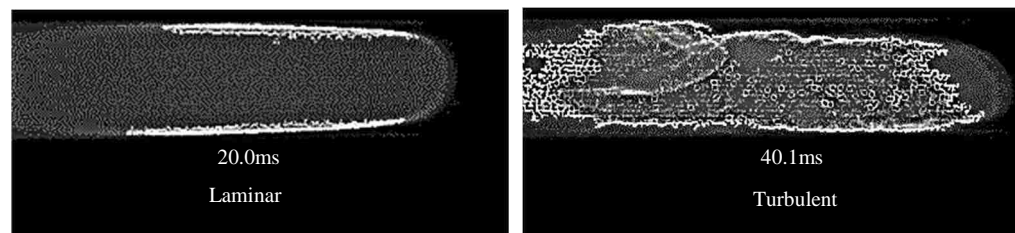
Fig. 2: Laminar and turbulent flame shapes during the propagation of the flame

2.2. LAMINAR AND PREMIX FLAMES

A premixed flame propagating inside a duct starting from a medium at rest may have characteristics of a laminar premixed flame as well as turbulent premixed flame. The analysis of laminar premixed flames is relatively easy, compared to turbulent premixed flames. The comparison between experiments, theory and computation can be performed quite easily in a laminar premixed flame. When the flow is turbulent, the conditions become complex and random. One main way of analyzing such flows is to compare experimental results with computational results. This thesis provides experimental findings of the reacting flow, which can be used to compare and enhance simulations of reacting flows. Governing equations and a brief account of numerically studying laminar premixed flames is presented in Appendix - B

2.2.1. Analytical Study of a Laminar Premixed flame

With the assumptions below and using equations for burnt product temperature by equation (1), flame thickness by equation (2), flame speeds by equation (3), the 1-D flame configuration in Fig. 3 is derived [7].

Assumptions:

- A single step reaction
- Reaction rate depends only on the fuel mass fraction (using a very lean mass fraction)
- Using Fick's Law
- C_p Constant (not dependent on T)
- Lewis Number (Le) =1

Flame Structure

The traveling flame at the laminar flame speed could be graphically illustrated as in Fig. 3 [8]. The reaction rate spikes at the flame front; the flame travels into the fresh gas. In Fig. 3 the sharp temperature rise at the flame front causes the increased temperature in the burnt gas. The fuel and the oxidizer are consumed at the flame front. The burnt gas will have a lower density and will need to expand into the fresh gas area if this was a flame traveling in a tube closed at the ignition end.
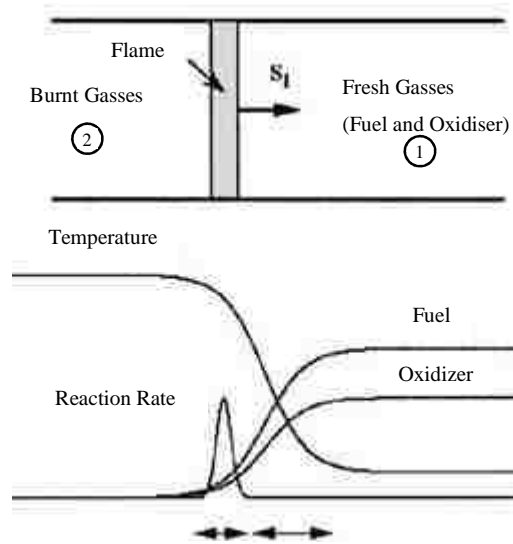
Fig. 3: Structure of laminar plane premixed flames; modified image published in [7]

Burn Gas Temperature (T2)

The initial and final temperature T_1 and T_2 are the temperature of the fresh gas and the temperature of the burnt gas in Fig. 3 .The relationship between T1 and T2 are formulated as equation (1) below [7] (assuming that the mixture is lean). This relationship shows that the final temperature depends on the fuel mass fraction (Y_F) and heat capacity (C_p.)

$$T_2 = T_1 + \frac{QY_F}{C_p}$$

(1)

$Q = Heat\ of\ reaction$

$C_p = Heat\ Capacity\ const\ pressure$

$Y_F = Fuel\ Mass\ Fraction$

Flame Thickness (δ).

The flame thickness is the space where the reactions rates are the highest; physically it is a thin sheet where the combustion reactions take place, which we identify as the flame front. Equation (2) shows a simplified expression for flame thickness (δ) and Laminar Flame speed (S_L). By using matched asymptotic expansions by changing variables for temperature and fuel mass fractions and using the Echekki Ferziger simplification[9,10]

(2)

$$\delta = \frac{D_{th}}{S_L}$$

Where

D_{th}= thermal diffusivity (m^2/s)

S_L = laminar flame speed (m/s).

Flame Speeds (S_L).

$$S_L = \frac{1}{\beta}\sqrt{R_r D_{th}}$$

(3)

Where β is a constant, $R_r(s^{-1})$ is the reaction rate and D_{th} (ms^{-1}) is the thermal diffusivity. Though these expressions are derived through assumptions, the author mentions that the physics will resemble an actual scenario [7]. Understanding the physics behind the most vital factors of the

experiment such as the flame speed, flame thickness, and final temperatures is helpful in the investigation of such a flame.

In this study, the flame is ignited from the closed end of the tube and travels towards the opposite end which is opened or closed. The absolute velocity of the flame is affected by the speed at which the flame consumes the unburnt reactants and by the flow generated by the expanding hot gases behind the flame front.

Relationship between displacement speed and absolute speed[7]

In general, we speak about a flame speed, however, to understand flame speed it is necessary to look at the definitions of absolute (S_a), displacement (S_d), and consumption (S_c) flame speeds as in Table 1.

Table 1: Simple classification of flame speeds.

Identification	Definition
Absolute (S_a)	Flame front speed relative to a fixed reference plane
Displacement (S_d)	Flame front speeds relative to the flow
Consumption (S_c)	Speed at which the reactants are consumed
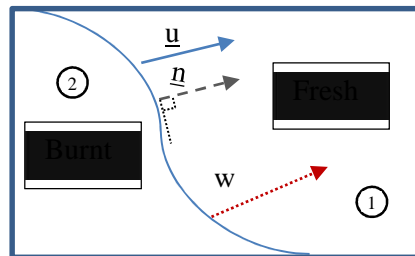
Fig. 4: Flame speed relationships

$$\overline{W} = \overline{U} + S_d.\overline{n}$$

(4)

$$S_a = \overline{W}.\overline{n} = (absolute\ flame\ speed)$$

(5)

$$S_d = (\overline{W} - \overline{U}) . \bar{n} \tag{6}$$

$\overline{W} = Flame\ Velocity$ (Absolute)

$\overline{U} = Flow\ Velocity$

$\bar{n} = unit\ vector\ perpendicular\ to\ the\ flame\ front$

Consumption speed

$$S_c = \frac{1}{\rho_1 Y_F} \int \dot{\omega}_F \, dx \tag{7}$$

Stretch

The consumption speed is given by (7). When the consumption speed "S_c" of the flame is equal to the displacement speed "S_d" of the flame it is called the laminar flame speed "S_L". When "S_d" is greater than "S_c," we say that the flame is stretched.

The following formula gives stretch

$$\kappa = \frac{1}{A} \frac{dA}{dt} \tag{8}$$

Where κ (Greek symbol lower case Kappa) is stretch, A is flame area, and t is time. Stretch means how many times the surface of the flame has increased per unit time. The units of stretch are s^{-1}.

Flame stretch has been derived in terms of strain rate and curvature by Candel and Poinsot[11].

Laminar Flame Speeds of air-fuel mixtures

The maximum laminar burning speed for propane occurs around an equivalence ratio of 1.1, and it is close to 0.35 m/s shown in Fig. 5 derived from [12]. The experiments in this work are carried out with propane-air mixtures with several equivalence ratios to cover rich, lean and stoichiometric air-fuel mixtures. The given speeds above are the consumption speeds when the flame has no stretch, while a stretched-flame will have much higher speeds.
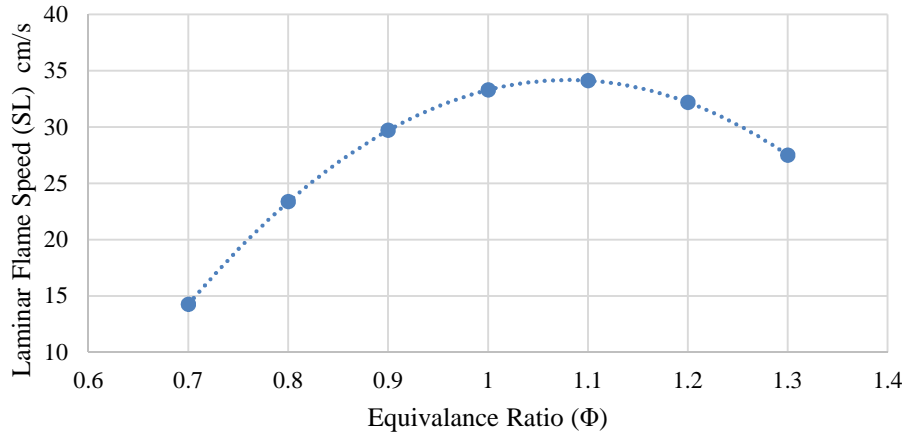
Fig. 5: Laminar burning speeds of propane /air at 300 k and 1 bar

Richard Stone gives an empirical formula for the laminar flame speed of a flame shown in Equation (9) [12].

$$S = B_m + B_\emptyset(\emptyset - \emptyset_m)^2$$

$$(9)$$

S = burning speeds at 300 K, 1 bar

B_m= maximum burning speed

B_ϕ= empirical constant

The graph in Fig. 5 has been plotted using equation (9) with the values given in Table 2 below.

Table 2: Values for equation (17) plotted in graph in Fig. 5 [12]

Fuel	Φ_m	B_m (m/s)	B_Φ(m/s)
Methanol	1.11	0.369	-1.41
Propane	1.08	0.342	-1.39
iso-octane	1.13	0.263	-0.85
Gasoline	1.21	0.305	-0.55

The effect of pressure and temperature on the laminar flame speed is given by equation (10) from Stone. This empirical equation uses the values for m and n from Table 3 [12].

$$\frac{S_L}{S_{L_0}} = \left(\frac{T}{T_0}\right)^m \left(\frac{P}{P_0}\right)^n$$

(10)

Where the subscript 0 denotes the conditions at standard temperature and pressure

Table 3: Effects of pressure and preheat for laminar flame speed for equation (10)[12]

Φ	0.8-1.5
S_L	$34-138(\Phi-1.08)^2$
m (pressure exponent)	$-0.16-0.22(\Phi-1)$
n (temperature exponent)	$2.18-0.8(\Phi-1)$

Relationship between Consumption speed and Absolute speed of a spherical flame

For a spherical flame where the expanding hot gases are trapped inside a flame bubble, the relationship between the absolute speed and the consumption speed can be given as equation (11)[7]

Where ρ is density and T is temparature

$$S_a = \frac{\rho_1}{\rho_2} S_c \backsim \frac{T_2}{T_1} S_c$$

(11)

2.3. TURBULENT PREMIXED FLAMES

A premixed flame is turbulent if the medium ahead of the flame front is turbulent. A flame becomes turbulent when the eddies ahead of the flame start interacting and altering the flame front [9,13]. The flame initiates as a laminar premixed flame; the flow induced disturbances ahead of the flame front create turbulence and thus shows characteristics of a turbulent premixed flame during its propagation along the duct.

Turbulent premixed flames cannot be analyzed using direct and simple methods as in the case of laminar premixed flames, due to the large number of correlations between species concentrations

and temperature fluctuations. Instead, "heuristic" models for turbulent combustion are derived based on physical analysis and various length and time scales.

2.3.1. Fluctuation of properties and turbulent intensity

Turbulence is characterized by the fluctuation of all local properties. For example, the property velocity will have a mean $\bar{v}$ and fluctuation v' (12). The turbulent strength is generally characterized by the turbulent intensity I, given in equation (13).[7,13]

$$u = \bar{u} + u'$$ (12)

$$I = \frac{\sqrt{u'}}{u}$$ (13)

The turbulent intensity itself is not sufficient to describe turbulent combustion.

2.3.2. The relationship of the Reynolds number, Damköhler Number and Karlovitz Number, with length and time scales of turbulent combustion

The largest eddy sizes in turbulent combustion are called the integral scales (l_t), and the smallest eddy sizes relate to the Kolmogorov scales (η_k) which last for a very short time before they dissipate. Length scales indicate the energy of an eddy to interact with the flame front. A Reynolds number Re(r) is introduced for an eddy size, r as

$$Re(r) = \frac{u'(r)_{rms} * r}{\nu}$$ (14)

u'(r)$_{rms}$ is the characteristic RMS velocity of motion related to eddy size, r and ν are the flow kinematic viscosity. But Poinsot and Veynante in 5.2.1 page 207 of [9] warns that "taking u' as the RMS velocity to quantify the velocity fluctuation in a premixed flame has no theoretical basis in a premixed flame. In experiments, u' in a turbulent premixed flame is calculated for the RMS velocities in the fresh gas far from the flame front which is an implicit assumption."

The turbulent Reynolds number Re$_t$ for the integral length scale l_t is given the below formula.

$$Re_t = Re(l_t) = \frac{u'(l_t) * l_t}{\nu}$$ (15)

Energy from larger scales to smaller scales flow through the Kolmogorov cascade [14], which is more commonly known as the energy cascade. The equation (16) [7], gives the dissipation (ε) of the kinetic energy (k).

$$\varepsilon = \frac{u'(r)^2}{(\frac{r}{u'(r)})} = \frac{u'(r)^3}{r} \tag{16}$$

The Reynolds number will have largest value for the integral length scale decreasing to a number close to unity where the inertial forces and the viscous forces will be equal.

This unity Reynolds number is characterized by the Kolmogorov scale which is given by (17) [14].

$$\eta_k = \left(\frac{v^3}{\varepsilon}\right)^{\frac{1}{4}} \tag{17}$$

The Reynolds number corresponding to a unity Reynolds number is given by (18), using (17) and (16).

$$Re_K = \frac{u'(\eta_k) * \eta_k}{v} = \frac{\varepsilon^{\frac{1}{3}} * \eta_k^{\frac{4}{3}}}{v} = 1 \tag{18}$$

Using (15),(16) and (17) the ratio of the integral scale to the Kolmogorov scale is given as (19)

$$\frac{l_t}{\eta_k} = \frac{\frac{u'^3}{\varepsilon}}{\left(\frac{v^3}{\varepsilon}\right)^{\frac{1}{4}}} = \frac{u'^3}{v^{\frac{3}{4}} * \varepsilon^{\frac{3}{4}}} = \frac{u'^3}{v^{\frac{3}{4}} * \left(\frac{u'^3}{l_t}\right)^{\frac{3}{4}}} = \frac{u'^{\frac{3}{4}}}{v^{\frac{3}{4}} * l_t^{\frac{3}{4}}} = Re_t^{\frac{3}{4}} \tag{19}$$

2.3.3. The Relationship of strain with length and time scales of combustion[7]

Strain is directly related to the velocity gradient in the strain term. Strain is denoted by the upper case Greek letter Kappa "K". Strain K=K(r) induced by an eddy of size, r is assumed to scale with a factor of u'(r)/r to arrive at (20).

$$K(r) = \frac{u'(r)}{r} = \left(\frac{\varepsilon}{r^2}\right)^{\frac{1}{3}} \tag{20}$$

The characteristic time τ_m scale of the eddy size, r is given by

$$\tau_m(r) = \frac{r}{u'(r)} = \frac{1}{K(r)} \tag{21}$$

The strain, relating to the Kolmogorov and integral scales are given by.

$$\kappa(\eta_k) = \sqrt{\frac{\varepsilon}{v}} \tag{22}$$

11

$$\kappa(l_t) = \frac{1}{k} \tag{23}$$

Where k in (23) is kinetic energy or $(u'(r))^2$.

The strain of integral and Kolmogorov scales are related to the turbulent Reynolds number by (24)

$$\frac{\kappa(\eta_k)}{\kappa(l_t)} = \sqrt{Re_t} \tag{24}$$

The Damköhler number is defined as the ratio of the mechanical time scale τ_m of a large eddy with the integral length (l_t) to the chemical time scale τ_c[13]

$$Da = \frac{\tau_{m_{l_t}}}{\tau_c} \tag{25}$$

The Karlovitz number is defined as the ratio of the chemical time scale τ_c to the mechanical time scale of an eddy in the Kolmogorov scale [13].

$$Ka = \frac{\tau_c}{\tau_{m_{\eta_k}}} \tag{26}$$

2.3.4. Understanding Premixed Turbulent Flames using Different Regimens

For a flame to be turbulent Re_t >1 is the minimum criteria, while in practical combustion devices this number varies from 100 to 2000 [9,13] .

Turbulent combustion regimes were identified by Borghie in 1985 [15], Peters in 1986 [16] and enhanced by Borghie and Destriau [17].Fig. 6 from [8] shows the regimes further explained by Veynante. The regimes identified are wrinkled, thickened wrinkled, and thickened flames. The definitions of the thin-wrinkled, thickened-wrinkled and thickened-flame regimes are described below. [9,8,13].

Flamelet regime – For large Da ($\gg$1) the flame front is thin, its inner structure is not affected by turbulent motion, eddies only wrinkle the flame surface. This regime occurs when the Kolmogorov turbulent scales or the smallest turbulent scales have a turbulent time τ_K which is larger than that of τ_c. The smaller turbulent eddies are slower than the chemical time for the reactions to happen.

Thickened wrinkled flame –Turbulent motions can affect and thicken the preheat zone but cannot modify the reaction zone, which remains thin and close to laminar.

Thickened flame or well-stirred reactor – Preheat and reaction zones are strongly affected by turbulent motion no laminar flame structure is identified.
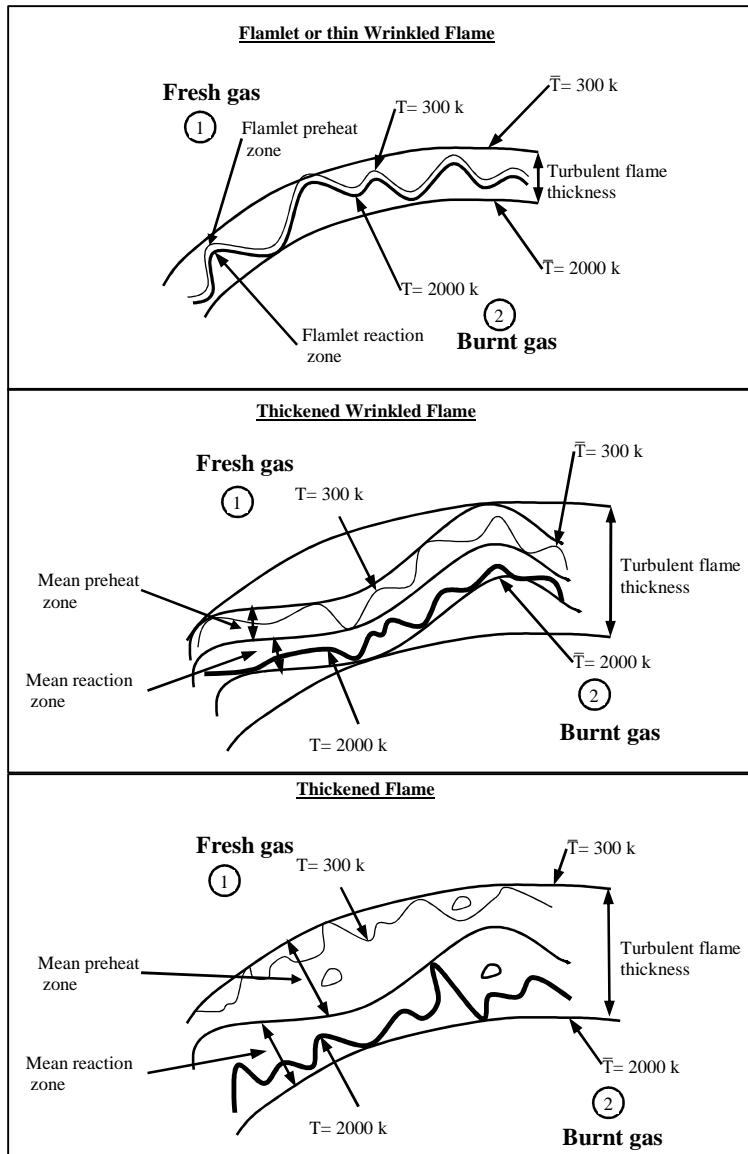
Fig. 6: Turbulent premixed combustion regimes modified diagram using modified image published in [8]

Fig. 7 [9] shows a combustion diagram where the combustion regimes are identified at different turbulence scales normalized by the flame thickness. The y-axis shows the non-dimensional eddy velocity. The x-axis shows non-dimensional length scale of the integral eddy size. Practical references of Fig. 7 are presented in Fig. 8 [9]. The diagram indicates what turbulent regimes can be expected in a practical combustion application. For instance, it can assumed that the flame propagation in a duct is close to the operating region of an IC engine but more towards the laminar region. In Fig. 2 initially the flame is laminar and should be present in a larger area (dotted triangle in Fig. 8) where $Re_t<1$ than for a piston engine, and a small region (striped triangle in Fig. 8) where $Da>1$ compared to a piston engine. The dotted rectangular box in Fig. 8 shows a possible region in the diagram for the flame propagation in the duct considered in this study.
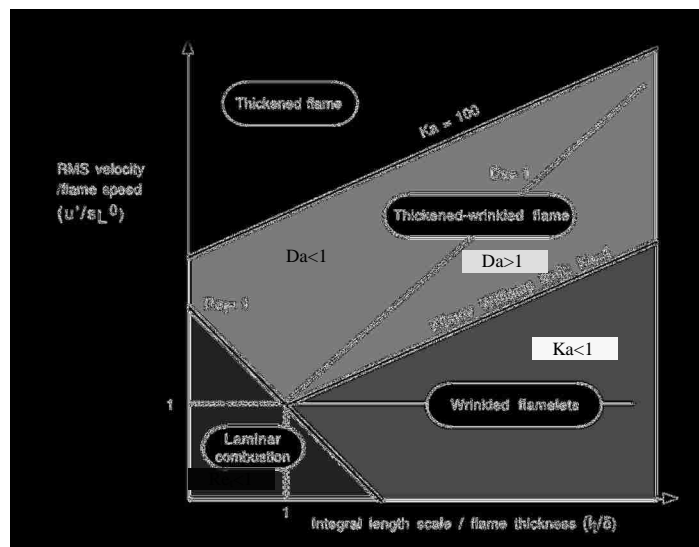
Fig. 7: Turbulent combustion regimes as a function of non-dimensional numbers; image published in [9]
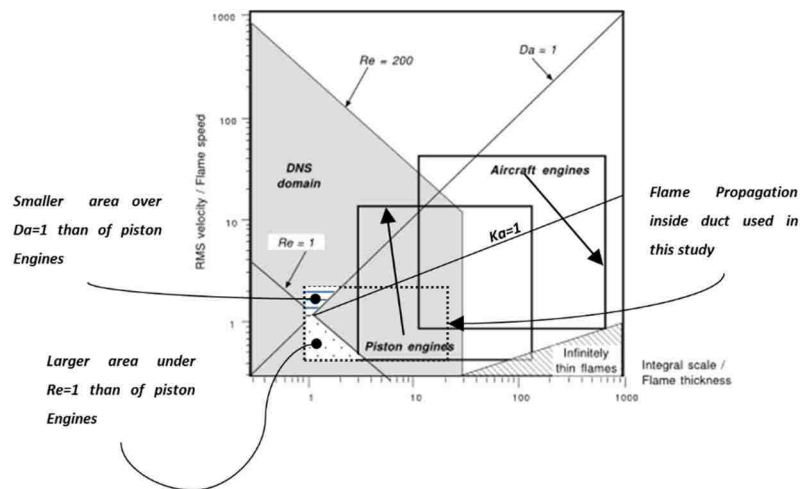
Fig. 8: Using the regime diagram to interpret operating ranges of devices; modified image published in [9]

2.4. RELEVANT HYDRODYNAMIC INSTABILITIES

Hydrodynamic instabilities analyze the stability and the onset of instability of fluid flow. Hydrodynamic instabilities were recognized and introduced in the 19th century by Helmholtz, Kelvin, Rayleigh and Reynolds [18]. The Darius–Landau, Rayleigh-Tailor and Richtmyer-Meshkov instabilities were suspected to affect the flame propagation through a duct which is discussed in 3.2 below.

2.4.1. Darius–Landau instability
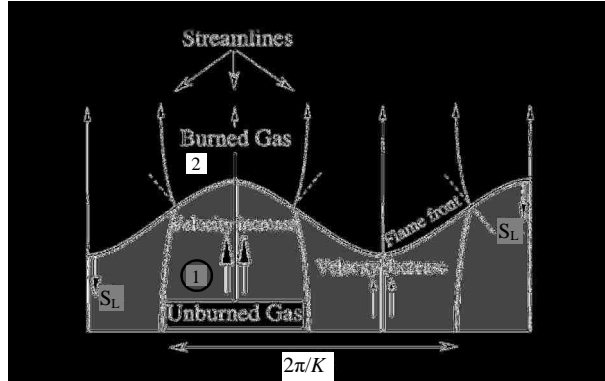
Fig. 9: Deviation of flow lines leading to Darius-Landau instability; image published in [19]

The gas expansion by the heat release in a wrinkled (wave number K) premixed flame traveling at a normal speed of S_L, will deviate streamlines while crossing the flame front. This deviation of streamlines will increase the wrinkling of the flame as shown in Fig. 9 [19]. The theory was predicted independently by Georges Jean Marie Darius (1938) and Lev Landau (1944)[20]. The DL instability is shown in (27) by ω, where S_L is the flame speed, K is the transverse wave number, and σ is the ratio of unburnt gas density to burnt gas density.

$$\omega = S_L K \omega_{DL} \tag{27}$$

Where, $\omega_{DL} \equiv \frac{-\sigma + \sqrt{\sigma^3 + \sigma^2 - \sigma}}{\sigma + 1}$ and $\sigma = \frac{\rho_u}{\rho_b}$

2.4.2. Rayleigh–Taylor instability
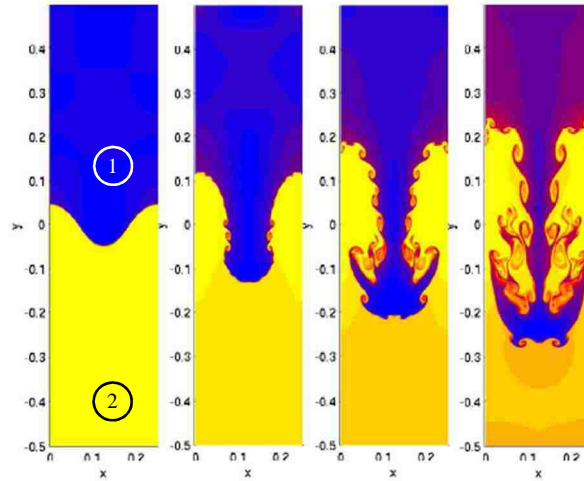
Fig. 10: Simulated results of the Rayleigh–Taylor instability; image published in [24]

This instability occurs at the interface between two fluids of different densities when the lower density fluid accelerates towards the higher density fluid [21]. This can occur under gravity when the lighter fluid is beneath the heavy fluid before the instability starts (Rayleigh [22]), or the lighter fluid having a greater acceleration than the heavy fluid interface (Taylor [23]). Fig. 10 [24], shows four images of the Rayleigh–Taylor instability development in chronological order from left to right. Number 1 in the figure indicates the initial high-density fluid while 2 indicates the low-density fluid, which is analogous to the unburned gas and burned gases respectively in this study. Kull [25] in his paper in 1991 has provided a detailed discussion of the RT instability and the Kelvin-Helmholtz instability which occurs due to the difference in velocities of the two fluids parallel to the boundary in Fig. 10. The conditions to trigger the instability, as well as the growth
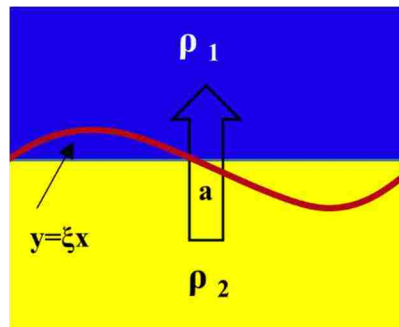
Fig. 11: Instability of a plane contact discontinuity from RT Instability image created based on [25]

16

rate of the instability were identified. A surface perturbation of y=ξ(x) is present at the boundary of fluids with densities ρ_1 and ρ_2 with an acceleration of a, from ρ_2 to ρ_1.

The surface is said to be unstable if;

$$\alpha a K > 0 \tag{28}$$

Where a is the acceleration, K, the wavenumber of the perturbation and $\alpha = \frac{\rho_1 - \rho_2}{\rho_1 + \rho_2}$. α is known as the Atwood number.

The growth rate of the instability is given as (29) [26]

$$Z(t) = \alpha a t^2 \tag{29}$$

Z(t) indicates the penetration distance of denser fluid bubbles into the lower density fluid region.

2.4.3. Richtmyer-Meshkov Instability
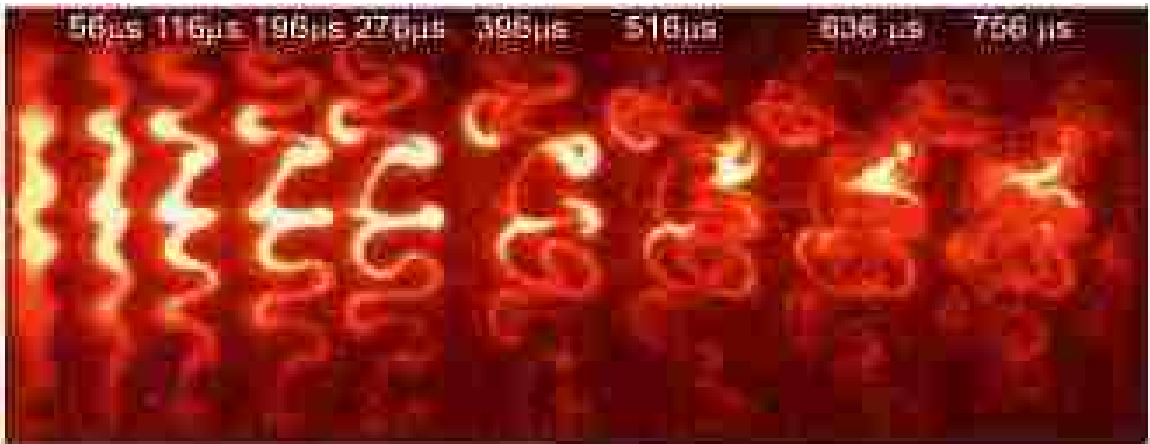
Fig. 12: Coexistence of all morphologies- Richtmyer-Meshkov Instability: image published in [29]

R. D. Richtmyer provided a theoretical prediction of the RM instability in 1960 [27] and E. E. Meshkov in 1969 [28] provided experimental verification of the theory by Richtmyer. Meshkov in his paper states that when a shock wave traverses through the boundary of two fluids with different densities, an instability occurs at the boundary of the two fluids. This instability occurs when the shock wave travels from the higher density fluid to the lower density or in the opposite direction. Fig. 12 from [29] shows a visualization of the Richtmyer-Meshkov instability. The image shows the flow morphology when a planar shock wave is accelerated through the boundary of two gasses

of different densities. It shows nine images taken in sequence. The leftmost image is the initial image. The high-density gas flows as a thin sheet in a vertical plane of the shock tube containing the lower density gas. A horizontal laser sheet illuminates the interface, and the image is taken from the horizontal plane of the Laser sheet.[29].

2.5. THE GLOBAL REACTION OF PROPANE WITH AIR AND STOICHIOMETRY

2.5.1. The global reaction of propane (C₃H₈) and air

A propane air premix is used in experiments. The main reaction taking place and a knowledge of stoichiometry is required. Though we have many reactions going on when combustion happens with propane and air, a Global reaction represents the total or global changes, which the reactants undergo.

$$C_3H_8 + 5(O_2 + 3.76N_2) \rightarrow 3CO_2 + 4H_2O + 18.8N_2 \tag{30}$$
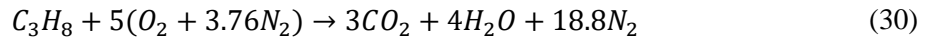
In this reaction in equation (30)we assume that the composition of air:nitrogen is 21:79 volume basis.

2.5.2. Stoichiometry and air to fuel ratio

The stoichiometry of a chemical reaction is when the reactants are mixed in the exact amount needed for the reaction to happen. In the reaction between propane and air as shown in equation (30), the stoichiometric ratio of air:fuel, is 1mole fuel to 5*(1+3.76) moles of air. The ratio of moles is equal to the ratio of volumes of the gasses assuming the gasses are ideal. We can represent the volumetric air to fuel ratio as in (31)

$$[AFR]_{St}^{Vol} = \frac{n_a}{n_f} \tag{31}$$

$[AFR]_{st}^{Vol}$ =volumetric air to fuel ratio at stoichiometry (when the exact number of fuel and air are involved in the reaction).

n_a=number of air molecules

n_f=number of fuel molecules

The volumetric air to fuel ratio at stoichiometry for propane and air is ($[AFR]_s^{Vol}$) 23.8.

2.5.3. The equivalence ratio (Φ) of a combustible mixture

The equivalence ratio is the ratio of air - fuel of a mixture at stoichiometry divided by the air-fuel ratio of the mixture. If the portion of air in the mixture is greater than it should be at stoichiometry, the equivalence ratio will be less than 1. We call mixtures with Φ<1 lean mixture, Φ=1 Stoichiometric mixture, and Φ>1 rich mixtures

$$\Phi = \frac{[AFR]_{St}^{Vol}}{[AFR]^{Vol}} = \frac{[FAR]^{Vol}}{[FAR]_{St}^{Vol}} \tag{32}$$

Φ=equivalence ratio.

$[AFR]^{Vol}$ =Volume ratio of Air to Fuel of an oxidation reaction

$[AFR]_{st}{}^{Vol}$= Volumetric Air to Fuel Ratio at Stoichiometry

$[FAR]^{Vol}$ =Volume ratio of Fuel to Air of an oxidation reaction

$[FAR]_{st}{}^{Vol}$ =Volumetric Fuel to Air Ratio at Stoichiometry (when the exact number of fuel and air are involved in the reaction).

2.6. DOLTON'S LAW OF PARTIAL PRESSURE AND PREPARATION OF GAS MIXTURES

2.6.1. Dalton's Law of Partial Pressure

The partial pressure method is used to prepare the required air-fuel mixture equivalence ratio. This method is based on Dalton's law of partial pressures and the understanding of equivalence ratios. The partial pressure is the fraction of pressure generated due to a particular gas in a mixture of gasses for example in an air-fuel mixture; the partial pressure is represented as in equation (33). According to Dalton's law of partial pressures [30], the total pressure of a mixture of gases is equal to the sum of the partial pressures of the mixture of gases as in equation (33) for an air-fuel mixture, by using the relationship of the number of moles and the partial pressure

.

$$p_T = p_f + p_a \tag{33}$$

p_a =partial pressure of air

p_f =partial pressure of fuel

p_T =total pressure.

2.6.2. Preparation of an air –fuel mixture of a required equivalence ratio

The ratio of the partial pressure of fuel to the total pressure can be written as the ratio of moles using the ideal gas law. By using Dalton's law together with equations (31) and (30), equations (34) and (35) can be written.

$$\frac{p_f}{p_T} = \frac{n_f}{n_f + n_a} = \frac{1}{\left\{\left(\frac{n_a}{n_f}\right) + 1\right\}} = \frac{1}{\left[\frac{[AFR]_{St}^{Vol}}{\Phi}\right] + 1} \tag{34}$$

$$p_f = p_T * \left\{\frac{1}{\left[\frac{[AFR]_{St}^{Vol}}{\Phi}\right] + 1}\right\} = p_T * \left\{\frac{1}{\left[\frac{1}{\Phi * [FAR]_{St}^{Vol}}\right] + 1}\right\} \tag{35}$$

$$p_a = p_T * \left\{\left[\frac{[AFR]_{St}^{Vol}}{\Phi}\right] + 1\right\} = \frac{p_T}{\left\{\left[\Phi * [FAR]_{St}^{Vol}\right] + 1\right\}} \tag{36}$$

Equations (34) and (35) can be used to prepare a mixture with a certain equivalence ratio by measuring the partial pressure of the fuel and air. This method is used to prepare the desired mixture which will be discussed in Chapter 4.

CHAPTER 3

3. BACKGROUND OF FLAME PROPAGATION STUDIES

3.1. EARLY INVESTIGATIONS OF FLAME PROPAGATION INSIDE DUCTS USING PIONEERING IMAGING TECHNIQUES.

Pioneering studies of flame propagation in ducts have been carried out by Mallard and Le Chaterlier in 1883 they observed flame movements using photographic films in their experiments [31].

Mason and Wheeler, interpreted the temperature rise and the propagation of the flame through a uniform cross-sectional duct when the mixture is ignited from the open end of the duct and travels towards the close end. The paper describes the sudden temperature rise of the burnt gasses. The paper also shows a plot of the distance vs. speed of propagation for methane and air at different equivalence ratios. It is shown that a maximum speed is reached when 10 percent of air is present at the mixture (bell shaped curves). Higher diameters of tubes had higher flame velocities.

Mason and wheeler used copper wires placed at an equal distance along the propagation to determine the speed of propagation by recording the time each wire melted as soon as the flame heated them up. They were experimenting with tubes which were closed at one end, and the flame was ignited at the open end. The length of tubes used was 5 m. They have observed a uniform flame movement along the duct in this configuration [32].

Mason and Wheeler in their paper on horizontal propagation [33] mentioned the oscillating movements in flames through tubes after a period of the uniform movement and termed this the "vibratory movement." They used the revolving film method to study the propagation of the flame; they attributed the "vibratory movement" to the resonance of the column of gas ahead of the flame front and the closed end of the tube. When the flame was initiated from the closed end of the tube, they have clearly observed a rapid increase in the flame propagation speed, followed by "the vibratory motion and also a backward movement. While testing with a 30m tube of 90cm diameter, the flame extinguished in all the mixtures, after a distance of 15m. They mention, "Violent Vibrations" occurring when the flame traveled close to 10m from the point of ignition. They have concluded the reason for the flame traveling back being due to the cooling of the hot combustion products behind the flame front, creating a partial vacuum. When experiments were carried out with both ends open, the backward movement of the flame was not reported. They used photographic film to measure the flame travel distance and time. The paper shows the images from the film of a flame moving from left to right. The film was traveling vertically at a speed of 30cm/s.

A steep line in the image shows a slow moving flame; and a line close to horizontal, shows fast moving flame. The fast flame corresponded to a flame ignited at the close end traveling to the open end. The flame travelling with both ends open was slower than the above. When the flame was started from the open end, the flame speed was the slowest. The fastest moving flame had, rapid oscillations of the flame, this oscillation of the flame movement could not be recorded. It was done through the screen wire method explained earlier. The highest speed of flame movement recorded in this set of studies was 60 m/s[33].

O. C. De C. Ellis and Henry Robinson started high-speed photography to record images of flames in 1925 [34]. They used a revolving shutter method unlike the films used by Mallard and Lechaterlier, and Mason and Wheeler. Mallard and Lechaterlier could not record the shape of a flame front, but Mason and Wheeler could record the shape of the flame only when the propagation speed of the flames were "not" irregular. The method of high-speed imaging by Ellis and Robinson made it possible to record images in irregular flame movements as well.

In 1928 Ellis carried out a series of investigations using the new high-speed imaging technique and acquired quite a number of images and related data of flames traveling in tubes with various configurations.

In the initial publication of the series in 1928 [35] Ellis noted when a flame is ignited at the center of a spherical vessel it extinguishes before the end of the vessel wall. He investigated the pressure rise at the vessel wall. He concluded that the pressure rise in the unburnt gas region could have caused this early extinction of flame.

In the study on the propagation of flame from central ignition within a tube by Ellis [36], a combustible mixture of CO and O_2 was ignited at the center of a circular tube. In narrow tubes, the acceleration reduced rapidly to a negligible value in a short period and a shorter distance from the ignition than in larger diameter tubes. He also noted that the flames were much faster when the two ends were open than closed. The heat loss through the wall was mentioned as reasons for narrow tubes being quicker to extinguish. Some interesting images of multiple ignitions in ducts were published in the same paper in the same paper. His studies of flames, when ignited at the closed end of a duct [37], is the most relevant to the present work. Fig. 13, [37], shows a series of images on a flame propagating through a closed duct. He has distinguished two phases of flame travel when the diameter of the tube is "exceedingly less" compared to its length. The initial phase is the fast moving phase, which is depicted by initial four snapshots of the flame front from the right side of Fig. 13, the second phase is the slow moving phase shown by the remaining snapshots, which can be seen placed very close to each other compared to phase one. He has observed that the start of the second phase moves closer to the point of ignition when the tube length is shorter. He has

attributed this phenomenon to the higher cooling rate when the pressure is higher in shorter tubes. In this study, Ellis noted sudden accelerations and decelerations leading to reverse movement of the flame when ignited from the closed end of a tube when the other end is open or closed. Bonn and Frazer in 1932 have also mentioned the two phases of propagation mentioned earlier and has attributed the effects of compression waves traveling through the duct as the reason for the 2nd phase or the vibratory motion. They have also mentioned that in "strong mixtures" just above stoichiometry could be converted to a detonation wave.[38].
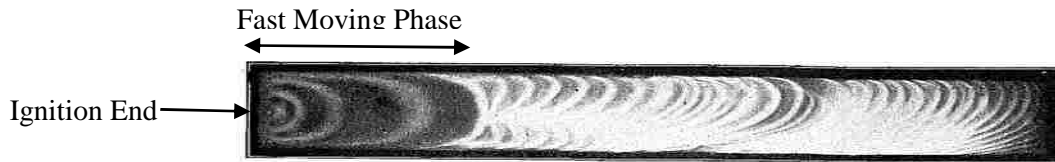
Fig. 13: High speed images of a propagating wave in a closed duct by Ellis in 1928: image published in [37]

3.2. INVESTIGATION OF HYDRODYNAMIC INSTABILITIES IN FLAME PROPAGATION THROUGH DUCTS AND THE USE OF FLASH SCHIEREN PHOTOGRAPHY

Markstein in 1957 carried out studies of flames traveling inside tubes [39]. During the flame propagation inside a duct, pressure waves are generated (random waves or oscillations). In his paper, Markstein investigated the flame front interaction with a pressure wave generated from the opposite end of ignition of the tube. He used the Schlieren spark photographs, to capture the flame shapes. Fig. 14 shows the flame shapes at the moment of a pressure wave colliding with a flame front. The flame shapes are quite similar to the images of tulip flame formation [39]. He concluded that higher the pressure ratio of the pressure wave generated higher was the radiation of the flame.

Fig. 14: Initial stages of the shock wave flame and front interaction with three images showing the stages of the development of the tulip flame: image published in [39]

23

He has tentatively identified the mechanism of the formation of the tulip flame as a modified version of the Taylor instability.

Salamander et al. in 1958 gave the name "Tulip-Flame" to the flame shape occurring in the first acceleration-deceleration sequence shown in   Fig. 15 [6]. Flash Schlieren photographs were employed to supplement the direct photographs which only used the luminosity of the flame. The flash Schlieren photographs enabled the capturing of pressure differences. Impulse lighting was used in in the new method to enhance images taken with small exposure times. The images were captured at 100,000 to 150,000 frames per second with exposure times in the range of 10^{-7} s. They have identified an initial propagation stage with a meniscus-shaped flame accelerating to a certain distance, then during a slowing down stage the flame taking the "tulip" shape. A gas flow opposite to the direction of propagation has been identified at this stage, followed by a greater acceleration of the flame. They have attributed shock waves traveling in front of the flame to the acceleration phases of the flame front [6].

Dunn-Rankin and Swayer in 1997 carried out experiments on tubes with both ends closed using pressure measurements and Schlieren images. They used three igniter geometries. They concluded that the ignition geometry did not affect the tulip flame formation and the tube geometry had an effect on the formation of the tulip flame [40].
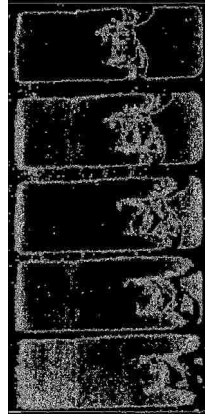
Fig. 15: The tulip shaped flame captured by Salamandra et al.: Image published in [6]

3.3. RECENT NUMERICAL AND EXPERIMENTAL INVESTIGATIONS OF PREMIXED FLAME PROPAGATION IN DUCTS

Dunn – Rankin et al. in 1988 used laser doper measurements and a numerical simulation, assuming the fluid is completely inviscid for a flame propagating in a closed rectangular tube. In their paper,

they explain the formation of a tulip flame being the result of the inviscid interaction of compressed gases ahead of the flame front and the vessel walls [41].

Gonzales et al. pointed out that heat transfer from the boundaries of the vessel, acoustic effects, viscous effect are not prominent in the formation of the tulip flame. He mentioned that finding a single mechanism to explain the tulip formation could be misleading. However, he points out that the Darius–Landau instability and the transversal velocity gradient along the flattened front subsequent to the "squish flow" or flow due to compression, and the deceleration of the central part of the flame could be significant in the formation of the tulip flame[42].

Clanet and Searby (1996) have looked at the problem using a half opened circular tube. By comparing the results of Markstein [39] with the Richtmyer Meshkov and Rayleigh-Taylor instabilities explained earlier in 2.4.3 and 2.4.2 respectively, they predict that the formation of the tulip flame is a manifestation of the Taylor instability driven by the deceleration of the flame tip. They have pointed out the resemblance of the tulip shape, with the shape of the flame when the shockwave interacted with the flame in the said experiment.

In the same paper [43] they approached the problem by looking at four distinct stages of propagation before the formation of the tulip flame. Namely an initial time of $t_0 < t < t_{sphere}$, $t_{sphere} < t < t_{Wall}$, $t_{Wall} < t < t_{Tulip}$, $t_{Tulip} < t$. The sphere refers to the time of the flame developing as a hemisphere; wall refers to the time at which the flame touches the wall of the tube; tulip refers to the time of starting the tulip flame. A simplified geometric model is presented as in Fig. 16 [43]. They have plotted the variation of pressure with time at the ignition end and used reduced pressure and reduced time to graphically represent the results where they were able to identify a distinct pattern of pressure variation regardless of the burning velocity (or initial Φ). The laminar burning velocity S_L was used to deduce the normalized time and pressure and the tube radius to normalize the flame position in Fig. 17 [43]. They concluded that neither viscosity nor acoustic effects are
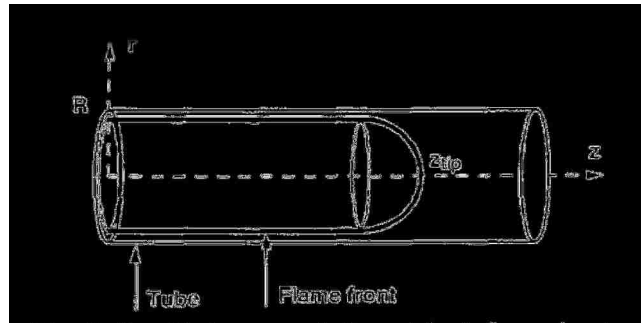
Fig. 16: Simplified geometric model of flame front at times between t $_{Sphere}$ and t $_{Wall}$: image published in [43]

25

prominent in the flame propagation in the said intervals. As long as the flame thickness is small compared to the tube dimensions; S_L, the tube radius R and the gas expansion coefficient E= ρ_u/ρ_b (where E is the ratio of the unburnt to burnt gas densities) are the only parameters governing the tulip phenomenon. The growth rate of the flame tip was related to the parameters above by equations (37) and (38) where Z_{tip} is the distance of the flame tip from the point of ignition.

$$\frac{dZ_{tip}}{dt} = \frac{Z_{tip}}{\tau} \tag{37}$$

Where;

$$\frac{1}{\tau} = \frac{2EU_L}{R} \tag{38}$$
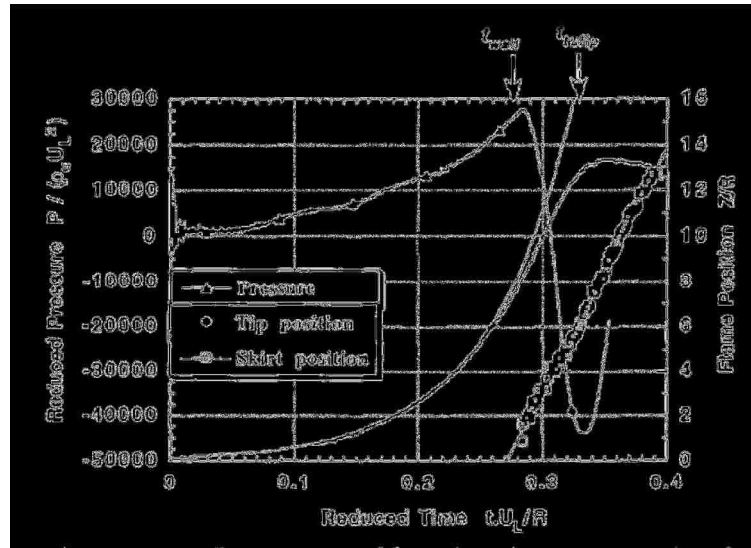
Fig. 17: Normalized superposition plot of pressure at closed end, the position of center of flame tip and of tailing edge of flame skirt; as a function of time. The best fit exponential is also shown: image published in [43]

McAlary [44] has concluded that the variations of propagation velocities from the mean were large for $\Phi<1.1$, Battoei et al.[45] has plotted the average flame velocity (AFV) along the duct for the fully open end with $\Phi=1.1$ which shows results which match with propagation characteristics in this work.

Valiev et al. [46] have concluded that the models in Clanet and Searby [43] and Bychkov [47] with the assumption of an incompressible fluid thus overestimates the growth rates of initial finger

26

flames with higher laminar flames speeds such as hydrogen and acetylene. They also comment that the shape of the channel affects the growth rate of the finger-shaped flame.

Sobiesiak et al. [48] have shown that the number of inversions can be modified by the mixture strength and the conditions of the duct exit end. The number of inversions was higher for the mixtures below and above $\Phi=1.1$ and the exit end gradual closing suppressed formation of
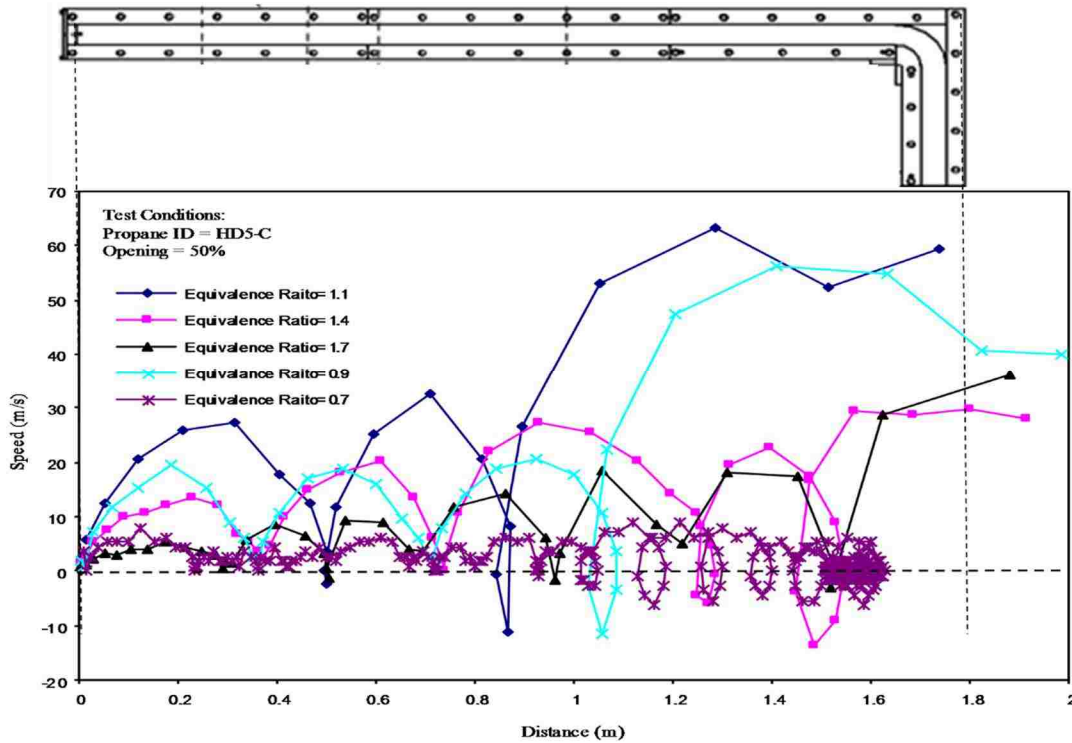
Fig. 18: Location of the tulip flame and first inversion in an L shaped rectangular duct; modified image published in [48]

inversions. The location of the tulip flame and inversions were compatible with the ones in this work Fig. 18.

Zhou et al. [49] have investigated the flame propagation in a rectangular duct with a 90° bend. They have concluded that the tulip flame formation is due to flame front and flame induced flow. The authors have observed the flattening of the flame surface, which introduces uneven force distribution on the flame front. The higher forces closer to the walls of the duct are suspected to increase flame velocities in the edges of the ducts inducing the tulip shape.

Xiao et al. in 2012 [50] have used Schlieren photography, pressure records, and LES to comment on the distorted tulip flame formation after the formation of a classical "tulip flame." They have

27

concluded that the vortices generated in the burnt gas behind the tulip flame create conditions for different flame propagation rates, as this, in turn, leads to the formation of the distorted tulip flame. Xiao et al. in 2013 [51] have observed the formation of a classical tulip flame after the formation of the distorted tulip flame. They mention that the distortions disappear as the primary cusp and the distortions merge into each other. They conclude that reverse flow dominates the burnt region near the flame front during the formation of the distorted tulip flame.

Xiao et al. in 2015 [52] mention the initiation of the tulip flame and the distorted tulip flames occurred just after a sudden deceleration of the flame front. They attribute the distorted tulip to the Rayleigh-Taylor instability driven by pressure waves.

Though a large number of studies are available on flames propagating in ducts, studies on flames propagating in ducts through a stratified medium are limited. The available studies with stratified medium have not been carried out for flames propagating in ducts where tulip flames and inversions are observed.

3.4. STUDIES OF FLAME PROPAGATION THROUGH STRATIFIED MIXTURES

Pires Da Cruz et al. [53] have numerically studied a methane-air flame traveling through a stratified mixture. They found that the laminar flame speed was strongly affected by the equivalence ratio gradient. The production of molecular hydrogen from the original fuel, its transport to the reaction zone, and the heat transfer from burnt to fresh gas are key factors in understanding the influence of stratification on laminar flame speed. They have concluded that lean stratified flames traveling from stoichiometric to lean are faster than their homogeneous flames.

Cessou et. al [54] have carried out an experimental study of propane-air flames propagating through a stratified medium. They have used PIV (Particle Image Velocimetry) for velocity measurements and LIF (Laser Induced Florescence) to visualize the distribution of equivalence ratios. They studied the very early stages of combustion up to 6ms from start of flame. Injection of fuel or air to the control volume was the method used to stratify the mixture. To rule out the turbulence effects of the injection they have compared results of the same mixture injected in place of fuel and air. They have concluded that the local burning velocity can increase or decrease the local burning velocity according to the distribution of the local equivalence ratio.

Haworth et al. [55] have done numerical simulations for propane-air premixed flame propagation in a non-homogeneous medium. They have pointed a secondary reaction zone exists three to four flame thicknesses behind the primary reaction zone. The reaction rate of this zone is dominated by turbulent mixing and the CO_2 production mechanism.

.

28

CHAPTER 4

4. EXPERIMENTATION

4.1. EXPERIMENTAL SETUP

The experimental procedures and apparatus used here is a derivative of those used by M. Mcklary in 1999[44], Stephan Mckellar 2004 [56] and Mohsen Battoei in 2007[45].

McKellar and Battoei put the majority of the apparatus together during their studies. The setup was modified to suit the present experiments. The modifications will be highlighted when describing the units in the following chapters.

4.1.1. Flame Propagation Duct (FPD)
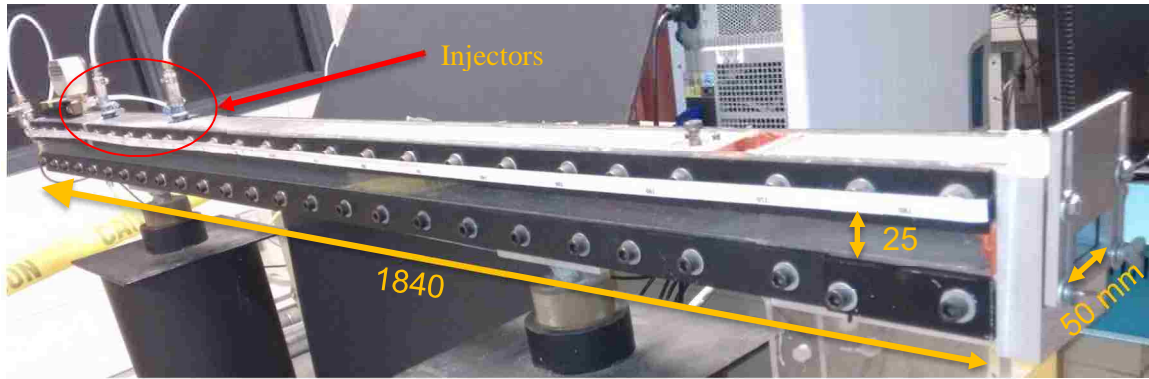
Fig. 19: Image of the flame propagation duct
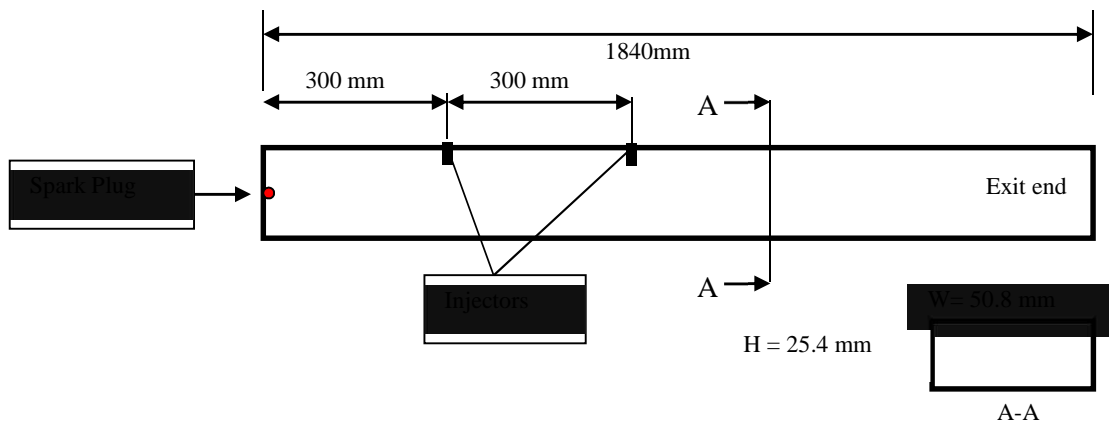
Fig. 20: Schematic diagram of the flame propagation duct

The FPD has dimensions of 50.8mmx25.4mmx1840mm. The duct is equipped with two transparent sides walls opposite to each other for optical access. These sides are fabricated of 12.7 mm thick clear Lexan panels. Injectors are located at 300mm and 600mm from a permanently closed end of the duct. The ports for the injectors are fabricated on the 50.8 mm side of the duct which enables the injector jets to be parallel to vertical side walls.

A gas delivery manifold is used to deliver the mixture and flush the combustion products from inside the duct after each experiment. It also has an Omega 4-digit absolute pressure gauge to indicate the pressure inside the duct. The absolute pressure gauge allows the duct to be filled to required pressure regardless of the atmospheric pressure under closed end conditions and to indicate the pressure when the duct is vacuumed before filling it with the initial air-fuel mixture.

The closed end of the duct has two threaded ports, one for a centrally mounted spark plug and one to deliver reactants. The same delivery port is used to mount a pressure transducer. Two steel cylindrical stands support the duct with a square base for stability. The stands are equipped with a mechanism that included bearings for simple height adjustments to level the duct.

Modifications to the FPD

The duct was leak tested by pressurizing to 20Psi and using soap foam to locate the leakages visually. New O-rings and silicon sealant are used to stop the leakages at the exit end of the duct. The repair was mandatory since the duct had to be fully vacuumed before filling with a fresh charge.

4.1.2. Ignition System

The ignition system comprises a high voltage transformer, a switch and modified automotive type spark plug. The transformer is a model found in gas or oil-fired home heating furnaces. This

particular unit operates on 120 V AC, and output approximately 10,000 V DC with a current rating of 20 mA. It has a standard 120 V grounded power plug. The electrical discharge is transferred to the spark plug by way of high-voltage insulated wire. The spark plug is modified by removing the ceramic core and inserting in the holes to make the electrodes. The wire, ceramic core and metal casing are sealed together using a non-conductive silicon sealant.

The spark is controlled by TTL (Transistor-Transistor Logic) type optical switch that is triggered by an output signal from data acquisition board through a BNC (Bayonet Neill–Concelman) connector and coaxial cable and managed by National Instruments' LabVIEW software. The trigger box has a 120 V grounded input plug as well as an out plug for the transformer. The optical switch, the triggering circuit and the data acquisition board are insulated from the high voltage of the

transformer. Therefore, no electromagnetic noise from the spark plug interfered with the data collection.

4.1.3. Injection system and injection timing control

The injection system consists of two commercial propane gas injectors, control box, and DC power supply. The injectors are mounted at the top center of FPD at 30 cm and 60cm from the spark end. The injectors are controlled by the injector control box which is triggered by an output signal from the DAQ device and managed by LabVIEW software.

4.1.4. Modifications to the injection system

- An in-line flow meter (Alicat Type 16 Mass and volume flow meter) was coupled to the injector (will be described with the data acquisition systems).
- A pressure regulator was introduced to provide the required injector pressure.
- A 4-way valve was introduced for the injector to change the substance injected without dismantling the system. This modification will be explained under the mixing panel below.

4.1.5. Gas-Mixing Panel and handling of the gas between the gas- mixing panel and flame propagation duct

The gas-mixing panel in Fig. 21 is used to prepare the combustible mixture of propane and air at the required equivalence ratio. The partial pressures of air and propane are used to prepare the mixture, which will be described in detail in later chapters. The mixture panel is fitted with a thick-walled 2250 ml sample cylinder in Fig. 22 to mix and store air/fuel mixture. The gauge on the mixture preparation panel is an Ashcroft type 1082 combination vacuum and pressure test gauge. The vacuum side of the gauge is delineated in inches of mercury (in Hg) while the pressure side of the gauge is delineated in pounds per square inch gauge (psig), given an accuracy of 0.25% of the full scale. The maximum operational pressure is 700 kPa (100 psig). Consequently, gas regulators are required to reduce the output pressure from the individual gas cylinders.

A vacuum pump is included with mixture preparation panel to initially evacuate the sample cylinder and internal piping before preparing a gas mixture. The vacuum pump has a rated ultimate pressure of 0.2 kPa and a corresponding error of 0.2%.

Fig. 21: Gas mixing panel front

**Fig. 22: The mixing chamber of
the gas mixing panel**

The fuel and oxidizer gases are supplied from two, high pressure, industrial gas cylinders. The fuel used for this study is Instrument Grade 99.5% propane and the oxidizer is dry air.

Modifications to the gas-mixing panel

- New piping and valves were installed to allow a single operator to vacuum and then fill the duct. Fig. 23 shows the piping and instrument Diagram.
- A 4-way valve was installed to the panel so that, fuel, air or gas mixture could be directed towards a regulator before the injector (V10 in Fig. 23).
- One of the four valves in the above 4-way valve was coupled to the vacuum pump for the injector to be vacuumed. The modification allowed vacuuming the substance in the piping before switching to a different substance in the injector line.
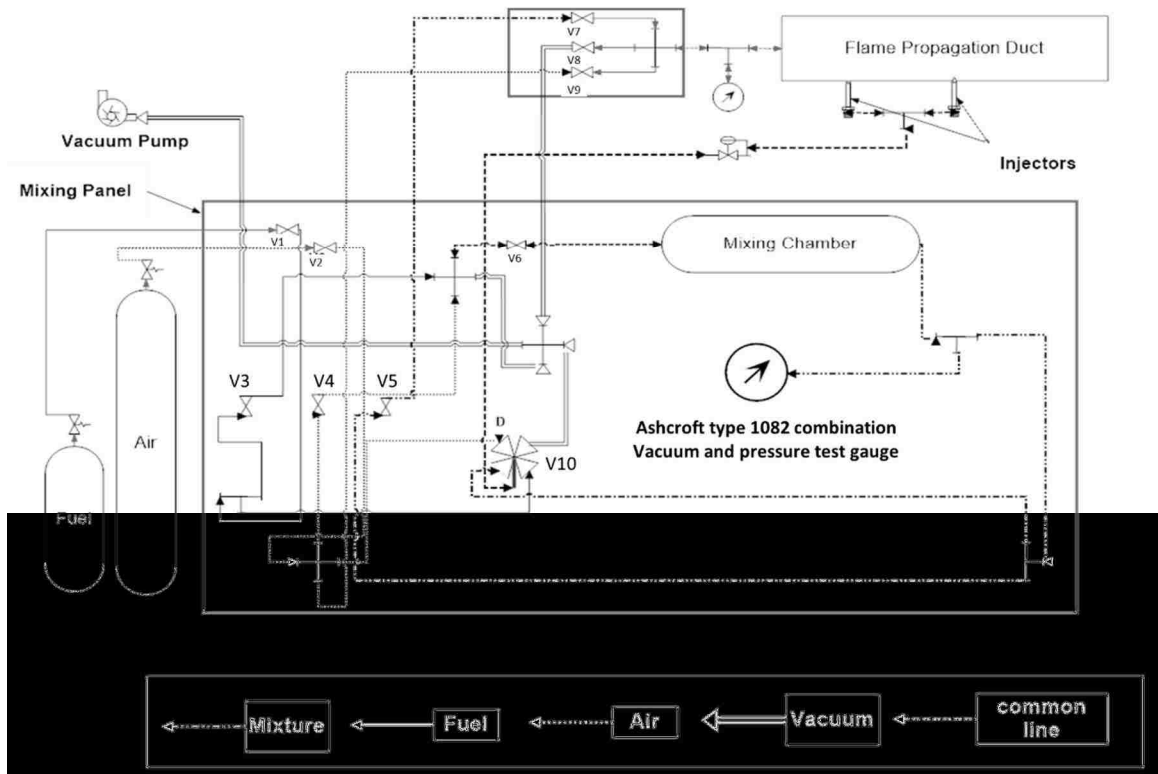
Fig. 23: Piping and instrumentation diagram for the modified mixture panel, connections to the flame propagation duct and Injectors

4.1.6. The LabVIEW Program

The LabVIEW program enabled to trigger the injectors, CCD camera and the spark to be triggered at required timing as well as to change the duration of the pulse. The duration of the pulse is used to keep the injectors open for a required time which alters the mass of gas injected. The duration of the ignition allows the spark to be present for a required duration to initiate the flame. The correct duration of the pulse to operate the camera is recommended by the instruction manual of the camera.

Modifications to the LabVIEW program

The LabVIEW program which was present did not allow for data acquisition. The code was modified to acquire data. The modifications are described in detail in 4.3.

33

4.2. UNCERTAINTY ANALYSIS

4.2.1. Uncertainty of the mass of substance injected

Calibration Uncertainty of the Alicat Flow meter

Fig. 24 shows the calibration data provided for the Alicat flow meter [57]. Based on the good data correlation fitting a straight line through the origin, the calibration for the DAQ board was taken as the ratio between the difference of the highest and lowest readings of calibration(39).
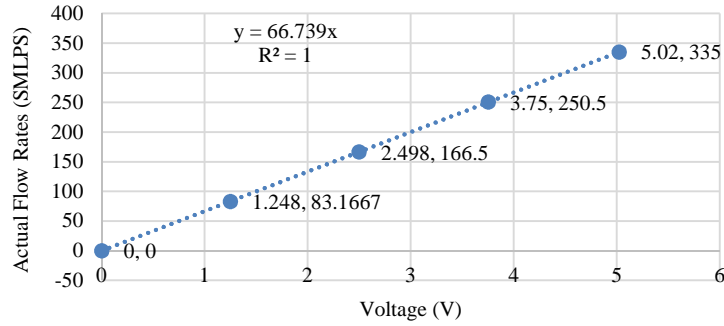
Fig. 24: Calibration chart from Alicat flow meter

Table 4: Data used for calibrating the DAQ Assistant in LabVIEW

Mass Used for Calibration	Description	Value	Unit
$\dot{Q}_1$	Smallest flow of calibration	0	SMLPS
$\dot{Q}_2$	Largest flow of calibration	335	SMLPS
V_1	Voltage for $\dot{Q}1$	0	V
V_2	Voltage for $\dot{Q}2$	5.02	V
$(\dot{Q}/V)_{cal}$	Calibration coefficient for the NI DAQ Assistant	66.733	SMLPS/V

$$\left(\dot{Q}/V\right)_{Cal} = \frac{(\dot{Q}_2 - \dot{Q}_1)}{(V_2 - V_1)}$$

(39)

Based on the relationship in (41); for the uncertainty of $(\dot{Q}/V)_{cal}$, equation (39) was used to arrive at equation (40) This equation gives the uncertainty of $(\dot{Q}/V)_{cal}$

(40)

$$u_{(\dot{Q}/V)_{Cal}} = \sqrt{\left[\left(\frac{1}{V_1-V_2}\right)*U_{Q_1}\right]^2 + \left[\left(\frac{-1}{V_1-V_2}\right)*U_{Q_2}\right]^2 + \left[\left(\frac{Q_2-Q_1}{(V_1-V_2)^2}\right)*u_{V_1}\right]^2 + \left[\left(\frac{Q_1-Q_2}{(V_1-V_2)^2}\right)*u_{V_1}\right]}$$

Table 5: Uncertainty of individual parameters to calculate uncertainty of the calibration coefficient for the Alicat flow meter (to be used in the NI DAQ Assistant in LabVIEW)

	Uncertainty Type	Description of Uncertainty	Value	Units
e_1	Calibration Uncertainty V1	±(0.8% of Reading+0.2% of full scale)	0	V
e_2	Calibration Uncertainty V 2	±(0.8% of Reading+0.2% of full scale)	±0.05	V
e_3	Calibration Uncertainty $\dot{Q}1$	±(0.8% of Reading+0.2% of full scale)	±0.67	SMLPS
e_4	Calibration Uncertainty $\dot{Q}2$	±(0.8% of Reading+0.2% of full scale)	±3.35	SMLPS
e_5	Zero Order Voltage	50% of resolution	±0.005	V
e_6	Zero Order Flow	50% of resolution	±0.005	SMLPS
u_{V1}	Overall Uncertainty V1	Calculated using equation (85)	±0.005	V
u_{V2}	Overall Uncertainty V2	Calculated using equation (85)	±0.05	V
u_{Q1}	Overall Uncertainty Q1	Calculated using equation (85)	±0.67	SMLPS
u_{Q2}	Overall Uncertainty Q2	Calculated using equation (85)	±3.35	SMLPS
$U_{(\dot{Q}/V)cal}$	Final Calibration Uncertainty	Calculated using equation (40)	±0.895	SLPM/V

The Final Calibration - $(\dot{Q}/V)_{cal}$ =66.733

Uncertainty of calibration $U_{(\dot{Q}/V)cal}$ ±0.895 SLPM/V

Extension of calibration uncertainty to final injected mass uncertainty

$$m = V * \left(\dot{Q}/V\right)_{Cal} * t * \rho$$

(41)

Table 6: Uncertainty of individual parameters to calculate the uncertainty of mass of substance injected

Symbol	Definition	Value	Unit
m_{inj}	mass injected	m	mg
Um	Uncertainty of mass injected	Eq.(42)	mg
$(\dot{Q}/V)_{cal}$	The Final Calibration	66.733	SMLPS/V
$U_{(Q/V)cal}$	Uncertainty of calibration	±0.895	SMLPS/V
t	Time	t	S
U_t	Assume zero	0	S
P	The density of substance.		Kg/m³
U_ρ	The uncertainty of density.	0	Kg/m³
V_{5v}	Voltage reading of LabVIEW DAQ card	5	V
U_{D5v}	Design Stage uncertainty of NI6035 -5V	±2.338	V

$$\frac{U_m}{m} = \pm \sqrt{\left(\frac{U_V}{V}\right)^2 + \left(\frac{U_{CD}}{\left(\dot{Q}/V\right)_{Cal}}\right)^2 + \left(\frac{U_t}{t}\right)^2 + \left(\frac{U_\rho}{\rho}\right)^2}$$

(42)

$U_m = \pm 1.34\%\ m_{inj}$

The uncertainty of mass injected is ±1.34% of the total mass injected

4.2.2. Uncertainty of the pressure measurement

Uncertainty of calibration and Amplification of signal

The transmission function F of the Dual mode amplifier has been calculated using (43) formula given in the Kistler Dual mode 5004 Amplifier manual[58].

Table 7: The uncertainty values of individual parameters to be used to determine the error in the amplification of the pressure signal

CIS	Calibration input sensitivity of Amplifier	1	mv/Pc
U$_{CIS}$	Uncertainty of CIS	±0.5	%
ST	Sensitivity of Transducer	16	Pc/Bar
U$_{ST}$	Uncertainty of transducer sensitivity at full scale	±0.5	%
S	Selected Scale	0.1	mv/bar
U$_{S}$	Uncertainty of S	±0.5	%

$$F = \frac{CIS\left[\frac{mv}{Pc}\right] * ST\left[\frac{Pc}{Bar}\right]}{S[\frac{mv}{bar}]} = -160 mv/V \tag{43}$$

$$\frac{U_F}{F} = \pm\sqrt{\left(\frac{U_{CIS}}{CIS}\right)^2 + \left(\frac{U_{ST}}{ST}\right)^2 + \left(\frac{U_S}{S}\right)^2} = 0.9\% \tag{44}$$

To calculate the error of the conversion factor (P/V)$_{Cal}$ in [bar/V] to be used in the LabVIEW DAQ Assistant The equation(45) has been used, with the values in Table 7. Equation (42) was used as the governing equation to obtain the required calibration for the LabVIEW DAQ Assistant. Equation (83) has been applied to obtain the uncertainty of (P/V)$_{Cal}$ in equation (46)

$$\left(\frac{P}{V}\right)_{Cal} = \frac{F[\frac{mv}{V}]}{ST\left[\frac{Pc}{Bar}\right] * CIS\left[\frac{mv}{Pc}\right]} = 10\ bar/V \tag{45}$$

$$\frac{U_{\left(\frac{P}{V}\right)_{Cal}}}{\left(\frac{P}{V}\right)_{Cal}} = \pm\sqrt{j\left((-1)*\frac{U_{CIS}}{CIS}\right)^2 + \left((-1)*\frac{U_{ST}}{ST}\right)^2 + \left(\frac{U_F}{F}\right)^2} = 1.1\% \tag{46}$$

Propagation of the calibration and amplificaton uncertainty to the final uncertainty of pressure

The uncertainty of the pressure reading U_{PR} from the LabVIEW DAQ Assistant can now be obtained using the calibration value and the uncertainty of the calibration value from equations (47) and (48)(66).

The design error of voltage below is found from Table 34

$U_{D10V} = \pm 8.65$
$V = 10V$

$$P = V * (P/V)_{Cal}$$

(47)

$$\frac{U_{PR}}{PR} = \pm \sqrt{\left(\frac{U_V}{V}\right)^2 + \left(\frac{U_{\left(\frac{P}{V}\right)_{Cal}}}{\left(\frac{P}{V}\right)_{Cal}}\right)^2} = 1.4\%$$

(48)

$U_{PR} = P*1.4\%$

At the operating range of 10 bars in our experiment $U_{PR} = \pm 1.4$ bar

4.2.3. Uncertainty of the equivalence ratio

Using the definition of Stoichiometry and using Daltons law of partial pressure (paragraph 2.5 and 2.6)

$$\Phi = \frac{P_f}{P_a} * [AFR]_{St}^{Vol}$$

(49)

Using equations (83) and (49) and the value of air to fuel ratio of 23.8 for propane-air mixture the uncertainty of $\Phi = 1.1$, $U_{\Phi=1.1}$ is given by

$$u_{\Phi=1.1} = \pm 23.8 \sqrt{\left(\frac{u_{p_f}}{p_a}\right)^2 + \left(\frac{-p_f * u_{p_a}}{p_a^2}\right)^2}$$

(50)

38

U_{pf} = error of reading the partial pressure of fuel = $U_{Ashcroft}$ = ±0.25 Psi

U_{pa} = error of reading the partial pressure of air = $U_{Ashcroft}$ = ±0.25 Psi

Pa and pf are taken from Table 22 which will be explained later in chapter 4.5.1 (Preparation of the air/propane premix at desired equivalence ratio).

Table 8: The uncertainty of the equivalence ratio prepared

Φ	UΦ
1.10	±0.056
1.00	±0.057
0.90	±0.057
0.80	±0.058

4.2.4. Uncertainty of distance measurements

The distance and velocity measurements are done using image processing. Initial calibration of the image is required to calculate the distance. The actual distance shown between two known pixels in the image are used to calibrate the image.

Table 9: Uncertainty values for individual parameters to calculate the uncertainty in image processing for distance and velocity for the camera settings to capture the total duct length

LT_{mm}	Actual Length for calibration of image	1840	mm
LT_{pix}	A number of pixels between two points of known displacement.	1258	Pixels
SC	Scale used in image processing	1.462639	mm/Pixel
U_{LTmm}	Uncertainty of actual length measurement	±0.5	mm
U_{LTpix}	Uncertainty of the pixel count	±0.5	Pixels
U_{SC}	Calculated Uncertainty of the scale used in image processing	±0.000704	mm/Pixel
L_{pix}	The sample number of pixels to calculate the length and error.	100	Pixels
L_{calc}	Calculated sample length using the scale	146.26	mm
U_{Lcalc}	Uncertainty of the calculated distance from image processing [given from (62)]	±0.511	mm

$$SC = \frac{LT_{mm}}{LT_{Pix}}$$

(51)

39

Equation (52) is obtained using equation (83) for the relationship in (59) .

$$U_{SC} = \pm SC * \sqrt{\left(\frac{U_{LT_{mm}}}{LT_{mm}}\right)^2 + \left(\frac{U_{LT_{pix}}}{LT_{pix}}\right)^2}$$

(52)

For calculating a length from the image (53) was used.

$$L_{calc} = Sc * L_{Pix}$$

(53)

Equation (54) is obtained by using equation (83) for (53).

$$U_{L_{calc}} = \pm L_{calc} * \sqrt{\left(\frac{U_{SC}}{SC}\right)^2 + \left(\frac{U_{LT_{pix}}}{L_{Pix}}\right)^2}$$

(54)

The uncertainty of the calculation of a length from images is given by equation (54)

4.2.5. Uncertainty of velocity calculations

Table 10: Uncertainty values for individual parameters to calculate the uncertainty of velocities calculated from images

t	Time interval	0.1	ms
D_I	Initial Distance at start of time interval t		mm
D_F	Final Distance at the end of time interval t		mm
$V_{(D1-D2)}$	Mean Velocity at time t		m/s
$U_{V(D1-D2)}$	Uncertainty of calculated velocity		m/s
U_{DI}	Uncertainty of Distance measurement for D_I	±0.5	mm
U_{DF}	Uncertainty of Distance measurement for D_F	±0.5	mm

$$V_{(D_I-D_F)} = \frac{D_I - D_F}{t}$$

(55)

Using (83) for the relationship in (55) we get (56)

$$U_{V_{(D_I-D_F)}} = \pm \sqrt{\left(\frac{\partial V_T}{\partial D_I} * U_{D_I}\right)^2 + \left(\frac{\partial V_T}{\partial D_F} * U_{D_F}\right)^2}$$

(56)

$$U_{V_{(D_I-D_F)}} = \pm \sqrt{\left(\frac{U_{D_I}}{t}\right)^2 + \left(\frac{U_{D_F}}{t}\right)^2} \tag{57}$$

The measurement uncertainty $U_{DI} = U_{DF} = U_{L(calc)}$

$$U_{V_{(D_I-D_F)}} = \pm \sqrt{2 * \left(\frac{U_{L_{Calc}}}{t}\right)^2} \tag{58}$$

Table 11: Uncertainties for distance and velocity calculated from images for different image calibrations and different velocity calculation methods

	Calibration						Velocity Calculation					
	U_{LTmm} [mm]	LT_{mm} [mm]	U_{LTpix} [Pixel]	LT_{Pix} [Pixel]	SC [mm/Pixel]	U_{SC} [m/Pixel]	$U_{L(CALC)}$ [mm]	$V_{(DI-DF)}$ [mm/ms]	Lcalc[mm]	Lpix [mm]	t [ms]	$U_{V(DI-DF)}$ [m/s]
1	0.5	1840	0.5	1250	1.472	0.00071	±1.15	26.91	1832	1245	68.1	±0.024
2	0.5	1840	0.5	1250	1.472	0.00071	±0.736	14.72	1.472	1	0.1	±10.409
3	0.5	1840	0.5	1250	1.472	0.00071	±0.736	29.44	2.944	2	0.1	±10.409
4	0.5	1840	0.5	1250	1.472	0.00071	±0.736	44.16	4.416	3	0.1	±10.409
5	0.5	1840	0.5	1250	1.472	0.00071	±0.736	58.88	5.888	4	0.1	±10.409
6	0.5	1840	0.5	1250	1.472	0.00071	±0.736	73.6	7.36	5	0.1	±10.409
7	0.5	1840	0.5	1250	1.472	0.00071	±0.736	88.32	8.832	6	0.1	±10.409
8	0.5	1840	0.5	1250	1.472	0.00071	±0.736	103.04	10.304	7	0.1	±10.409
9	0.5	1840	0.5	1250	1.472	0.00071	±0.736	117.76	11.776	8	0.1	±10.409
10	0.5	1840	0.5	1250	1.472	0.00071	±0.736	132.48	13.248	9	0.1	±10.409
11	0.5	1840	0.5	1250	1.472	0.00071	±0.736	147.2	14.72	10	0.1	±10.409
12	0.5	1840	0.5	1250	1.472	0.00071	±0.736	161.92	16.192	11	0.1	±10.409
13	0.5	1840	0.5	1250	1.472	0.00071	±0.736	176.64	17.664	12	0.1	±10.409
14	0.5	1840	0.5	1250	1.472	0.00071	±0.736	191.36	19.136	13	0.1	±10.409
16	0.5	1840	0.5	1250	1.472	0.00071	±0.736	206.08	20.608	14	0.1	±10.409
17	0.5	10	0.5	93	0.108	0.00543	±0.121	21.6	2.16	20	0.1	±1.711
18	0.5	10	0.5	93	0.108	0.00543	±0.224	43.2	4.32	40	0.1	±3.168
19	0.5	10	0.5	93	0.108	0.00543	±0.33	64.8	6.48	60	0.1	±4.667
20	0.5	10	0.5	93	0.108	0.00543	±0.438	86.4	8.64	80	0.1	±6.194
21	0.5	10	0.5	93	0.108	0.00543	±0.546	108	10.8	100	0.1	±7.722
22	0.5	10	0.5	93	0.108	0.00543	±0.654	129.6	12.96	120	0.1	±9.249
23	0.5	10	0.5	93	0.108	0.00543	±0.762	151.2	15.12	140	0.1	±10.776
24	0.5	10	0.5	93	0.108	0.00543	±0.87	172.8	17.28	160	0.1	±12.304
25	0.5	10	0.5	93	0.108	0.00543	±0.979	194.4	19.44	180	0.1	±13.845

Row number 1in Table 11 shows the uncertainty of velocity when the average AFV is calculated by dividing total distance (duct length) from the time taken for the total flame travel. Rows 2 to 16 shows the absolute instantaneous velocities calculated for 1 to 14 pixels traveled per 0.1 milliseconds. 17 to 24 shows the instantaneous velocities calculated at a higher accuracy by using a higher resolution image (higher number of pixels per mm or lower scale of mm/pixels).

4.2.6. Summary of uncertainties and special points to note

Table 12: Summary of uncertainties

Property	Uncertainty
(Mass injected)m_{inj}	$U_m=\pm1.34\%\ m_{inj}$
(pressure) PR	$=\pm1.4$ bar
$\Phi=0.8$	$U_{\Phi0.8}=\pm0.056$
$\Phi=0.9$	$U_{\Phi0.9}=\pm0.057$
$\Phi=1.0$	$U_{\Phi1.0}=\pm0.057$
$\Phi=1.1$	$U_{\Phi1.1}=\pm0.058$
(Length measurements from image processing)L_{Calc}	$U_{\ LCalc}$ in Table 11
(Velocity measurements from image processing)$V_{(D1-D2)}$	$U_{V(DI-DF)}$ **[mm] in** Table 11

- When comparing tests with different equivalence ratios, confusing results can be expected due to the uncertainty of the prepared Φ.
- If more accurate velocity measurements are needed, close-up images (which gives a higher resolution for the area concerned) should be captured which can be explained from inspecting Table 11.

4.3. DATA ACQUISITION AND CONTROL SYSTEM

The data acquisition system acquires image data from

I.   The CCD (Charge coupled device) camera

II.   Pressure variation at the ignition end of the FPD using a pressure transducer

III.   Flow through the injectors using a flow meter upstream of the injectors

A LabVIEW program manages the triggering of ignition, injection and Data Capturing. Fig. 25 shows the total data management system. The LabVIEW codes for data acquisition was completely written, and the existing code for triggering was updated for this study. Data acquisition is described in detail in the following chapters.

4.3.1. Data acquisition frequency

The image capturing frequency decides the data acquisition frequency or the sampling frequency. The images of the flame captured at 10,000 frames per second seemed to provide sufficient details

of the image for the fastest traveling flame. This flame traversed the duct in approximately 100 ms for an open end case with equivalence ratio 1.1. This is the case used in all injection trials described later in the chapter. Around 1000 frames per test run is captured in these trials.
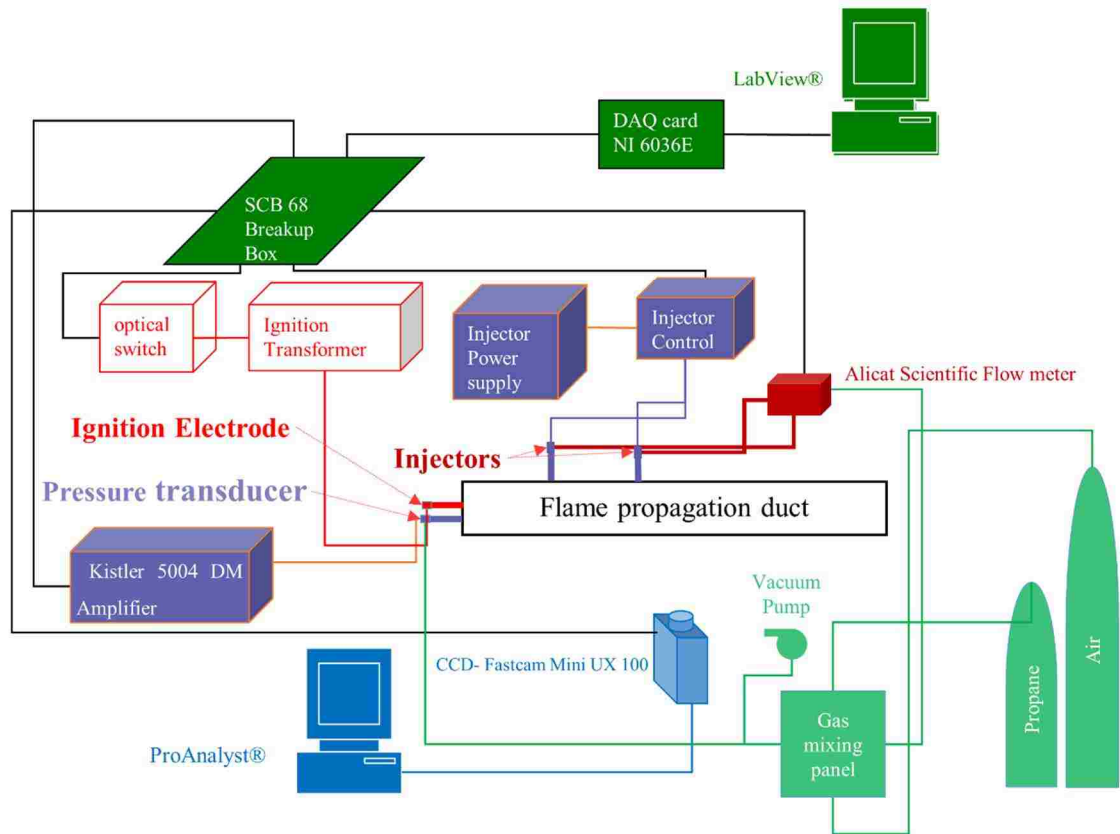
Fig. 25: Experimental setup with the data acquisition and control system.

The following data was acquired

1. Images showing the flame front position captured at 10,000 Frames per Second (Fps)
2. Pressure reading at the ignition end at a sampling frequency of 10,000 Hz
3. Instantaneous flow reading for the injected substance at a sampling frequency of 10,000 Hz

For each image captured, the following 6 data points are processed

I.   Time in steps of 0.1 ms
II.   The position of the flame front at each time interval
III. The instantaneous velocity calculated using data from I and II above
IV.   The pressure reading at the ignition end

V.   The mass flow rate

VI.   The total mass injected up to the time

4.3.2. Control program for data DAQ System

The front panel of the control program is shown in Fig. 26. The inputs to the program are; delay and pulse quantities for the Spark (4), CCD (5), injectors (1), (2), and (3).
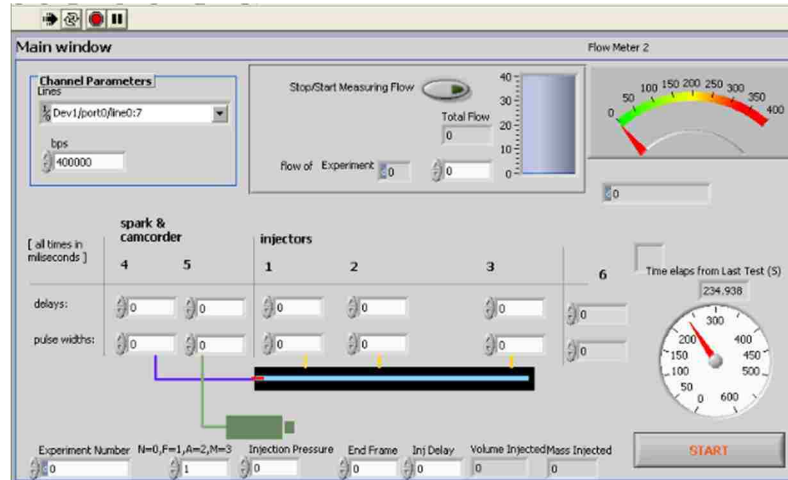
Fig. 26: The LabVIEW program to control ignition and DAQ system

Modifications to the existing program

The program was modified to record and save the mass injected, injection pressure, the last frame number of the total number of frames of the captured image sequence and the ambient temperature. All the data shown in the panel are saved to an excel file.

The instantaneous flow of the injected gas is recorded in each time interval. This flow reading is corrected to the mass of gas injected into the duct at the injection pressure and temperature and displayed after each run.

The start button triggers the data acquisition by the pressure transducer and flow meter immediately. The camera, ignition and injectors are triggered at the input delay and pulse width, with the same start button. All the acquired data are written to a file. The various filtering and calculations done after the collection of data are explained in chapter 4.4.

4.3.3. Image Data Acquisition

The image data is captured using a CCD. The FASTCAM Mini UX 100 type 800k-M-8G is used to capture images. The description of the CCD and settings used for capturing images are given in Table 13.

Table 13: General description and settings of the CCD image capturing

Camera Type	FASTCAM Mini UX100 type 800K-M-8G
Record Rate(fps)	10000
Shutter Speed(s)	1/10000
Trigger Mode	Start
Image Width	1280
Image Height	200
Color Type	Mono
File Format	Avi

4.3.4. Pressure Data Acquisition

The pressure sensor used is a 6117BF Piezoelectric Sensor. Table 14 [59] provides the characteristics of the sensor. The sensor signal is then amplified and filtered using an 180 kHz low pass filter using a Kistler Type 5004 Dual mode Amplifier

Table 14: Characteristics of the Pressure sensor used

Measuring range bar	0 - 200
Sensitivity pC/bar	−15
Natural frequency kHz	≈130
Linearity %FSO	≤±0,5
Temp. Range (sensor) °C	−20 - 200
Sensitivity change 200 °C ±50 °C %	≤±0,5
Thermal shock error at 9 bar P$_{mi}$ (1500 1/min)	
Δ P (short term) bar	≤±0,6
Δ P$_{mi}$ %	≤±3
Δ P$_{max}$ %	≤±1,5

.

The amplifier sensitivity is set to 15pC. The negative sign of the transducer sensitivity is ignored here since Kistler transducers deliver a negative charge for positive loads and the transducer produces a negative signal from a positive input [58]. The transducer produces 0 to 10v for a range of 1-100 bar pressure range. The output of the amplifier is connected to an SCB -68 breakup box. The DAQ card 6036E (National Instruments) is used to acquire voltage signal from the Breakup box.

The "DAQ Assistant" feature of LabVIEW for the pressure reading is calibrated using the calibration settings of 0-100 bar indicating 0-10 V as in Fig. 27.The Calibration is done according to (45) in paragraph4.2.2. The final calibration used is 10V/bar. The scale shows the gauge pressure. 6000 readings at 10,000 Hz is recorded. Pressure measurements up to 6s are written to an Excel sheet. The sampling frequency of pressure is taken as 10000Hz to be equal to the sampling frequency of the image data acquisition of the CCD of 10000 FPS.
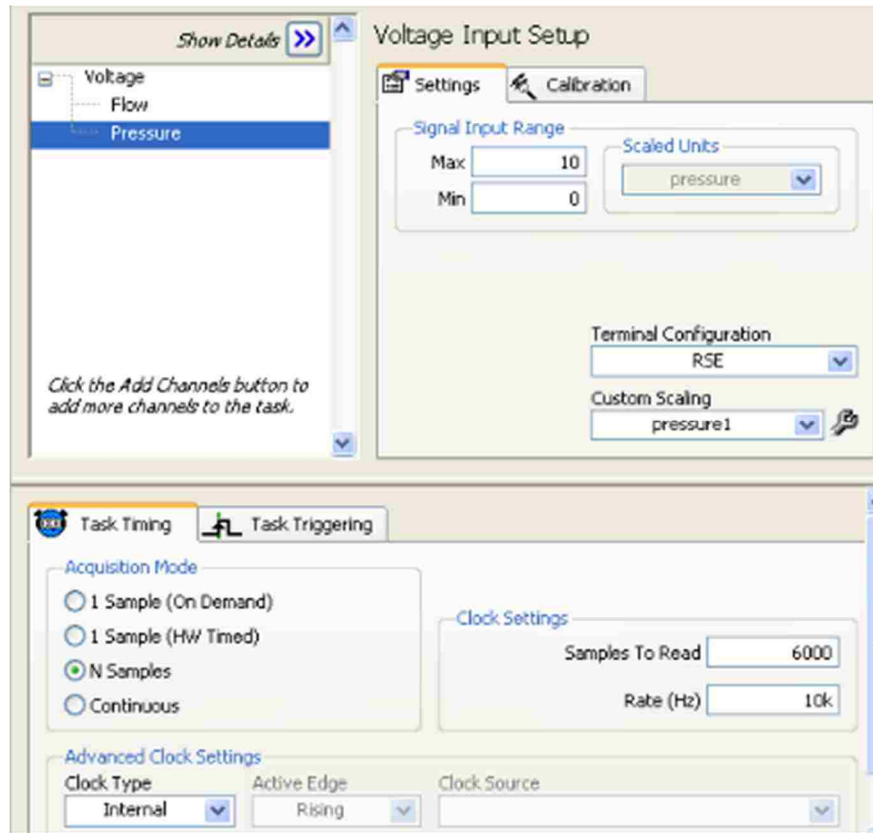
Fig. 27: LabVIEW DAQ Assistant - calibration for pressure recording

4.3.5. Flow Data Acquisition

The flow data is acquired using the "Alicat scientific 16 Series" mass and volumetric gas flow meter. The meter provides a voltage signal directly to the SCB 68 breakup box and the DAQ card. The same National Instruments 6036E is used to acquire the data. The LabVIEW program is used to capture and record the data using the DAQ Assistant configurations for the flow meter. A low pass filter is used to filter the high-frequency noise. Unlike in the pressure data acquisition, the data recorded was processed using the integral function of LabVIEW in addition to the direct reading. The block diagram for flow data acquisition is shown in Fig. 28. The integral function will provide

47

the integral of the input function. The Data captured are instantaneous flow rates in milliliters per second; the integral function converts it to milliliters at each time interval.
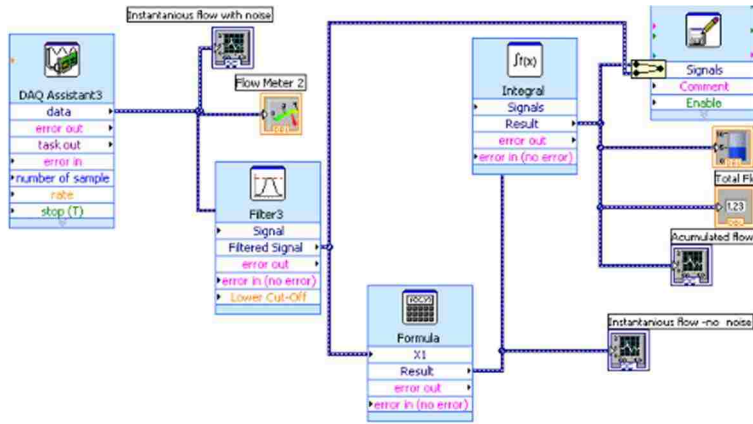
Fig. 28: Block diagram indicating the integral function and filtering used to process the flow data

6000 samples are recorded at a sampling frequency of 10,000 Hz. Fig. 29 show the calibration of the flow meter in the LabVIEW DAQ Assistant. The Standard Temperature and Pressure used for calibration are 25ºC, 14.7 PSIG. The Corresponding Calibration values were 5.02 V I ~ 20.08 SLPM and 0V ~0SLPM. The calibration is given in the calibration certificate of the flow meter[57], The values were converted to SMLPS (standard milliliters per second).
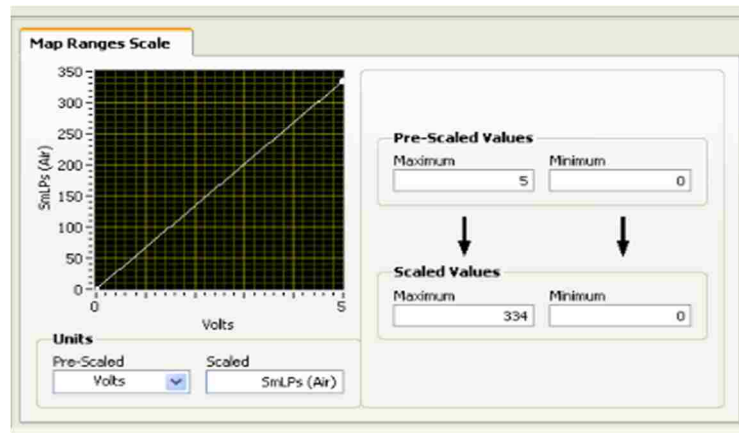
Fig. 29: Calibration of the DAQ Assistant for flow meter

The value in Standard Liters per Minute is converted to Standard Milliliters per second to configure the DAQ assistant as in Fig. 29. The measurement of mass flow rates of air, propane and mixture was then corrected to the injection pressure and temperature.

48

4.4. PROCESSING OF COLLECTED DATA

4.4.1. Processing of Image Data

The images are captured and saved in AVI file format. This image file is then processed using ProAnalyst® an image processing software.

The maximum resolution of the image is limited by the FPS set for the recording session. Images are recorded every 0.1 ms at 10000 FPS. Image capturing is triggered using the LabVIEW software. The start of ignition is recognized as the 1st white pixel recorded in the sequence. The x-axis is selected to align with the center of the duct, which is the axis horizontal to the duct passing through the center of the ignition electrode. The origin of the x-axis is set to the tip of the ignition electrode. Then the line tracking option in ProAnalyst® is selected to track the movement of the bright flame front.
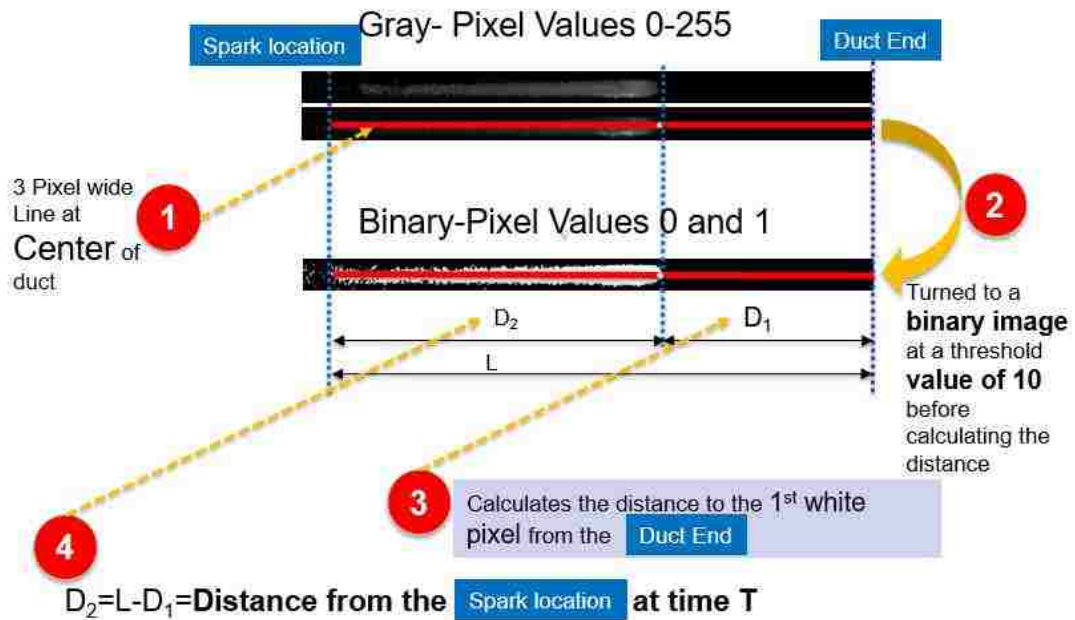
Fig. 30: Using image processing to derive the flame position

The method used to find the flame position in each image is illustrated in Fig. 30. Two points along the axis are selected as the tracking line (number 1 in the Fig. 30). This line will represent the centerline of the duct. The line thickness and threshold limit of the whiteness are selected. The gray scale image which is initially available is a matrix of pixels, where each pixel has a number corresponding to the gray scale. A value of 0 corresponds to a 100% white cell, and a value of 256 corresponds to a 100% black cell. Numbers in-between displays a mix of black and white thus brighter regions have a higher value than a dark region.

49

The threshold value converts all pixels having a gray scale value less than the specified value to 0 (**B**lack) and the others to 1(**W**hite). This enables to produce a matrix of 1 (**W**hite) and 0 (**B**lack) (number 2 in the Fig. 30). Then the number of pixels from the end of the duct to the 1st white cell is determined (number 3 in the Fig. 30). This enables to find the distance from the ignition end (number 4 in the Fig. 30). The scale of mm/pixels converts the number of pixels to mm.

Initially, the calibration of the image should be done. This procedure enables to read distances from the image file. The actual distance measured between two pixels in the image are used to calibrate the image. A calibration file is produced by using this information. The data is stored as mm/Pixel, and the origin and orientation of the x and y-axis are also saved in this calibration file.

For a 100 ms image recording, 1000 images are saved, the position of the flame front in each image is written to a file, a sample of such a recording is given in Table 15. The B to W column in the table indicates a detection of a white cell along the measuring line. Frames 230-232 and 234 indicates that no white cell is displayed along the line of tracking. Tracking point x column indicates the flame position at the particular frame corresponding to the frame number in the Frame column.

This sample set of image data indicates that the flame propagation is initiated at frame 235, which means 23.5 milliseconds after the start of recording images. Though in 233 a white cell is detected, the flame has not started propagating because in 234 a black cell is indicated, therefore the start of the flame is considered as 235. The "Level" column in Table 15 indicates the level of gray scale indicated, the threshold for this example is 10, this means all pixel levels less than 10 are considered black (indicated by -1). The gray scale level is indicated only for the values greater or equal to 10 in the table. Column Y indicates the position of the center of tracking line in the Y direction relative to the coordinate system adapted in the calibration file.

Table 15: Line tracking data

| Frame | Time | Track Point | | Dist. to P1 | B to W | Level |
		X(mm)	Y(mm)			
230	0.023	-1	-1	-1	-1	-1
231	0.0231	-1	-1	-1	-1	-1
232	0.0232	-1	-1	-1	-1	-1
233	0.0233	4.389313	0	1833.27	0	10
234	0.0234	-1	-1	-1	-1	-1
235	0.0235	4.389313	0	1833.27	0	10
236	0.0236	2.926209	0	1834.733	0	10
237	0.0237	4.389313	0	1833.27	0	10

The Calculation of the instantaneous absolute flame velocity

The images are processed to represent a set of time and the corresponding position of the flame along the centerline. The position is the distance from the exit end Table 15 . This data is used to calculate the instantaneous absolute flame velocity of the flame at every time interval. The flame front at an instance may have velocities in different directions, but by choosing the center line, we only consider the flame displacement along this line which we have identified as the x- axis in this study. The velocity is displayed rather than a flame speed.

The velocity calculation estimates that the recorded distance is at the start of the time interval, there for the instantaneous velocity is calculated by subtracting the displacement recorded in the next time interval by the displacement recorded in the present time interval. This difference is divided by 0.1 ms. The instantaneous velocity, in this case, is defined as the average flame velocity during a 0.1 ms interval along the x-axis. Table 16 shows a set of data.

Table 16: Time distance and corresponding instantaneous flame velocity table

Frame #	Time (ms)	Distance (mm)	Absolute flame velocity (m/s)
240	24	3.66	21.95
241	24.1	5.85	0
242	24.2	5.85	4.88
243	24.3	6.34	24.39
244	24.4	8.78	9.75
245	24.5	9.75	24.39
246	24.6	12.19	-19.51
247	24.7	10.24	45.72
248	24.8	14.81	3.05
249	24.9	15.12	-8.53
250	25	14.27	15.36
251	25.1	15.80	17.56
252	25.2	17.56	-14.63

4.4.2. Processing of pressure data

The data received to the Breakup box filtered by a Butterworth low-pass filter at 25Hz and 50Hz. A Bandpass filter of 60 Hz-100 Hz is used to capture any acoustic oscillations which could be suspected as the 1st harmonic of the longitudinal pressure oscillation.

Formula (60) is used to calculate acoustic oscillation frequency in a rectangular tube of length*width*length of x*y*z.[7]

$$f = \frac{C_0}{2}\left[\left(\frac{n_x}{l_x}\right)^2 + \left(\frac{n_y}{l_y}\right)^2 + \left(\frac{n_z}{l_z}\right)^2\right]^{\frac{1}{2}} \tag{59}$$

n_x= oscillating modes in the x direction

n_y= oscillating modes in the y direction

n_z= oscillating modes in the z direction

f= resonant frequency of the modes n_x, n_y and n_z

C_0= speed of sound (or pressure wave)

l_x= width of the tube

l_y=hight of the tube

l_z=length of the tube

$$C_0 = \sqrt{\gamma * \left(\frac{R}{M_{Air}}\right) * T} \tag{60}$$

R specific =Universal Gas Constant/Molar mass of the substance

γ=Cp/Cv

Cp=Heat capacity at constant Pressure

Cv=Heat capacity at constant volume

T= Temperature in Kelvin

M_{Air}=Molar Mass of Air

Using the values in the table, we deduce the values for the sound of speed as in Table 17; it is assumed that the pressure wave travels through the air throughout.

Table 17: Values to find the speed of sound

T	298	K
γ_{air}	1.4	
R	8.317x10³	J k⁻¹ Kmol⁻¹
M_{Air}	29	kg kmol⁻¹
C₀	**346**	**m/s**

Direction	x	y	z		
Length	2.1	0.05	0.025	Identification	f(Hz)
Modes	1	0	0	First longitudinal	82
	2	0	0	Second longitudinal	165
	6	0	0	Third longitudinal	494
	1	0	1	First transvers in x - first longitudinal	6921
	1	1	0	First transverse longitudinal	3461

The 1st harmonic of the longitudinal frequency was investigated using a band pass filter (60Hz-100Hz).

4.4.3. Processing of Flow Data

The flow data is calibrated for Air at STP. This data should be converted to injected (Air, propane or mixture) pressure and temperature of the gas at the flow meter. The data recorded is the instantaneous flow at each 0.1 milliseconds from the start of data acquisition.

The conversion assumes that all gasses are Newtonian fluids. To convert the readings recorded for air at STP to Propane or Mixture or air at a given temperature and pressure; the Alicat Scientific Operating Manual use the Poiseuille Equation (61) and the Ideal Gas Laws[60]. The mass flow rates for various gasses can be displayed in the apparatus. But since we need the data to be exported to the CPU as an Excel file, the data exported should be converted later.

$$Q = \frac{(P_1 - P_2)\pi r^4}{8\eta L} \tag{61}$$

Q = Volumetric Flow Rate

P1 = Static Pressure at the Inlet

P2 = Static Pressure at the outlet

R = Radius of the restriction

η = Dynamic or Absolute Viscosity of the Fluid

The reading we receive is for air; if we need to convert the readings to propane or a mixture of propane/ air we have to convert them as in (62) and (63).

$$Q_{Propane} = Q_{Air} * \frac{\eta_{Air}}{\eta_{Propane}} \tag{62}$$

$$Q_{Mixture} = Q_{Air} * \frac{\eta_{Air}}{\eta_{Mixture}} \tag{63}$$

η_{Air} = Dynamic or Absolute Viscosity of air

$\eta_{Propaner}$ = Dynamic or Absolute Viscosity of Propane

$\eta_{mixture}$ = Dynamic or Absolute Viscosity of the premix with a known Φ

The values of η_{Air} and $\eta_{Propaner}$ can be known from the literature. But $\eta_{mixture}$ has to be calculated. Davidson[61] has proposed an accurate and simple method to calculate the Dynamic viscosity of mixtures if you know the η of the mixing gases and the ratio of mixing.

$$fl_{12} = \frac{1}{\boldsymbol{\eta_{12}}} = \frac{p_1{}^2}{\eta_1} + 2\frac{p_1 \cdot p_2}{\sqrt{\eta_1} \cdot \sqrt{\eta_2}} * E_{12}{}^A + \frac{p_2{}^2}{\eta_2} \tag{64}$$

fl_{12} = is the fluidity or simply the inverse of dynamic viscosity of the mixture of substance 1 and 2

η_{12}= Dynamic viscosity of the mixture of substance 1 and 2

A= an imperial constant which is approximated to 1/3

p_i is defined as the momentum fraction which is the fraction of the total momentum associated with the particular component.

$$p_i = \frac{x_i * \sqrt{M_i}}{\sum(x_i * \sqrt{M_i})} \tag{65}$$

x_i = Mole fraction of component i

M_i =Molecular weight of component i

$E_{1,2}$ = the mean efficiency with which body 2 transfers energy to body 1

m_1 = mass of body m1

m_1 =mass of body m2

$$E_{1,2} = \frac{\sqrt{m_1} * \sqrt{m_2}}{(m_1 + m_2)} \tag{66}$$

Table 19: Values to calculate viscosity of mixture

	$M,(m_1\&m_2)(g)$	X	$\sqrt{M}$	$\sqrt{M}*x$	η (Pois)or $(g\ cm^{-1}\ s^-)^1$
C3H8	44	1	6.63325	6.63325	81.458
air	29	21.63636	5.385165	116.5154	184.918

Table 20: Results of equations (64),(65) and (66) to find the dynamic viscosity of propane-air mixture @ Φ=1.1

E_{12} (Efficiency Factor)	0.16	
p_{C3H8} (Momentum Fraction of Propane	0.05	
Pair (Momentum Fraction of air)	0.95	
fl_{12} (Fluidity of the mixture at Φ=1.1)	0.01	P^{-1}
η_{mix} (Propane air @ Φ=1.1)	187.56	P

The values for dynamic viscosity for air and propane were extracted from the Alicat Scientific Operating Manual[60].Now using the values of dynamic viscosity of Propane, Air and, Mixture the flow can be corrected to the relevant fluid flowing through the flow meter. Next step is to correct for the pressure; we use the ideal gas equation for this. Since the value indicated is at p_1= 14.7 Psi, to correct the value for P_2 and know the new density of the fluid we use the equation (67) derived from the ideal gas law.

$$\rho_1 = \rho_1 \frac{p_1}{p_2}$$

(67)

$$Q_2 = Q_1 \frac{\eta_2}{\eta_1}$$

(68)

Using the (67) and (68) and knowing the dynamic viscosities (η), injection Temperature (T) and the injection pressure (P) for each fluid, corrections to the flow rate reading can be done. Once the conversions are complete, we get the injected mass flow rate at 0.1ms intervals for the flow through the injector in mg/s and the output from the integral functions which is in mg. Table 21 shows the correction matrix used in the spreadsheets to calculate the corrected values for mass flow rates.

Table 21: The table of correction values for 40.13 PSi injection pressure (P) and 300k temperature (T)

Substance	ρ (kg/m3)	M (g/ mol)	R (kJ/kg/k)	η (Pois)or (g cm^{-1} s^-)^1	Volume correction factor ($\eta_{substance}$/ η_{Air})
C3H8	4.879826	44	189	81.45	2.270102384
Air	3.213544	29	287	184.91	1
Air/C3H8@ Φ=1.1	3.28216	29.6	281	187.55	2.119204843

4.5. EXPERIMENTAL PROCEDURES

4.5.1. Preparation of the air/propane premix at desired equivalence ratio

The gas is prepared to the required equivalence ratio using the partial pressures of gasses. The method and theory of the preparation were given in paragraph 2.6 page 19 and 20.

Ashcroft type 1082 combination vacuum and pressure test gauge are used to monitor the partial
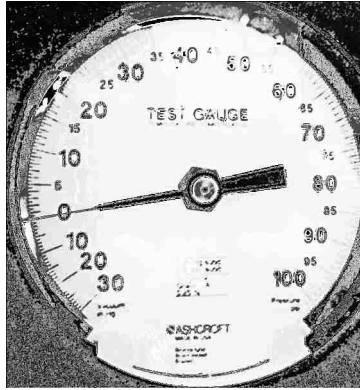
Fig. 31: The Ashcroft pressure gauge dial

pressure readings inside the mixing chamber (Fig. 23). The gauge shows the gauge pressure, and the zero is adjusted to the ambient pressure. The Partial pressures of air and fuel are calculated using. Equations.(60) and (61) in paragrapg2.6.2 page 20

Example of preparation of a $\Phi = 1.1$ propane air mixture is given below

$[AFR]_s^{Vo}$ =23.8.

Desired Φ =1.1

The partial pressure of fuel is chosen so that the total pressure does not exceed 100 Psi which is the maximum pressure of the mixing chamber. The total pressure is calculated using equation (69) which is a modification of equation (34)

$$p_T = \frac{p_f}{\left\{\dfrac{1}{\left[\dfrac{[AFR]_{St}^{Vol}}{\Phi}\right] + 1}\right\}} * \qquad (69)$$

The P_T (total) is an absolute pressure. It needs to be converted to the gauge pressure. The maximum partial pressure of fuel is selected where the total pressure does not exceed but very close to 100Psi. The pressure gauge for the mixing chamber shows vacuum pressure in inches mercury (inHg). The mixing vessel is vacuumed to 27 inHg (The bottle could not be vacuumed to 30inHg (0 Psi absolute)

56

due to practical reasons) It is assumed that the 3inHg partial pressure is P_{air} and fill in air until the needle points to a value equal to P_f. Then fill in air from the Pf value up to 0. Finally, fill the rest of the bottle up to P_T. the calculated values to prepare a propane air mixture at $\Phi=1.1$ is shown in Table 22. Table 23 gives the summarized values to be used to prepare the mixture looking at the gauge in the mixture panel.

Dry air with 79% N_2 and 21% O_2 and instrument grade propane (99.5% Propane) is used to prepare the air-fuel mixture.

Table 22: Calculated values for partial pressure and corresponding readings of the instrument used

Partial Pressure	PSI Absolute Value	Psi Gauge Value	Vacuum inches mercury Reading
Air (Pa)	106.27	91.56	-
Total Pressure (P_T)	111.18	96.47	-
Fuel (P_f)	4.91	0	10
(P_{a3})	101.35	86.65	-
(P_{a2})	3.43	-	7
(P_{a1})	1.47	-	3
Vacuumed UP to	1.47	-	27

Table 23: Procedure to prepare a mixture of propane-air of an equivalence ratio of 1.1

Procedure	Reading	
Vacuum Bottle up to	27	inHg Vacuum
Fill air up to	10	inHg Vacuum
Fill Propane up to	0	Psi Gauge
Fill air again up to	96.5	Psi Gauge

4.5.2. Preparation of the duct and other equipment for an experiment

- All equipment should be connected properly as per Fig. 25.
- The premixed air-fuel mixture is prepared and stored in the mixing chamber.
- The camera should be placed to the desired view and set to trigger mode (This setting makes the camera ready to operate with the pulse from the control program).
- The required substance to inject and the proper injection pressure should be adjusted if injections are carried out.

- The flame propagation duct is closed from the exit end and vacuumed (It can be vacuumed to 0.8 Psi Absolute).

- The mixing chamber valve is opened to fill the duct.

- The duct pressure gauge is monitored, and the mixing chamber valve is closed just above the atmospheric pressure (around 14.8-15 Psi).

- If the trial is an open end, then the exit end of the duct should be opened.

- The control program is triggered with the required values for delay and injector pulse times in place.

- Once the Program is triggered, and the flame propagation takes place. The. Pressure and flow data files should be saved with the relevant experiment number. The control program prompts for the file names.

- The recorded movie file is then saved.

- The experiment number, injection pressure, and the ambient temperature is recorded in the control program before the next experiment. A maximum of 6 trials can be performed with one preparation of the mixing chamber.

4.5.3. Identification codes of the experiments

Since a large number of experiments are done, experiments were labeled according to a predetermined code. The identification code is important when working with injections. Three types have been used to describe, injections before and after ignition and flames without ignitions. An "IF: logic is used in the MS Excel spreadsheets to name the flame when the flow data, pressure data, and image data is exported to the spreadsheet.

Table 24: Description of the flame code

Description of Experimental trial	Flame code sample	Description
Injection Advance	O_1.1_34mg_104ms/24mg_40.70Psi_165	**O**pen end experiment_ Φ=**1.1_34**mg is injected_ Injection is **104ms** advanced compared to ignition time /**24mg** is injected prior to ignition_**40.70Psi** injection pressure_165 Experiment Number
Injection Delay	C_1.1_69mg_-24ms_43.38Psi_237mm_126	**C**losed end experiment_ Φ=**1.1_69mg** is injected_ Injection is **24ms** delayed compared to ignition time; _ injection pressure is **43.38 Psi_** Flame front at **237mm** from spark at the start of injection_ **126** Experiment Number
No Injections	O_1.1_125	**O**pen end experiment_ Φ=**1.1_** experiment number **126**

4.6. STRATEGY FOR EXPERIMENTS AND THE EXPERIMENTAL MATRIX

4.6.1. Reference trials with a homogeneous mixture

The aim of the study is to investigate the flame propagation in the duct when the mixture is stratified. Initially, flame propagation in the duct is tested with homogeneous mixtures with equivalence ratios of 0.8, 0.9, 1.0 and 1.1. Then the 1.1 equivalence ratio of the mixture is used to investigate stratified flow.

4.6.2. Fuel injections

An extreme situation was observed when flames extinguished with the injected fuel. The delay time to inject fuel was established by some initial trials. Different quantities were injected at this timing to identify the critical fuel mass to be injected for flame extinction.

Once this critical fuel mass was determined, a smaller amount than this mass was injected however the injection timing was varied. The propagation profiles for the conditions were compared.

4.6.3. Air injections

Air was injected to find a critical condition as well. With air injections, the flames did not extinguish, but the formation of the tulip flame at the normal position did not occur. This situation

was identified as the critical condition for air injections. A critical delay time, as well as mass of air, was responsible for this situation

Similar to fuel injections, the air injection timing was altered to identify different flame propagation patterns below the critical condition.

4.6.4. Air-fuel mixture injections

To separate the pure effects of flow disturbances by the gaseous jet, from chemical effects due to injected substances; a mixture of propane and air with an equivalence ratio of 1.1 was injected into the duct. The injection of the mixture was also carried out in the same manner as the fuel and air injections. A distinct deviation from the original flame propagation pattern was identified with mixture injections as well. This critical point was the conditions responsible for displacing the tulip flame as observed in critical air injections. The requirements responsible for the displacement of the tulip-flame was identified and compared with air injections.

4.6.5. Experimental Matrix

The experimental matrix below shows the range of conducted experiments.

Table 25: Experimental matrix

Initial Φ	Exit End	Injections	Mass	Injection Advanced /Delayed	time	Reason
0.8	Open	-	-	-	-	Estimate Base case
0.8	Close	-	-	-	-	Estimate Base case
0.9	Open	-	-	-	-	Estimate Base case
0.9	Close	-	-	-	-	Estimate Base case
1	Open	-	-	-	-	Estimate Base case
1	Close	-	-	-	-	Estimate Base case
1.1	Open	-	-	-	-	Estimate Base case
1.1	Close	-	-	-	-	Estimate Base case
1.1	Open	Fuel	0-50 mg	Delayed	17ms	Identify critical Injection mass
1.1	Open	Fuel	25mg	Delayed	0-20ms	Check Delayed Fuel injections
1.1	Open	Fuel	25mg	Advanced	0-45 ms	Check Advanced Fuel injections
1.1	Open	Air	0-50 mg	Delayed	17ms	Identify critical Injection mass
1.1	Open	Air	25mg	Delayed	0-20	Check Delayed Air injections
1.1	Open	Air	25mg	Advanced	0-45 ms	Check Advanced Air injections
1.1	Open	Mixture	48mg-74mg	Delayed	12.7-20.9ms	Identify conditions to displace tulip flame

CHAPTER 5

5. RESULTS AND DISCUSSION

5.1. FLAME PROPAGATION THROUGH THE DUCT WITH HOMOGENEOUS MIXTURES OF Φ=1.1, 1.0, 0.9 AND 0,8 –OPENED AND CLOSED EXIT END

5.1.1. Introduction

Experiments were carried out for initial Φ= 0.8, 0.9, 1.0 and 1.1 in the duct, for exit end open and closed conditions. The acquired data were; the position of the flame front shown as the distance from the spark end, the pressure variation inside the duct (measured at the spark end), and the time elapsed from the start of flame propagation. 36 experiments were carried out and are listed in Table 37 in Appendix E - 1. The objective of this set of experiments is to understand the flame propagation when the duct is open or closed as well as how the propagation varies with different equivalence ratios. This initial understanding of the flame propagation will serve as a reference to study flame propagation through a duct with stratification.

5.1.2. Correlation between experiments at the same condition to evaluate repeatability

Table 26 shows the correlation coefficients of the interaction of exp. numbers 15,16,17,18, 24 and 25 for Φ = 0.8 open-ended cases and the average correlation coefficient, each experiment, has with the other experiments in the group. The best experiment to represent the group is experiment number 24 with the highest average correlation;

Table 26: Average correlation coefficient calculation

Experiment #	15	16	17	18	24	25	Average Correlation Coefficient
15	1.0000	0.9892	0.9720	0.9651	0.9960	0.9644	0.9811
16	0.9892	1.0000	0.9804	0.9590	0.9925	0.9591	0.9800
17	0.9720	0.9804	1.0000	0.9872	0.9754	0.9857	0.9834
18	0.9651	0.9590	0.9872	1.0000	0.9678	0.9934	0.9787
24	**0.9960**	**0.9925**	**0.9754**	**0.9678**	**1.0000**	**0.9691**	**0.9835**
25	0.9644	0.9591	0.9857	0.9934	0.9691	1.0000	0.9786

Using the same techniques as for the Φ = 0.8 case above, the results for all open and closed ended cases for Φ=0.9, 1.0, and 1.1 were processed and presented in Table 37 in Appendix E - 1. The experiments shown in bold in the table are the ones which are used to represent each group of experiments. These experiments are selected to be analyzed further.

5.1.3. Overview of trials and repeatability

In trials with equivalence ratios 0.8, 0.9, 1.0 and 1.1 a good repeatability of experiments was observed. The AFV Vs Distance graphs have less noise (disturbances) as the equivalence ratio is increased up to 1.1. The luminosity of the flame also increased with the increase of the equivalence ratio. The image processing had less noise when flames with higher light intensity are recorded.

Table 27: Ascending order of the average correlation coefficients

Φ	End Condition	Average Correlation of the total set
0.8	C	0.9990
0.9	C	0.9990
1.0	C	0.9957
1.1	C	0.9957
0.8	O	0.9803
0.9	O	0.9973
1.0	O	0.9940
1.1	O	0.9926

The repeatability of trials is higher for the closed end cases than of the open-end cases. When an open-end trial was done, the FPD is vacuumed, filled with the mixture, then the duct is opened. Due to the exit end being open before ignition a random a variable is introduced. Due to the potential local disturbances generated while opening the duct, the flame travel would be affected. With the variation of the time, the duct stays open before the ignition, the mixture from the duct can diffuse out, creating different conditions at the duct end. Thus more variations among similar open end trials can be expected than of closed end trials, which is evident in Table 27.

5.1.4. The absolute flame velocity diagram

All the experimental data are compared using the Absolute Flame Velocity Vs Distance plot shown in Fig. 32. The instantaneous velocity calculated is the average velocity during a period of 0.1 ms. This velocity has an error of ±10.4mm (Table 11) This large error is due to the very small time interval used to find the average velocity [equation (58)].
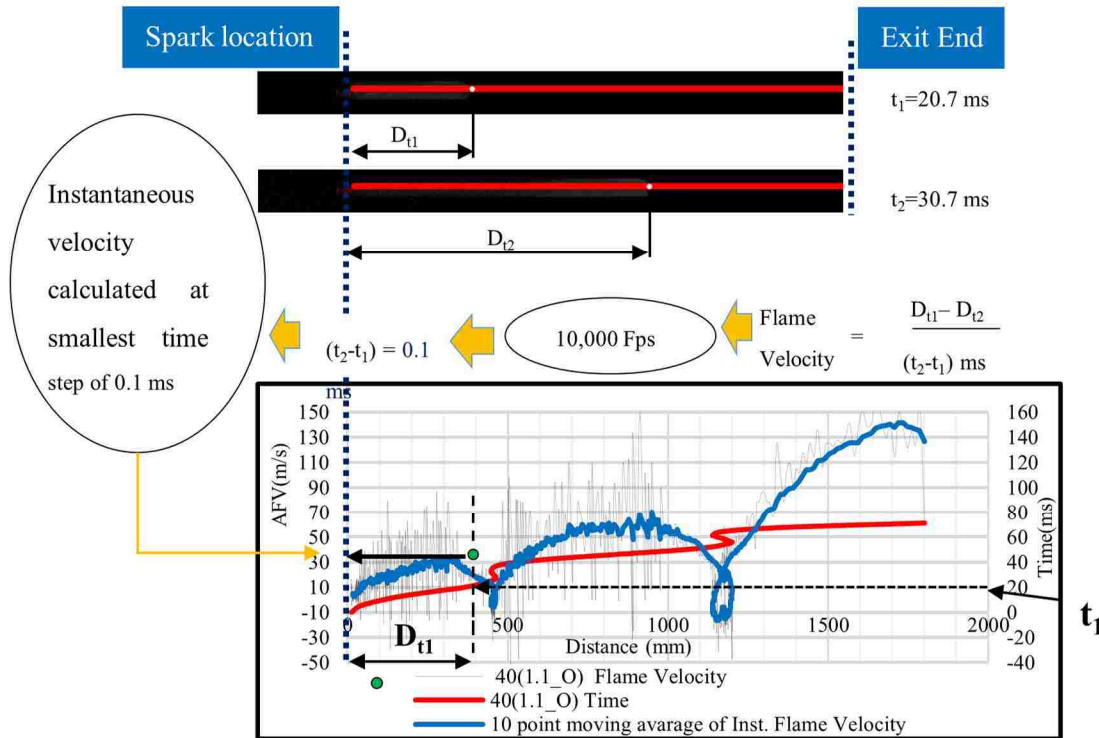
Fig. 32: The AFV Vs Distance diagram

For instance, the minimum error of the flame position could vary by ±0.5 pixels making the possibility of having an error of 1 pixel. If this one pixel will translate to 1 mm and the time interval is taken as 0.1ms, this results in a speed of 10 m/s. Hence the randomness (noise) seen in the diagram does not relate to the actual phenomena, but a processing error. This error is minimized if the time span is increased or the scale is decreased, and the measurement is small. If accurate flame velocities are required a close up image of the concerned area will decrease the scale (mm/pixel) and give a reading with less uncertainty. This can be seen in row 17 of Table 11. In the remainder of the study, the 10 point moving average of the velocity is used to represent and compare different flame propagation patterns.

64

5.1.5. Presentation of initial data

The results of the open end and close end experiments representing the beset trial in each group is shown graphically as plots of the absolute flame velocity, time laps and pressure variation at the ignition end taking the x-axis as the position of the flame front in the center line of the duct. The trials in each group with the highest average correlation coefficient in Table 37 in E - 1 are shown from Fig. 34 to Fig. 37 for open-end cases and Fig. 41 to Fig. 44 for closed–end.

5.1.6. Common propagation patterns of open end cases, the tulip flame and inversions

The flame propagation consists of a sequence of acceleration-deceleration periods. The first such period is identified as the popular tulip flame and the others as the inversions. A sequence of images of the tulip flame and inversions are shown in Fig. 33 A and B. The time lapse from the start of propagation is indicated in each image. The position of the tulip flame and inversion will be referred to as the most negative velocity reached during a single acceleration-deceleration period. These positions are marked in Fig. 34 as vertical dashed lines. The tulip flame and the 1st inversion is marked as A and B respectively in Fig. 34 to Fig. 37. After the formation of the classical tulip flame, the shape of the flame gets distorted this region is identified as the distorted tulip flame by Xiao et al [52]. The first inversion can also be named a distorted tulip flame from the beginning since it can be seen that the tulip flame is more pronounced than the 1st inversion.
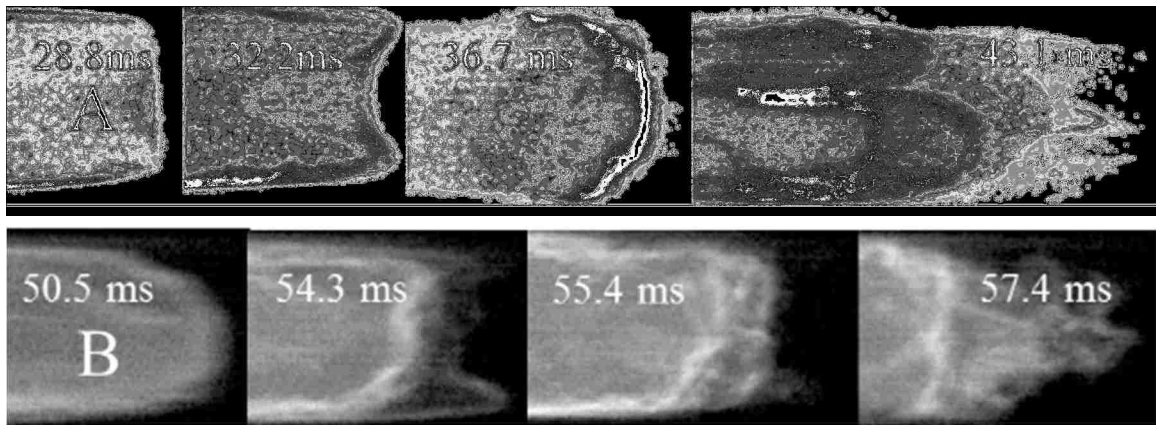
Fig. 33: Image sequence of the tulip flame and the 1st inversion

5.1.7. Comparison of open-ended cases

By inspecting Fig. 34, to Fig. 37 one can observe that the number of inversions has increased with the decrease of the Φ of the mixture. The pressure trace shows a very distinct relationship with the tulip flame formation as well as all inversion developments. A peak pressure at each tulip and inversion location is observed. The raw pressure was filtered at 25Hz.
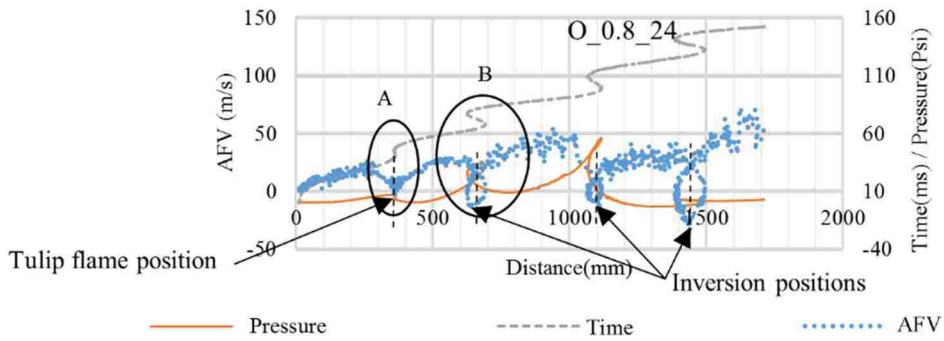
Fig. 34: AFV vs distance for Φ=0.8, exit end opened; experiment #3
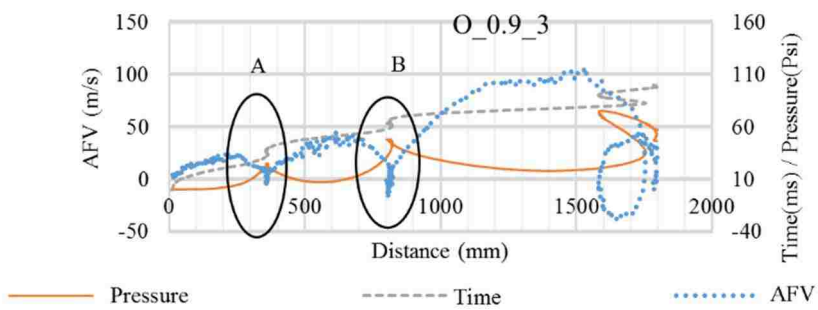
Fig. 35: AFV vs distance for Φ=0.9, exit end opened; experiment #24
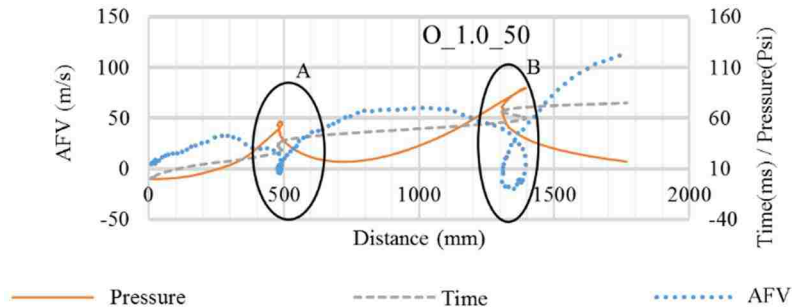
Fig. 36: AFV vs distance for Φ=1.0, exit end opened; experiment #50
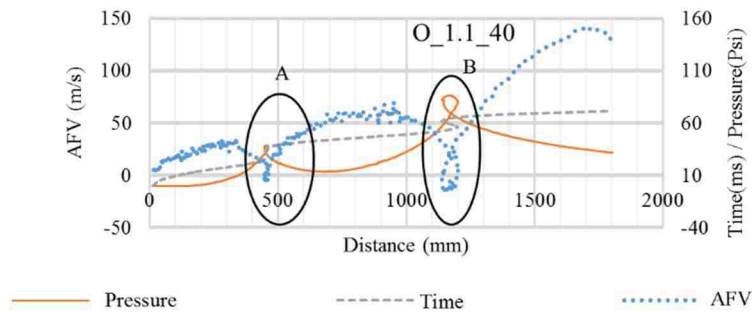
Fig. 37: AFV vs distance for Φ=1.1, exit end opened; experiment #40

66

Fig. 38 shows that position of the tulip flame for Φ = 0.8 and 0.9 occurs around 350 mm from the ignition end while for 1.0 and 1.1, the phenomenon occurs between 500 mm and 450mm respectively. This indicates the tulip flame of lower Φ occurs closer to the ignition.

In the work of Sobiesiak et al. [48] it was shown that in weak mixtures the inversion occurred closer to the ignition end than in more reactive mixtures. Hence, there were more inversions in weaker mixtures than those of more reactive mixtures. The lowest number of inversions were achieved at Φ = 1.1.Fig. 5 shows that the highest laminar burning velocity is achieved at an equivalence ratio of 1.1.
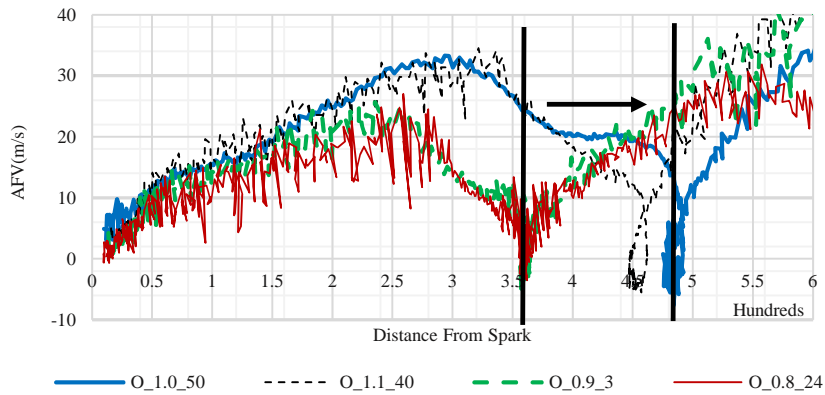
Fig. 38: Position of the tulip flame for open end flame propagation

In this study we have tested mixtures only up to 1.1 since the operating region of most practical combustion devices do not use mixtures of higher equivalence ratios. Accordingly, the position of the tulip flame of Φ = 1.1 (O_1.1_40 in Fig. 33) should be the furthest from the ignition end. However, the position of the tulip flame of Φ = 1.0 is furthest. The Fig. 39 indicates that the time taken to travel through the duct increases with the decrease of equivalence ratio, again except Φ=1.0 being quicker than 1.1. The peak pressures are indicated in Fig. 39. Higher peak pressures are observed for more reactive mixtures and again except 1.1 being slightly less than 1.0. In Fig. 40 and Fig. 37 Φ= 1.1, has a peak velocity in the range of 140m/s, Φ= 1.0 with 110m/s, Φ= 0.9 with 100m/s and Φ= 0.8 with 70m/s. With the case of peak velocities, the order did not contradict with the 1.1 and 1.0 cases as it did for peak pressure and, the tulip flame location.

With the results, one could assume if the case of Φ= 1.0 is more reactive than that of 1.1 contradicting the conclusion that Φ= 1.1 being the most reactive mixture. However, the uncertainty of preparation of the mixture could change the intended mixture equivalence ratio (discussed in section 4.2.3). A mixture of Φ=1.0 to be as high as 1.057 and at the same time a mixture expected

to be Φ =1.1 to be as low as 1.042 The uncertainty can make the mixtures of Φ=1.0 and Φ=1.1 cases to be different from what they are supposed to be.
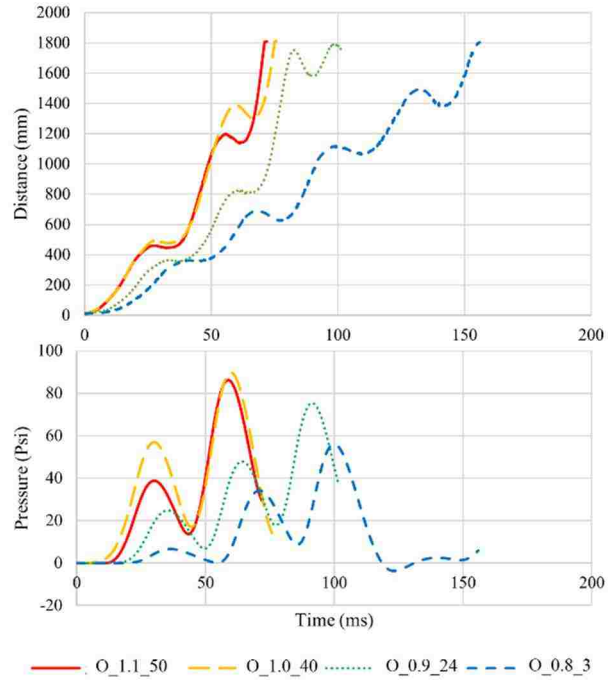
Fig. 39: Comparison of pressure and distance vs time with different equivalence ratios for open exit end
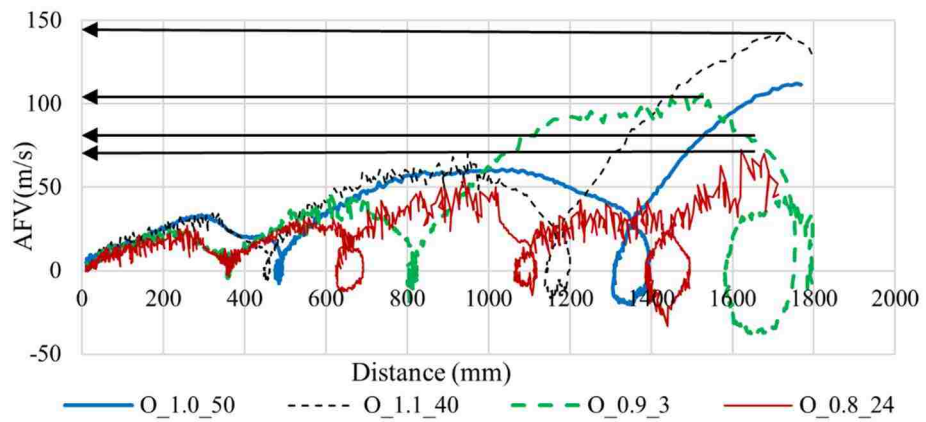
Fig. 40: Comparison of AFV along the duct with varying initial equivalence ratios for open exit end

5.1.8. Comparison of closed-end cases

The flame propagation through a duct in Fig. 41 to Fig. 44 with the exit end closed is different from open end trials. However, Position of the tulip flame showed the same variation as it did with open-end cases. The tulip flame position was closer to the ignition end for leaner mixtures.
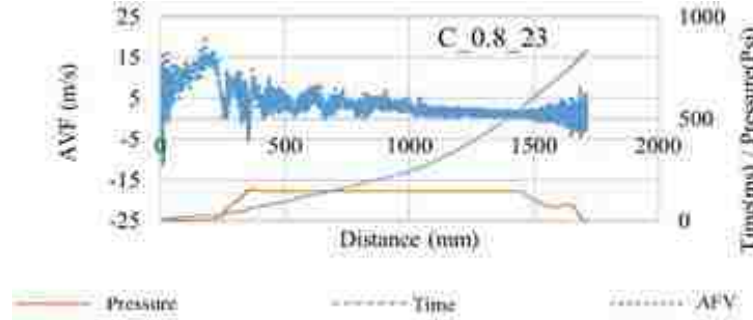
Fig. 41: AFV vs distance Φ=0.8, exit end closed: experiment #23
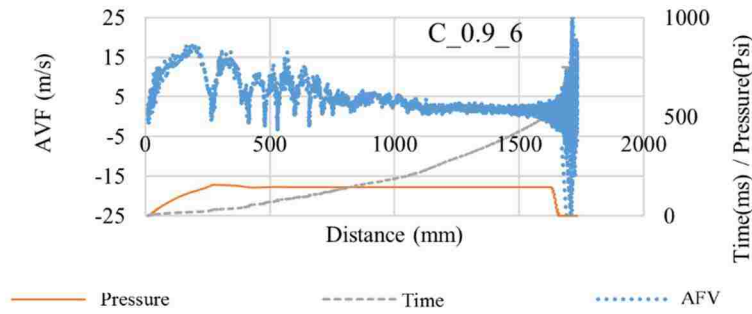
Fig. 42: AFV vs distance Φ=09, exit end closed; experiment #6
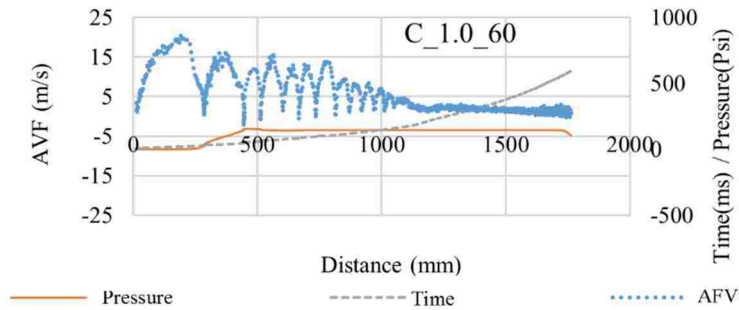
Fig. 43: AFV vs distance Φ=1.0, exit end opened; experiment #60
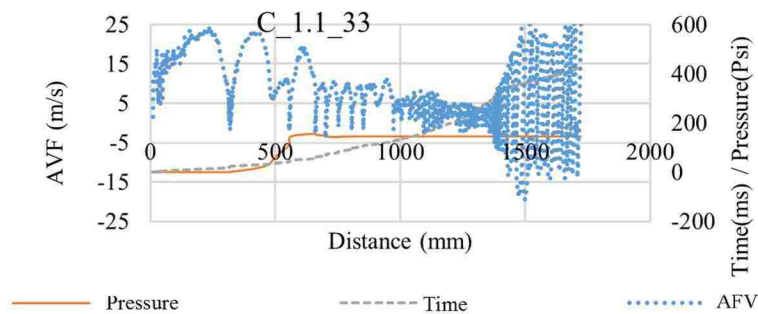
Fig. 44: AFV vs distance Φ=1.1, exit end closed; experiment #33
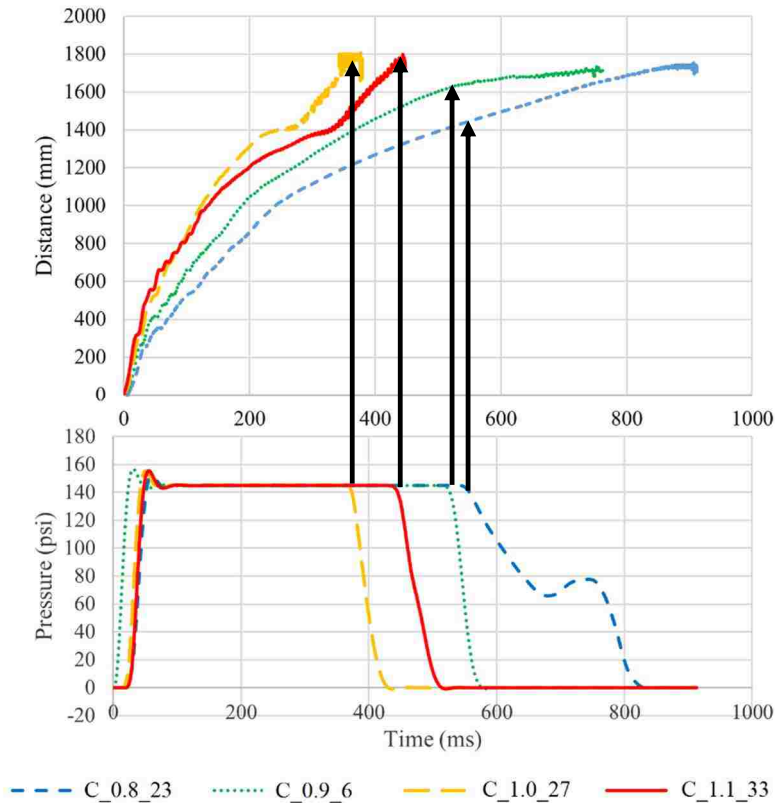
Fig. 45: Comparison of pressure and distance vs time with different equivalence ratios for closed exit end cases

Unlike in the case of pressure oscillations in open-end cases in Fig. 39, the closed end cases show a different pattern in Fig. 45. An initial sharp pressure rise is followed by a period of constant pressure, and then a reduction. The time taken to travel the duct increases with the reduction of the equivalence ratio from 0.8 to 1.1. It is observed that the steep pressure drop occurs right after the flame reaches the end in higher equivalence ratios. However, in lower equivalence ratios, the pressure drop occurs while the flame travels in the duct. In weaker mixtures, the very long time taken to propagate to the end of the duct enhances the hot combustion gasses to cool down before it reaches the end. This cooling down of the combustion products, drops the pressure in the duct before the flame front reaches the end.

Fig. 46 shows closed end trials with different equivalence ratios. The figures indicate that the tulip flame formation still takes place and a large number of inversions occur during every propagation. Similar to open end cases the tulip flame formation in lower equivalence ratios occurs closer to the ignition end.

70
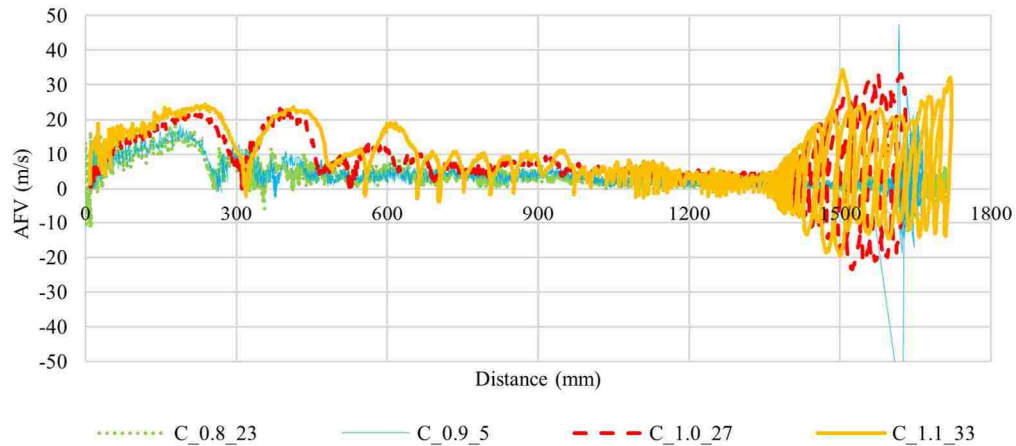
Fig. 46: The AFV Vs distance for Φ = 0.8, 0.9, 1.0, and 1.1 for closed exit end

5.1.9. The analysis of the tulip flame and inversions in open-end and close-end flame propagation

The flame propagation in both open-end and close-end ducts consisted of a sequence of acceleration and deceleration periods. The first such sequence is called the tulip-flame, and the subsequent sequences are termed as inversions. A brief description of the tulip flame and inversions were given in 5.1.6 for open-end cases.

In Fig. 47 the tulip and inversions are shown. The local pressure reaching a maximum at the inversions were very prominent in open end trials. The local maximum pressure is reached when the velocity of the flame fronts drops to a minimum at each sequence. However, in close-end cases, the pressure keeps on rising to reach a constant maximum which is higher than the peak pressure recorded in a closed end trial. A larger number of inversions appear in the close-end case. The tulip and inversions occur during an acceleration period followed by a deceleration period. A local peak velocity is recorded in each sequence. This peak velocity increases in each consecutive sequence in open end trials; in contrary the local peak flame velocity keeps on decreasing in closed end trials. The flame surface area starts increasing as the flame travels towards the exit end of each accelerating period in a sequence. The flame surface is not limited to the front portion of the flame but exists between the side walls of the duct Fig. 48. This increasing surface contributes more to increase the reaction rate and produce even more hot combustion products. The flame front accelerates initially due to accumulating hot combustion products behind the flame front. The turbulence in the duct increases in each consecutive sequence, this increase in turbulence will increase the reaction rates further. The increased turbulence together with the increasing flame surface area will give rise to a larger amount of hot combustion products behind the flame front in

71

each consecutive sequence. In the open end case, higher peak velocities are reached in each sequence due to this reason.
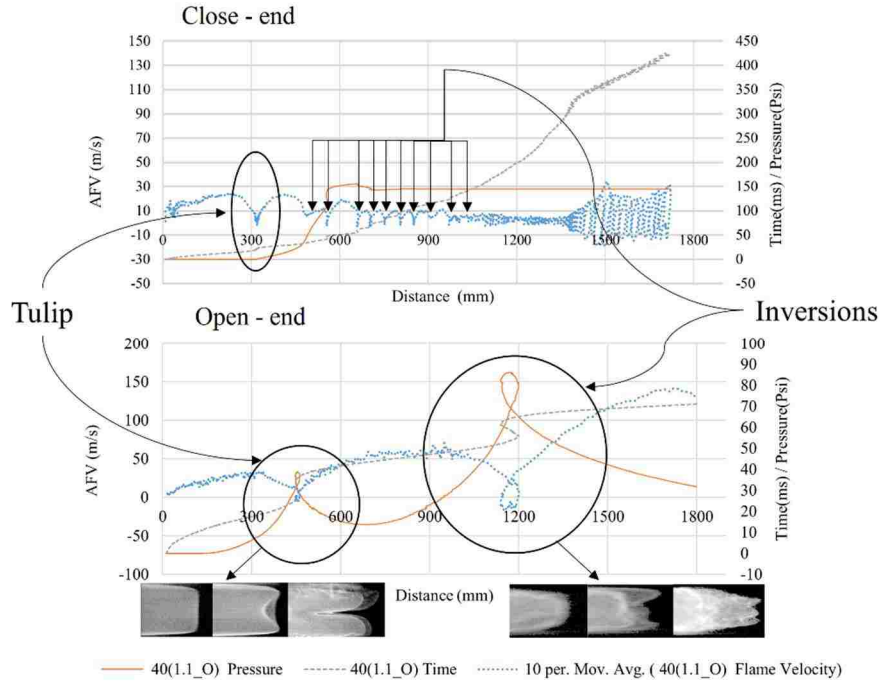
Fig. 47: Tulip and first inversion for Φ=1.1, open -end and close – end trials
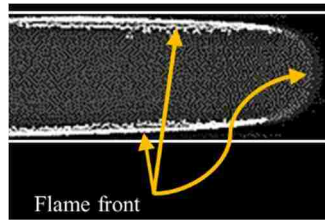
Fig. 48: Flame front existing between side walls

Fig. 47 shows that the pressure inside the tube increases gradually as the flame propagation is initiated in both open-end and close-end conditions. When the exit end is closed the pressure of the reactants also, increases and a lower pressure gradient across the flame front exists. This results in a lower peak velocity at each consecutive sequence in the close-end case.

There are differences in flame propagation in closed end, and open-end ducts. The tulip flame and each subsequent inversion also exhibit differences in open and closed end trials. However, the main reason behind this propagation pattern is believed to share a common explanation. An analysis of the tulip flame formation in an open exit end at an equivalence ratio of 1.1 is used to understand the acceleration-deceleration sequence (Leap Frog phenomenon) in the propagation pattern.

72

Many suggestions have been brought forward to explain this phenomenon which was discussed in detail in chapter 3. In the initial studies, the phenomenon was attributed to the heat loss through the walls of the tube. The pressure waves interacting with the flame front was another suggestion for the formation of the tulip flame. The Richtmyer- Meshkov instability was also considered as the cause of the tulip flame, the instability occurs when a pressure wave traverses the boundary of fluids of two different densities (in this case burnt gas with low density and unburnt gas with high density).

The Darius-Landau instability was proposed by Gonzales et.al [42]; but the Rayleigh–Tayler instability was proposed by several researchers [39,43,62].

The following explanation of the tulip flame formation in an open-end trial is used to explain the mechanism behind this propagation pattern common to open and closed end trials. The initial period of flame acceleration from 0 mm to 300 mm in the open-end case of Fig. 49 is due to the increasing surface area of the flame which accelerates the production of hot combustion products. The expanding hot combustion products push the flame front forward. The expanding hot combustion products accelerate towards the fresh mixture ahead of the flame front. The fresh mixture consists of a lower temperature than the combustion products and has a much higher density than that of the products. The higher density of the fresh mixture resists the push from the hot combustion products. At a distance of 300mm (Fig. 49), the flame front starts decelerating due to this resistance. This resistance causes the Rayleigh-Taylor instability. Hence, the lower density particles accelerating towards the higher density particles triggers the R-T instability; thus at 300mm from the ignition end the R-T instability kicks in.

The conditions for R-T instability are given in equation (28) in chapter 2.4.2 as **αat>0**. where "**α**" = 0.77 (since the density ratio of the fresh gas to burnt gas is ~ 8.08 for Φ=1.1 [47]) and the acceleration "a" of the flame being approximately 2 m/s^2 from Fig. 49.The growth rate of the instability given by equation (29) chapter 2.4.2 as **αat^2** indicates the dent in the middle of the flame front should travel 300 mm backward starting at 18ms (flame at 300 mm in Fig. 49). But for a duration of 14 ms (18ms up to 32 ms) the flame would have travelled 616 mm. (S=ut+0.5at^{2,} u=30mm/ms, a=2mm/ms, 2 t=14ms and S=616 mm) with the same acceleration if the instability did not occur. The summation of these two displacements indicates that the flame travels around 314 mm towards the exit end during this period The experimental results show that the flame has travelled 150mm towards the exit end. The difference can be attributed to the presence of a reaction between the two fluids in this case which is not accounted for in the R-T instability. The comparison was a very approximate one which should be done in more detail.

A comparison of the Taylor-Rayleigh-instability with the flame propagation is shown in Fig. 50. The upper set of images which were shown earlier in Fig. 10 are the simulation result of the. R-T instability. The lower sequence of images in Fig. 50 are for a flame propagation through Φ=1.1. The lower sequence of images actually should be horizontal but to compare it with the upper set of images they have been rotated 90° anticlockwise. These four images are shown again in Fig. 51 which depicts the flame shapes related to different points in the velocity-distance diagram. The
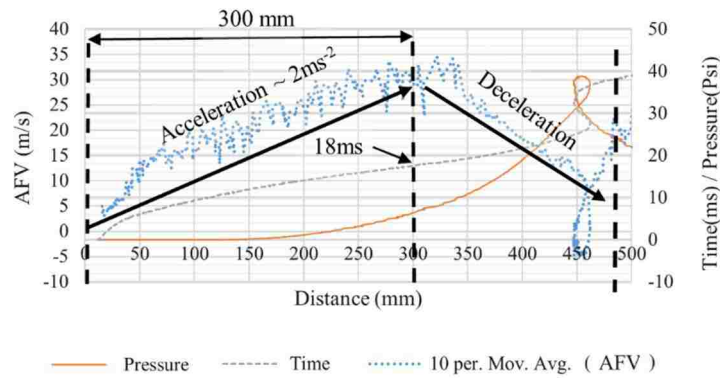
Fig. 49 : Acceleration and deceleration during tulip formation in an open-end case
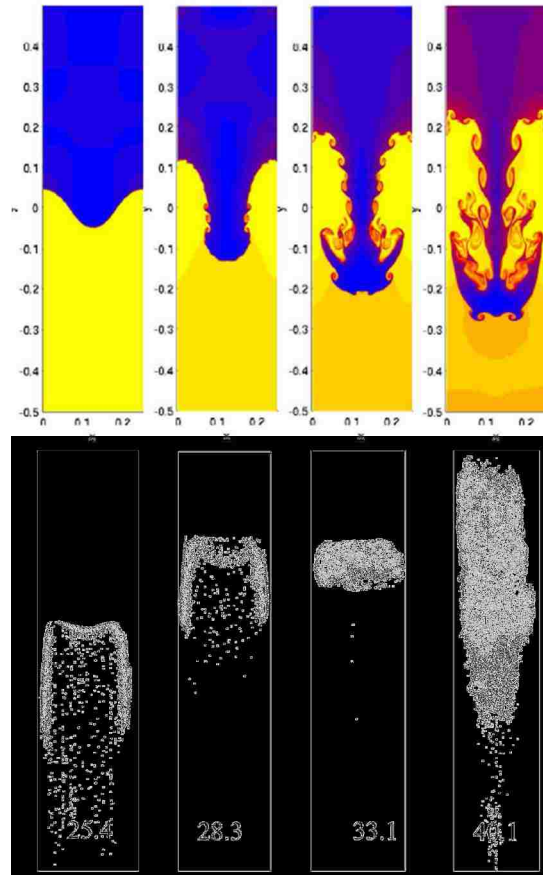
Fig. 50: Comparison of Rayleigh-Taylor instability (upper from 24) with the tulip flame formation (lower)

74

intermediate flame shapes between these images are shown as a sequence of images in Fig. 52. The images can be traced from the time stamp indicating the time from the start of ignition.
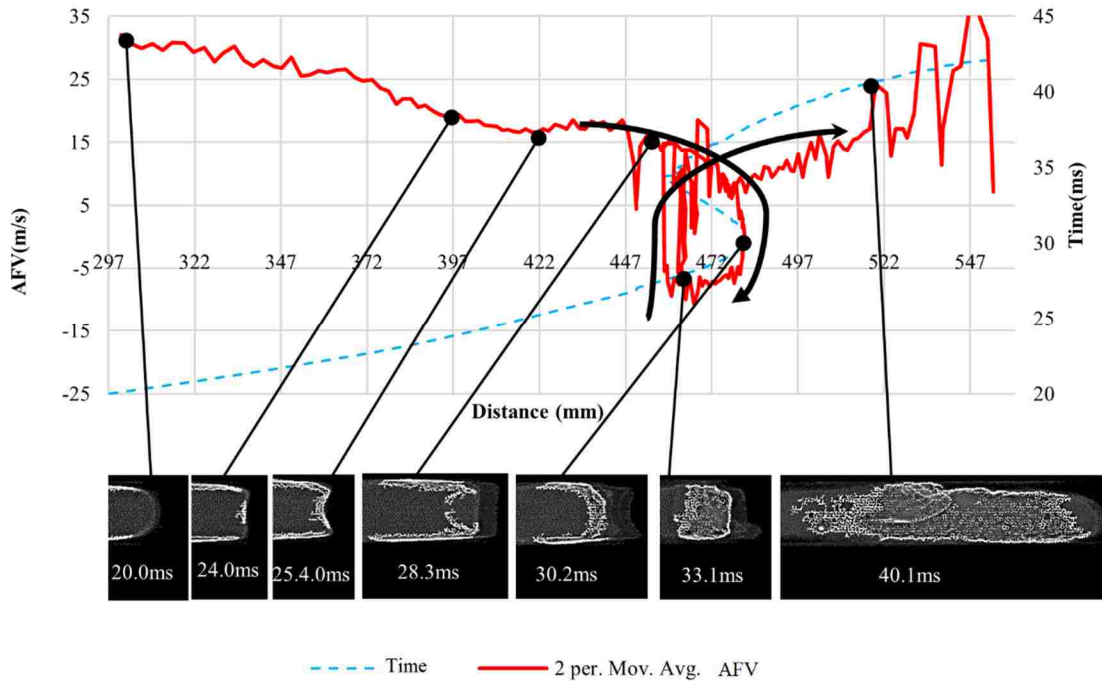
Fig. 51: The shape of the flame front corresponding to the velocity fluctuation along the duct for the tulip formation

In the leftmost frames in Fig. 50 one can see the backward facing cusp formation for both the non-reacting flow (upper row) and the reacting case (lower row), the 2nd set of image shows the deep indentation. Since a reaction takes place in the case of combustion, unlike non-reacting flow, the high-density fluid trapped in the dent, ignites. The backward movement of the flame (33.1ms and 35ms in Fig. 52) occurs when a larger amount of unburnt mixture is trapped in the indentation.

A similar phenomenon is observed in the mushroom cloud created by an atomic explosion where the hot gasses accelerate into the colder atmosphere; this happening is also explained as a consequence of the Taylor- Rayleigh instability.

The heat exchanging at the channel walls [40,63,64], and the shape of the channel will, also, affect the shape of the tulip flame but the formation of the tulip and the inversions can be seen to be influenced, by the Rayleigh–Tailor instability.

However in Fig. 51 the flame shape changes are visible at 24 ms. Between 20ms and 24ms the changes were not observed. For the R-T instability to be very significant, the shape changes should occur right after the acceleration stops. A limitation of this analysis is that we use images from only

one angle, we cannot really tell if the flame changes occur at the front of the flame while we observe a finger shaped flame from the side of the flame front. Therefor the significant influence from the R-T instability can only be attributed only after further studies.
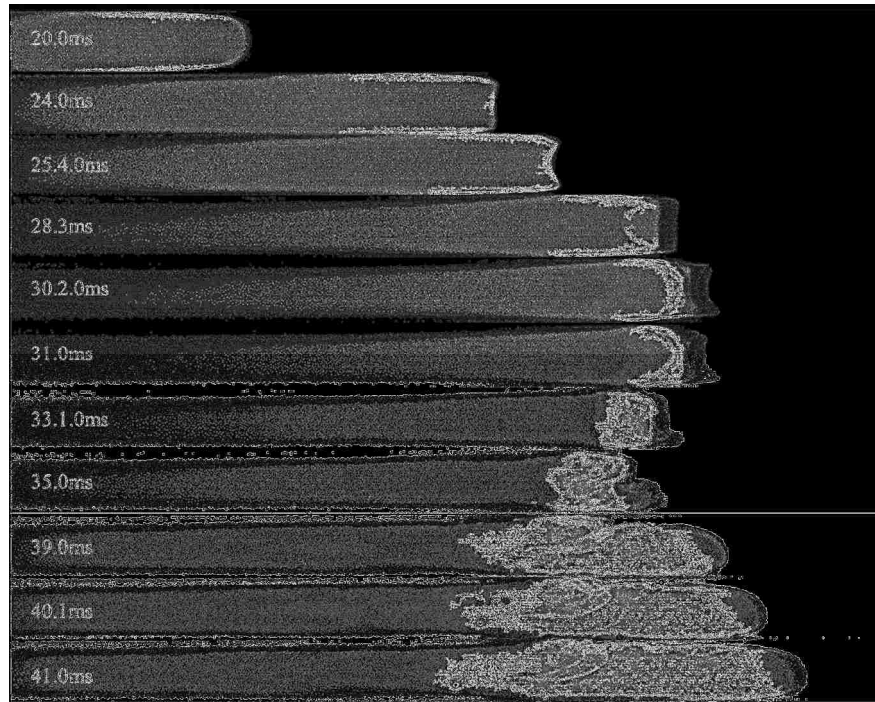
Fig. 52: Formation of the "Tulip Flame" (the time lapsed from the start of ignition is shown)

5.1.10.   Effect of acoustic waves in the formation of the tulip flame

In the experiment described above the pressure signal was filtered using a 25Hz low-pass filter, and yet the pressure trace shows great correlation with the formation of the tulip flame as well as the consecutive inversions (Fig. 34, to Fig. 37). The calculated minimum resonance frequency for the duct is 82Hz shown in Table 18. Since the pressure trace was filtered using a low pass filter of 25 Hz, pressure oscillations over 25 Hz such as the resonance frequency of the duct are not represented in this pressure trace. This indicates that acoustic waves do not affect the tulip nor the inversions. Clanet and Searby [43], adopted the method of changing acoustic time scales by using different lengths of tubes of the same cross section and showed that the length difference did not affect the formation of the tulip flame. Both experiments indicate the same idea that the acoustic resonance frequency of the duct does not affect the formation of the tulip flame.

5.2. FLAME PROPAGATION THROUGH THE DUCT WITH INJECTIONS

5.2.1. Injection process analysis

The objective of this experiment is to investigate the pattern of flow when the injector is triggered and to define the start of injections. The understanding of the injector flow rate is required to correctly time injections to stratify the charge ahead of the injectors. Ten injections with a delay of 18 ms and a pulse of 10 ms were tested. The instantaneous flow was recorded and plotted.

By analyzing the injection flow rate in Fig. 53 the start of injections was defined to be the point where the instantaneous injection has reached 6 SMLPS (large dotted vertical line in Fig. 53). The injector was opened at 18.8 ms and kept open for 10 ms. The number 6 SMLPS was chosen as a standard number to be used in all experiments. A program detects when the instantaneous flow rate increases beyond 6 SMLPS. The time at which the injector is opened is determined using this number. In this experiment, the flow rate reached 6SMLPSs at 18.8 ms
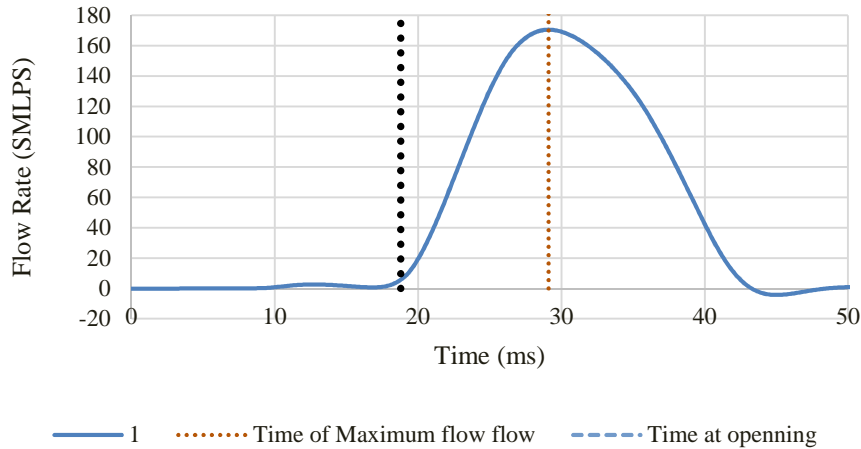
Fig. 53: Instantaneous flow Vs time for a single injection

5.2.2. The variation of injection timing

The standard deviation of the start of injection varied by +/_ 0.42ms. The standard deviation indicates the accuracy of the injection timing. The test indicates that injection time can have an accuracy less than 0.5 ms. The pulse or duration of the injection was 10 ms. Fig. 54 shows the flow rate diagrams of several injections.Table 28 shows the statistical values of the ten injections.
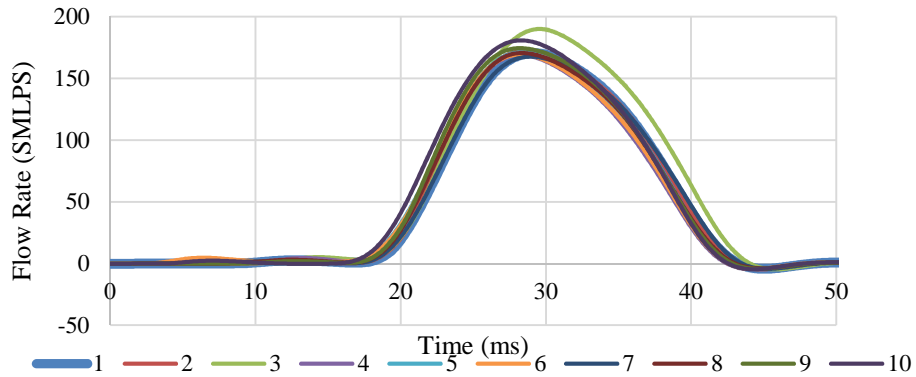
Fig. 54: Ten instantaneous injections with the same delay and pulse settings

Table 28: Statistical analysis of the variation of the starting time of injections for the same settings

Mean start time of injection	18.16 ms
Standard Deviation of start time	0.42 ms
Sample Variance	0.18 ms
Range	1.30 ms
Minimum	17.50 ms
Maximum	18.80 ms
Count	10

5.2.3. Impact of injections

There are two injection process variables that impact the flame propagation; the amount of injected gas and the injection timing. The injection affects the flame velocity using locally altering the equivalence ratio and by altering the flow-field.

Before the injection occurs, the propagating flame induces the flow of the unburned mixture ahead of the flame. The flame velocity varies while propagating along the duct, as shown earlier. This flow is unsteady. The injected air or fuel jet impose its own velocity field on the flow in the duct at the injection site. Some of it spreading initially radially and then being carried downstream and altering the equivalence ratio. The injection pattern was captured in an image for injecting air, shown in Fig. 55. The image shows air jet at the tail of the flame. It illustrates the effect of an injection on the flow field. In this image, the flame propagates from left to right. Because of the late injection, the flow downstream is affected more by the injection. The flow rate of the injector at the time of the image (23.5 ms) was 145ml/s as seen in Fig. 56. The injecting air jet has a velocity

78

in the range of 150 m/s to 250 m/s (the injection velocity is an approximate value). The total mass of air was 45 mg (the dashed line in Fig. 56 indicates the total mass of air injected). The air injection started just before the arrival of flame at the injection site. The image was captured when the injection continued while the flame passed the injection site.
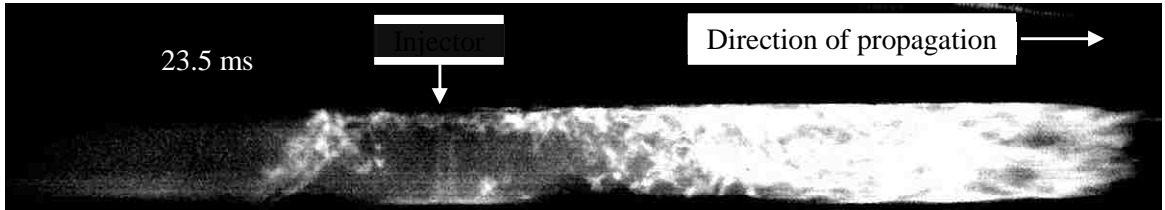
Fig. 55: Image of the injection site 23.5ms after ignition; injection starts when the flame front is 75mm ahead of the injector and continues injecting in trial #311
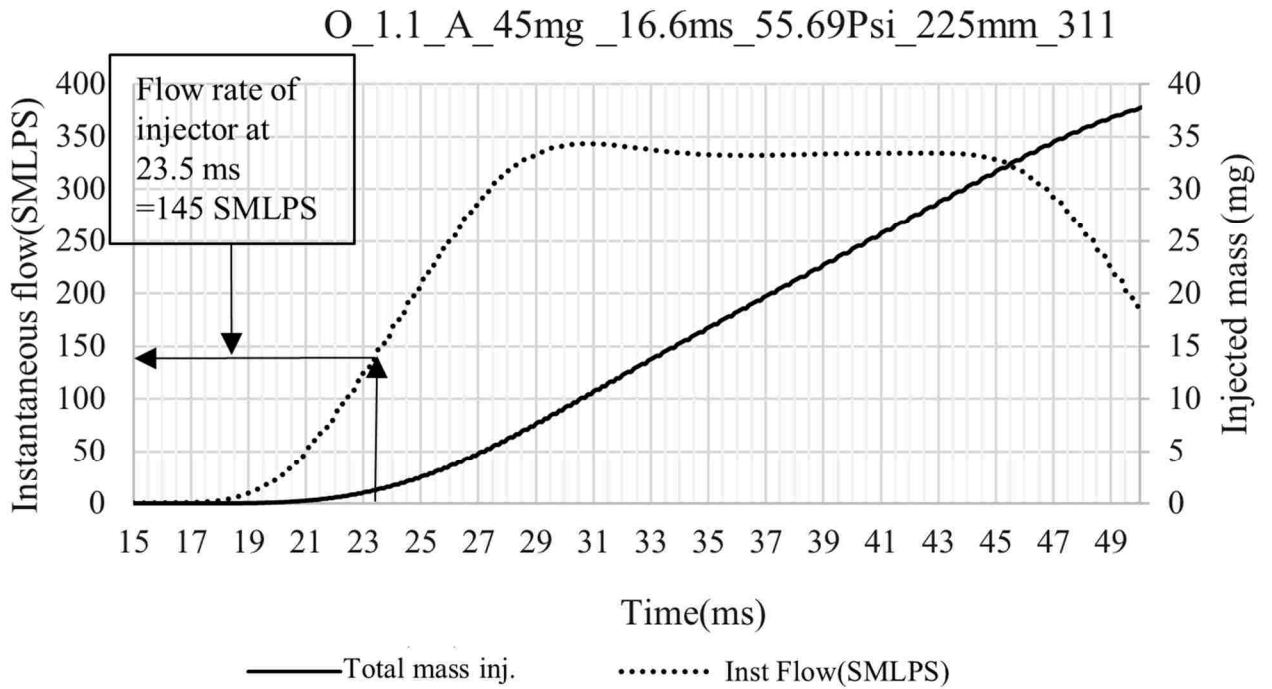
Fig. 56: The details of injection for experiment number 311

79

A simple static species addition model was used to estimate the potential change of the nominal equivalence ratio of $\Phi = 1.1$ when 50 mg of air or 34.6 mg of fuel is added to the volume of the duct cross-section. The x-axis shows the distance from the injector (in the case of the experiment this x value extends upstream and downstream of the injector). Fig. 57 shows the results together with air/propane mixture flammability limits, ($0.51 > \Phi > 2.83$ [65]). Curves in Fig. 57 indicate that air injections will not dilute the mixture below the lower flammability limit. However, if the injected propane accumulates within the length less than 222 mm the mixture equivalence ratio will be above the upper flammability limit. The fuel injections can increase the equivalence ratio above the upper flammability limit.
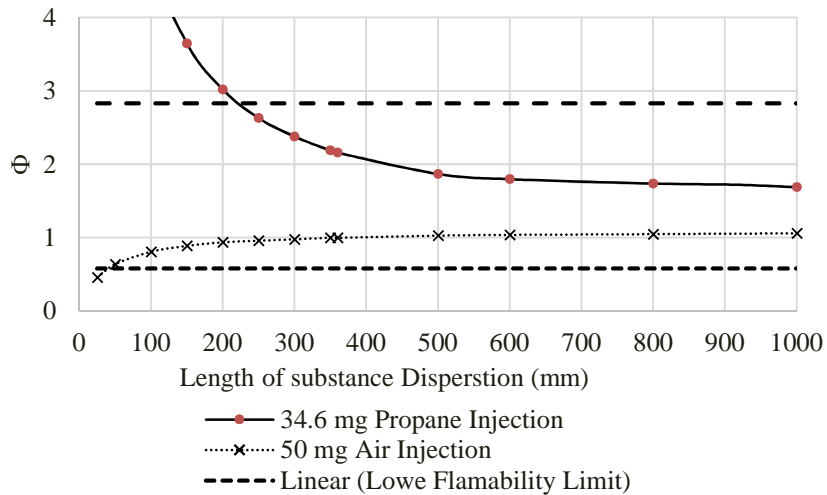
Fig. 57: Calculated Φ within the duct volume at different distances from the point of injection

5.3. VARYING THE MASS OF FUEL INJECTED TO DETERMINE THE CRITICAL MASS OF FUEL TO TERMINATE THE FLAME

5.3.1. Introduction

The stoichiometric air to fuel ratio of the propane-air mixture is 14.7:1. Therefore a small change in the fuel mass will make a larger change in the equivalence ratio. It was observed that large amounts of fuel injected to the duct, extinguished the flame in some initial investigations. Therefore, it was decided to inject different fuel quantities and determine the maximum mass of fuel, which allowed the flame to travel without terminating. This mass is termed as the "critical mass." Table 38 in Appendix E - 2 shows the list of experiments. The injection timing was fixed at a 17.5ms delay. But due to the variation of the starting time of the flame and different flame propagation speeds, the position of the flame front at the time of injection start varied significantly.

5.3.2. Results and discussion

Fig. 59 shows the AFV variation along the duct for the cases where the flames terminated when a large amount of fuel was injected. Fig. 59 shows a further analysis of the result. Fuel injections above 34mg have terminated the flame before the exit. The Higher amount of fuel terminated the flames at a shorter distance upstream.
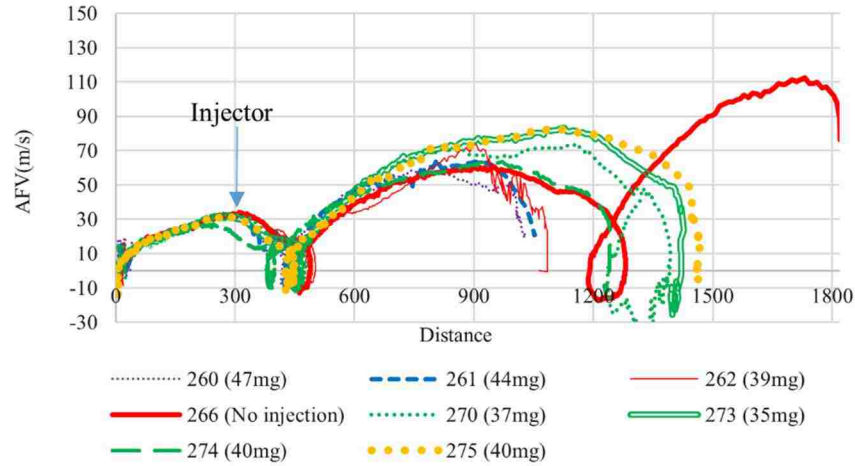
Fig. 58: AFV vs distance diagram for the cases with flame terminations for delayed fuel injections
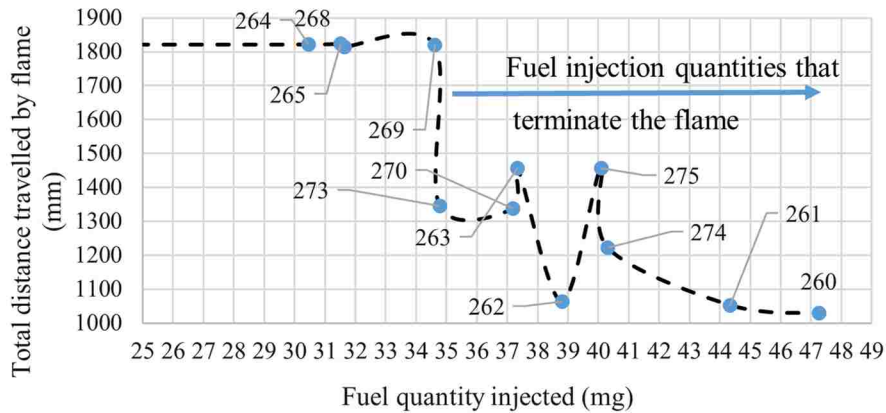
Fig. 59: The variation of total distance travelled by the flame before extinction for varied mass of fuel injected to the duct (Trial number shown in figure)

.Table 39 in Appendix E - 3 shows a summary of the results of experiment numbers 261 to 276. Fuel injections increase locally, the effective equivalence ratio of the duct. The position of fuel particles along the duct decides the local equivalence ratio. Fig. 59 shows that in the experiments 260, 261, 263, 270, 273, 274 and 275 the flames are terminated before reaching the exit end of the duct. Also, note in Fig. 58 it indicates that all of these flames terminated towards the end of the deceleration period of the 1st inversion.

81

Fig. 60 provides details of the experiment number 273 shown in Fig. 58 and Fig. 59; one of the flames which were terminated with a high amount of injected fuel. The distance of flame front position from the ignition end (in mm), instantaneous injection mass of fuel (in SMLPS) and the cumulative fuel injection mass (in mg) at a given time is indicated in this diagram. The mass of fuel injected when the flame is at the injector is only 1mg. A greater mass of fuel of 29.21 mg has been injected after the flame has passed the injector. The flame is extinguished 1346mm downstream of the duct or 1046 mm from the injector.
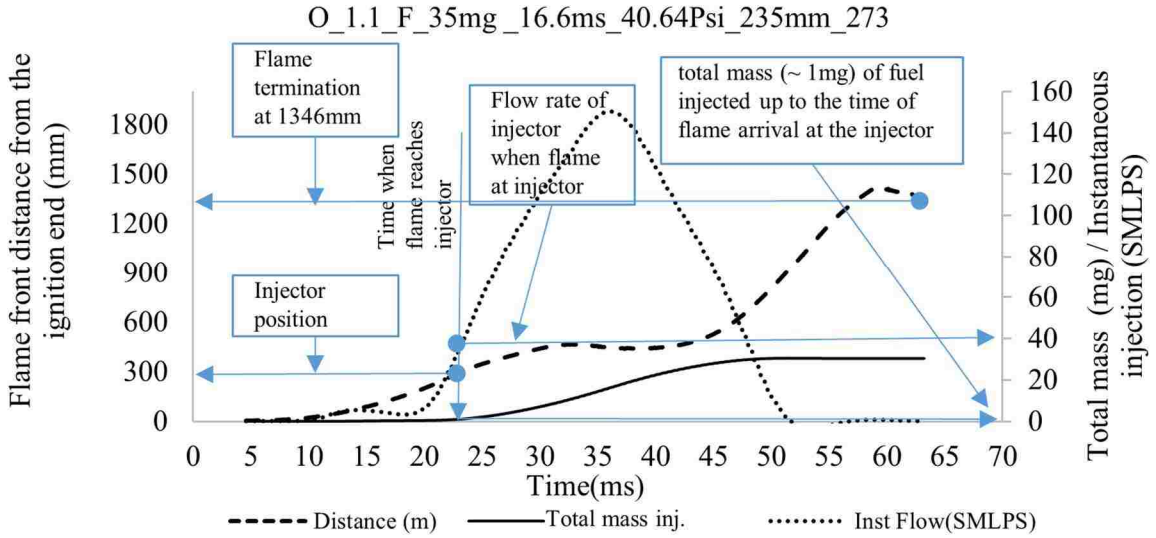
Fig. 60: Injection and the distance of the flame front variation Vs time, for experiment 273

The model shown in Fig. 57 indicates that the equivalence ratio of the duct does not increase beyond the flammability limit at a distance more than 1000 mm from the injector position. However, this model does not account for flow in the duct. In Fig. 58 one can see that flow speed inside the duct when the flame passes the injector is around 30m/s. This flow can transport the injected fuel faster than predicted by the model. Fig. 55 shows how the injected gas spreads more towards the direction of flame travel rather than dispersing symmetrically.

It was earlier noted that all the flames are terminated during the deceleration period of the 1st inversion. One can see that some unburnt gas moves towards the reverse direction and penetrate the burnt region at the inversion, this was explained in 5.1.9 (The analysis of the tulip flame and inversions in open-end and close-end flame propagation). The fuel injected behind the flame front can increase the unburnt mixture. The equivalence ratio can be increased to the upper flammability limit at1046 mm away from the injector. Fig. 61 illustrates the higher equivalence ratio region

82

expected in the duct. The fuel arriving behind arriving with the injection also can enrich the secondary reaction zone [55] affecting the reaction rate at this zone as well.
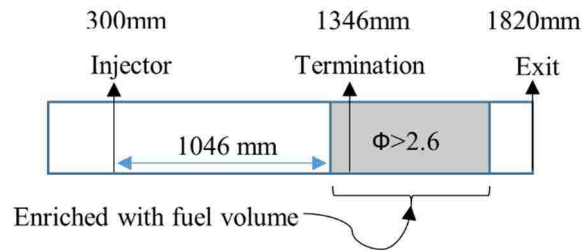
Fig. 61: Schematic diagram of the flame termination of experiment 273

One can also expect the injected gasses to quench the flame. If the injected fuel reaches the flame front from behind, the flame front will lose energy to the cool fresh mixture ahead of the flame and behind the flame. If the reaction region cannot keep up with the outflow of thermal energy to support reactions, the flame can quench at this location

5.4. VARYING THE TIME BETWEEN IGNITION AND FUEL INJECTIONS WHEN LESS THAN THE CRITICAL MASS IS INJECTED

5.4.1. Introduction

The subsequent experiments are focused on the flame propagations with the fuel injections at varied timings. To ensure that the flames did not extinguish before the exit end, the injected fuel mass was maintained close to 27 mg, well below the critical mass of 34.6 mg. The injection delay and advance were varied.Table 40 in Appendix E - 4 shows the list of experiments carried out.

The objective of the experiment was to examine how the flame propagation changes when fuel injections are delayed or advanced relative to the ignition time.

5.4.2. Results and discussion

Fig. 62 and Fig. 63 show the propagation patterns when fuel injection advance and delay is varied. It is noted that the position of the 1st inversion changed with the varying of ignition delay and advance. Long delays and very short advances resulted in the inversions pushed towards the exit end. Two effects of these injections were noted. (Fig. 62 and Fig. 63)

1. The AFV of the propagations started to deviate starting from 600mm in delayed injections and 800 mm in advanced injections.
2. The first inversion was relocated when injection advances and delays were varied.
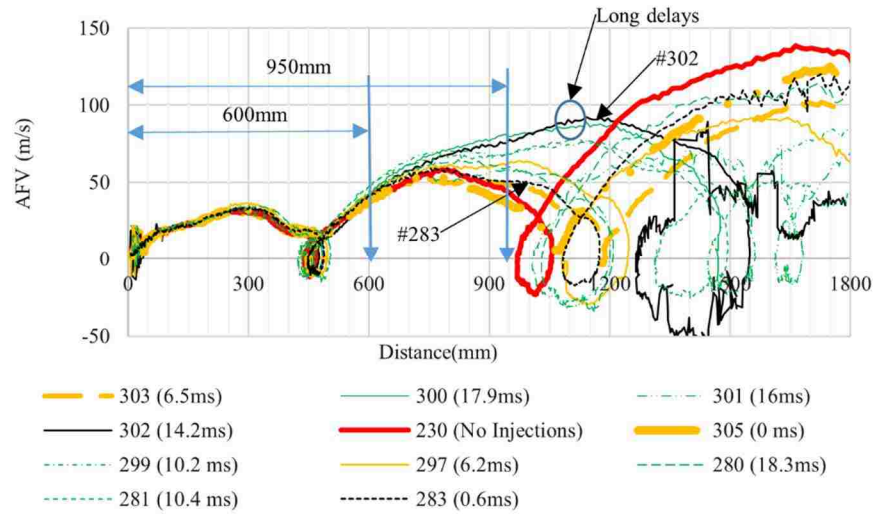
Fig. 62: Flame propagation profiles for varied delayed injections of 26.9 mg fuel
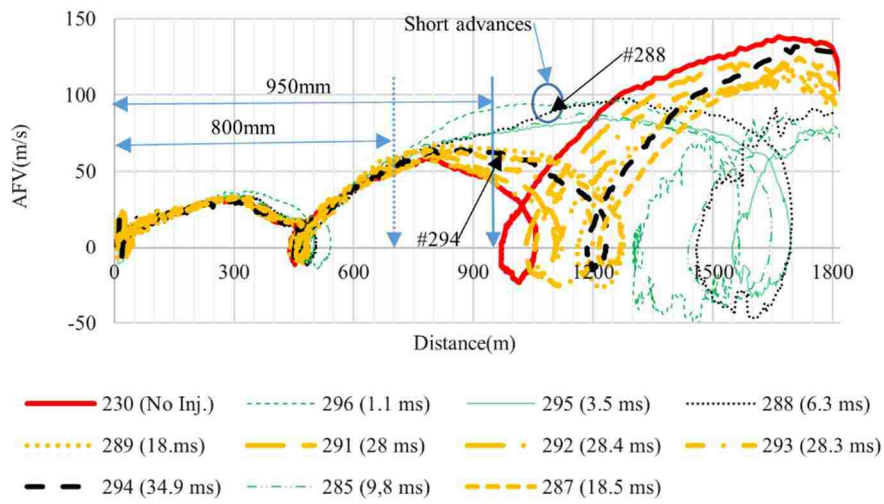
Fig. 63: Flame propagation profiles for varied advanced injections of 27 mg fuel

In both advanced and delayed injections, the first acceleration-deceleration period is unchanged. The AFV remained almost the same until the propagation patterns start an interesting deviation jest after 600mm in the delayed injections (Fig. 62) and after 800mm in advanced injections (Fig. 63). The deviations become very prominent at a distance of 950mm from the ignition end in both cases. Hence AFV at 950mm position in the duct (shown in both images) was chosen to investigate further. Fig. 64 shows the plot of the position of the first inversion with the AFV at 950 mm from the ignition end. There is a good correlation between the position of the inversion and the flame velocity at 950mm from the ignition end (R^2=0.7437). This indicates that the higher the velocity increase of the flame after the tulip formation the further downstream does the 1st inversion is positioned. Hence this velocity can be taken as a measure to indicate the position of the inversion. Circled cases in Fig. 65 and Fig. 66 shows that for a very small advance and a very small delay
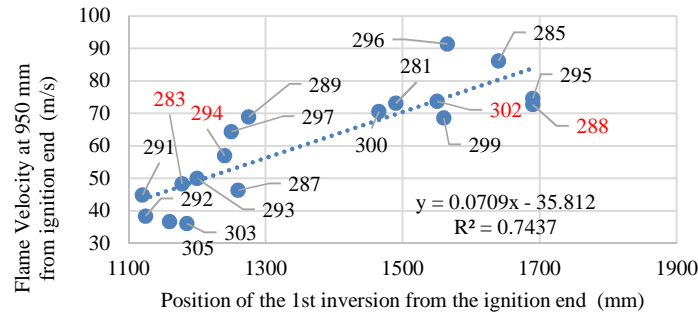
Fig. 64: Position of the first inversion vs the absolute flame velocity at 950 mm from the ignition end

there is a drastic difference of the position of the first inversion. For Injection delays less than 10 ms (#283 Fig. 62 and Fig. 65) the position of the first inversion is closer to the Ignition end. Fig. 67 shows that the flame reaches the injection site closer to the maximum fuel flow of the injector (73% of the maximum flow) the flame interacts with the injecting fuel. The mixture composition at the flame front becomes highly fuel rich. This can make the reaction rate of the flame front quite low. (fuel particles have less access to oxygen particles). As a result, the flame propagation speed can slow down. In the case of advanced injections, less than 10 ms (#288 of Fig. 63 and Fig. 66) unlike in the delayed injections the position of the 1st inversion is further downstream. In Fig. 68
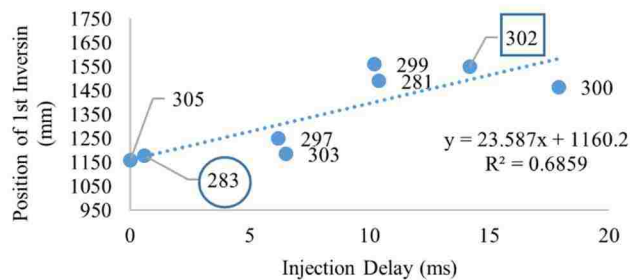
Fig. 65: Position of the first inversion for varied delayed fuel injections

85

when the flame reaches the fuel injection site the fuel injection is almost complete (24% of the maximum flow) and the rate of injection is very low.
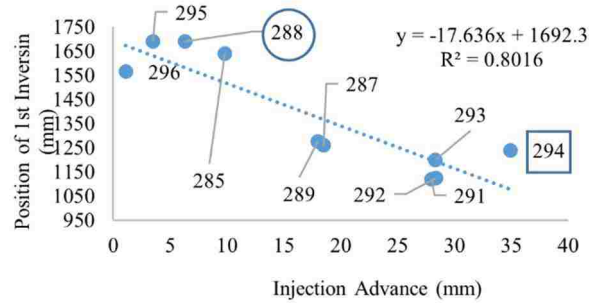
Fig. 66: Position of the first inversion for varied advanced fuel injections of 27 mg
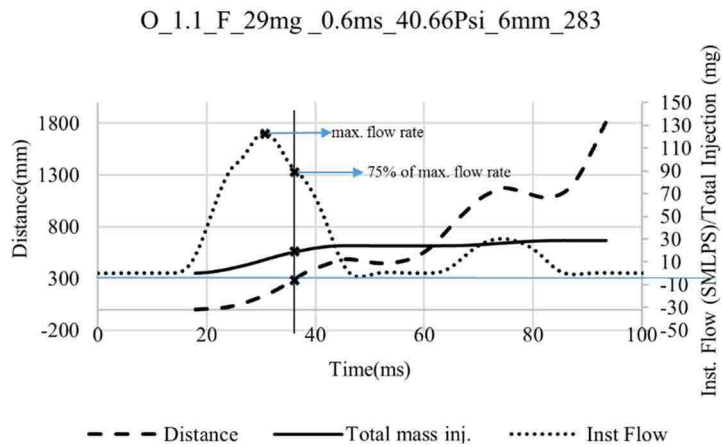
Fig. 67: Time Vs velocity diagram for #283 for a fuel injection with a very small delay (0.6ms)
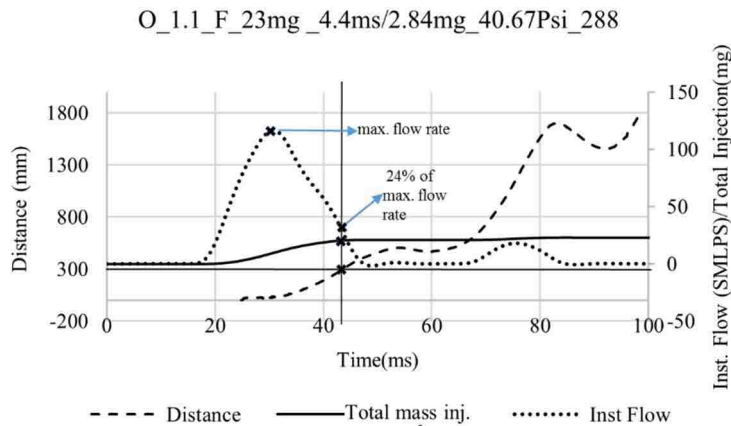
Fig. 68: Time Vs velocity diagram for #288 for a fuel injection with a very small advance (4.4ms)

The interaction of injected fuel with the flame is quite low compared to # 283. (comparing these two situations one can see that the AFV at 950 should be higher for #288 than for #283, which indeed is the case (Fig. 64). Accordingly, the first inversion for #288 is located at 1690mm and that of #283 at 1178 mm. The first inversion is shifted 512mm due to the stronger interaction of the flame front with the fuel injection. The other extreme cases are #302 and #294. Their details are shown in Fig. 69 and Fig. 70 and respectively. In case 302, only a very small amount of fuel is injected before the arrival of flame, most of the fuel is injected behind the flame compared to case 283. As a result, the average AFV at 950mm is higher for #302 case, and the 1st inversion is further downstream of the duct. In case 294 about 80% of fuel has been injected before the ignition. In this case, the injected fuel has time to increase the local equivalence ratio by a large amount before the start of flame. The injected fuel will increase the equivalence ratio even before the start of the flame. The very high equivalence ratio reduces the laminar flame speed of the flame which in turn reduces the AVF at 950. Therefore, the first inversion of case 294 is located closer to the ignition end than the case 288. The flow rate of the injector when the flame is at the injector is far lower in case 294 resulting in less turbulence as well.
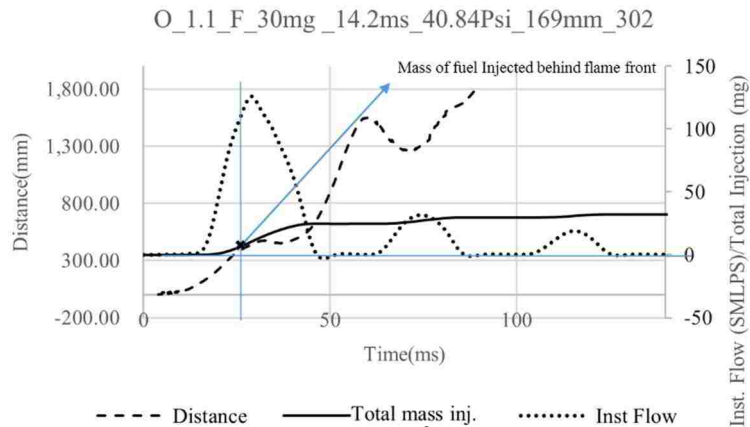
Fig. 69: Injection and flame propagation pattern for a 14.2 ms advanced fuel injection for trial #302
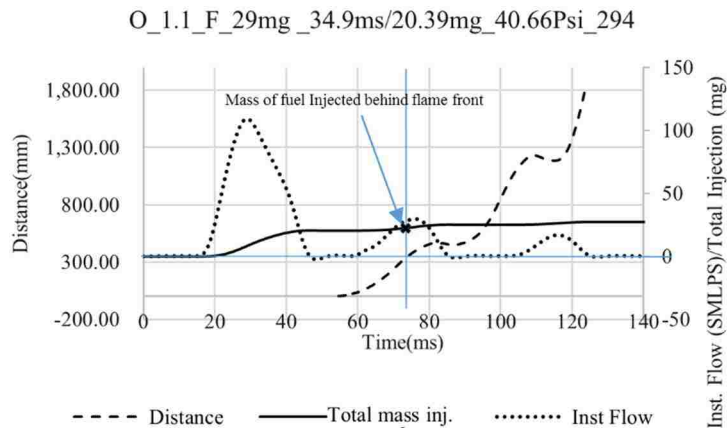
Fig. 70: Injection and flame propagation pattern for a 34.9 ms advanced fuel injection for trial #294

87

5.5. VARYING THE MASS OF AIR INJECTED TO DETERMINE THE CRITICAL MASS OF AIR TO DISPLACE THE TULIP FLAME.

5.5.1. Introduction

Unlike for the fuel injections, the injection of air into the duct did not decrease the equivalence ratio up to the lower flammability limit. Flames did not extinguish with injections of air, but the flame propagation profile displayed significant variations with higher amounts of the injected air. The air injections were delayed by 14.8ms (±3.5 ms). The timing could not be exactly fixed since the flame initiation contributes to this variation. Table 41 in Appendix E - 3 shows the list of experiments. With the variation of the injection times (±3.5 ms), the flame position at the start of injection varied.

5.5.2. Results and Discussion

When a mass of air over 37 mg is injected, the tulip-flame is displaced towards the exit end of the duct Fig. 71. When an air mass less than 37 mg is injected, the tulip flame location is not altered (Fig. 72).

The position of the tulip flame formation with the position of the flame front at the start of injections is displayed in Fig. 73. The variations of tulip flame position with the injected air mass is shown in Fig. 74.The objective is to identify a critical mass of air to be injected to transform the propagation profile significantly.
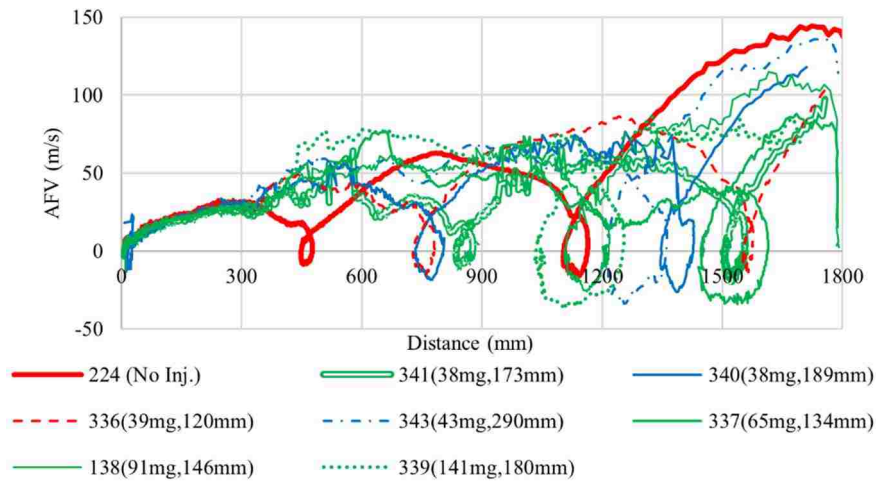
Fig. 71: Propagation profiles for air injections over 34.6 mg
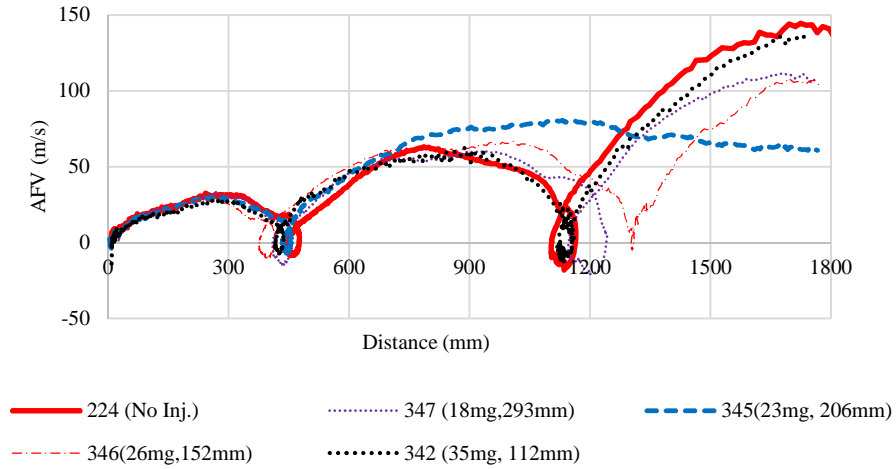
Fig. 72: Propagation profiles for air injections less then 34.6 mg
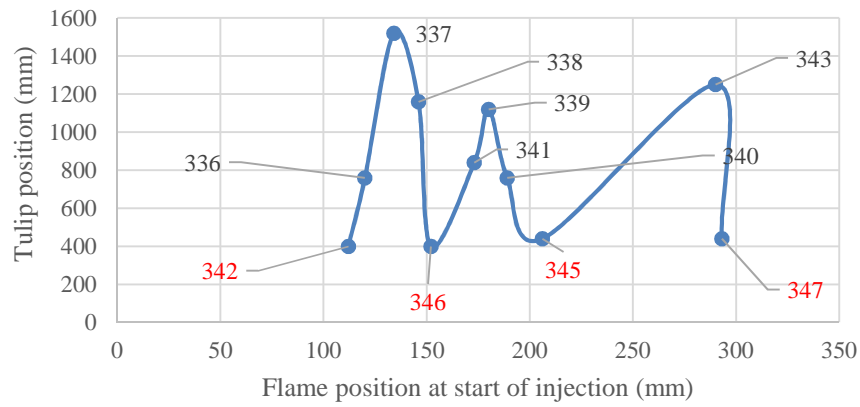
Fig. 73: Variation of the position of the tulip with position of the flame at the time of starting air injections
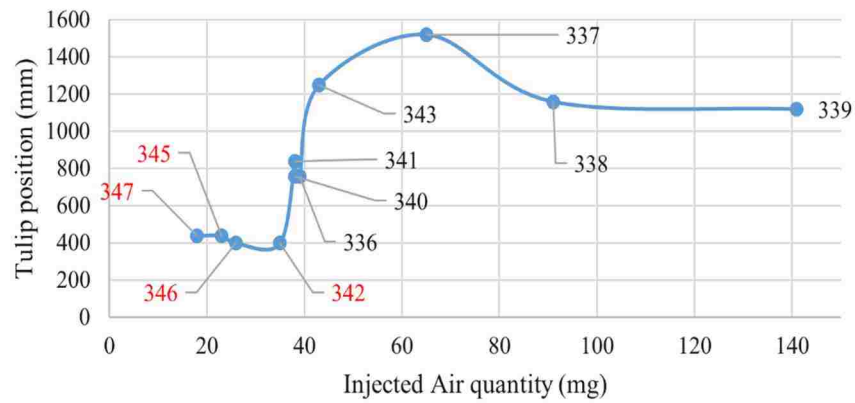
Fig. 74: Variation of the position of the tulip with different quantities of air injected

89

Fig. 75 shows the injection details of case 337 shown in Fig. 71, Fig. 73 and Fig. 74. The flame arrives at the injection site when the injection is 60% of its maximum value. 65% of the injected air is injected behind the flame front. Unlike for the fuel injections where the flames were extinguished in a similar initial condition (Fig. 60), the flame accelerates. The tulip flame occurs at 1400 mm distance from the ignition end. The tulip formation is displaced 1100mm towards the exit. The injected air mass is 1.8 times the fuel mass injected in case 273 shown in Fig. 60. Unlike for the fuel injections, the flame is not extinguished. The increased flow from the injection and the increased laminar flame speed due to higher turbulence can displace the tulip downstream The cool air behind the flame front increases the density of the burnt gasses behind the flame front. This increment in density can change the Atwood number (paragraph 2.4.2) due to a reduced density ratio. Since the formation of the tulip has been attributed to the R-T instability, the change in the position can also be influenced by the change in density of the burnt gasses behind the flame front.
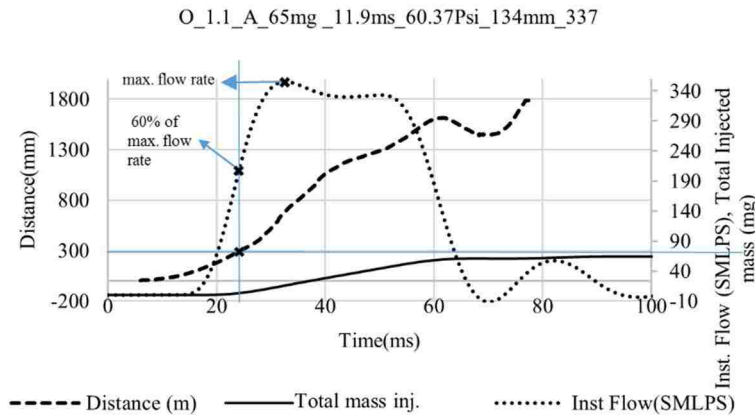
Fig. 75: Injection profile and distance of flame from the ignition end for 65mg of air injected when the fame front was at 173mm from the ignition end in trial # 337

5.6. VARYING THE TIME BETWEEN IGNITION AND AIR INJECTIONS WHEN LESS THAN THE CRITICAL MASS IS INJECTED.

5.6.1. Introduction

Table 42 in Appendix E - 6 shows the list of experiments carried out to examine flame propagation when 34 ± 0.8 of air is injected at different timings with respect to the spark release. The mass of air was used to keep the flame propagation below the "critical injection mass" (37 mg) in paragraph 5.5 above. The objective of experiments is to investigate how the flame propagation changes when air is injected at different times with respect to the spark release when injected below the "critical mass" of air, for both advanced and delayed injections.

5.6.2. Results and discussion

The air injected makes the local air/fuel mixture locally lean. Fig. 57 in section 5.2.3 shows the

variation of Φ with the distance for a 34.6 mg air injection. The analysis indicates that the air injections will not shift the local equivalence ratio towards the lower flammability limit.

Fig. 76 to Fig. 78 show the similarity of propagation pattern in each category when the cases were categorized according to the injection timing. The position of the first inversion has a distinct relationship with the injection timing. For fuel injections, advanced injections and delayed injections reacted differently, but with air injections only the magnitude of the advance or delayed mattered, it seemed that the injection being advanced or delayed didn't matter. Especially for very short advanced injections and delayed injections, the variation of the position was different in fuel
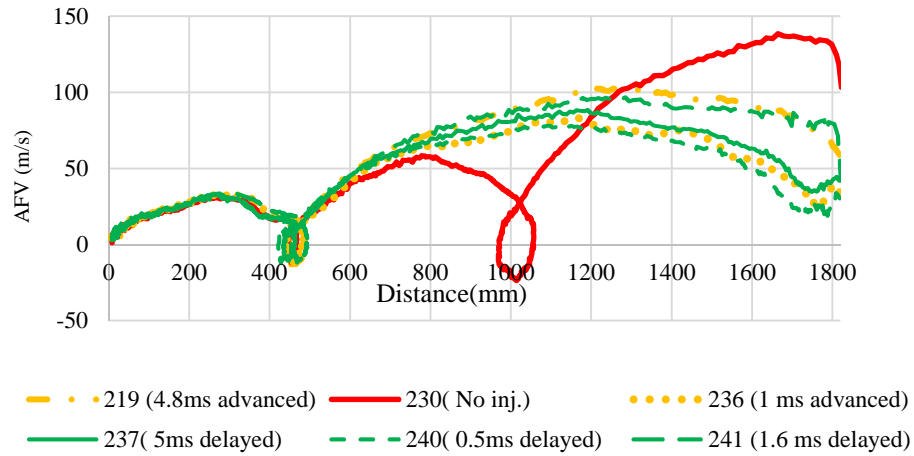
Fig. 76: Comparison of AFV for delayed and advanced air injections below 5 ms
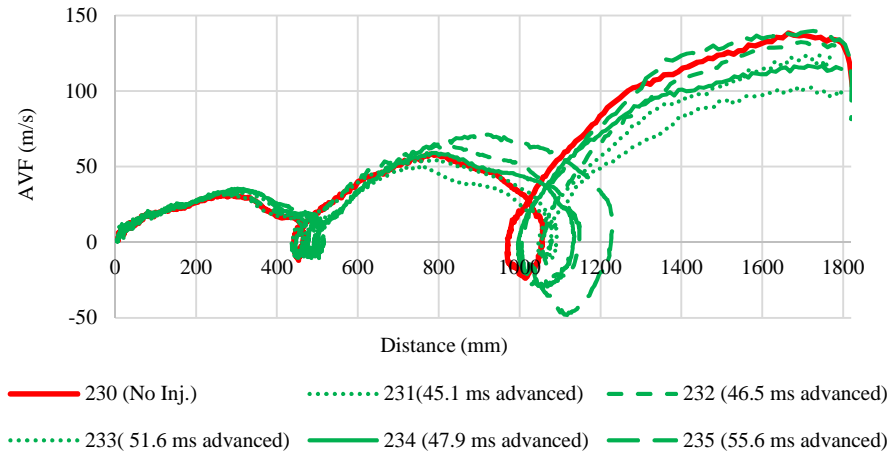
Fig. 77: Comparison of AFV for delayed and advanced air injections 5ms -40ms

91
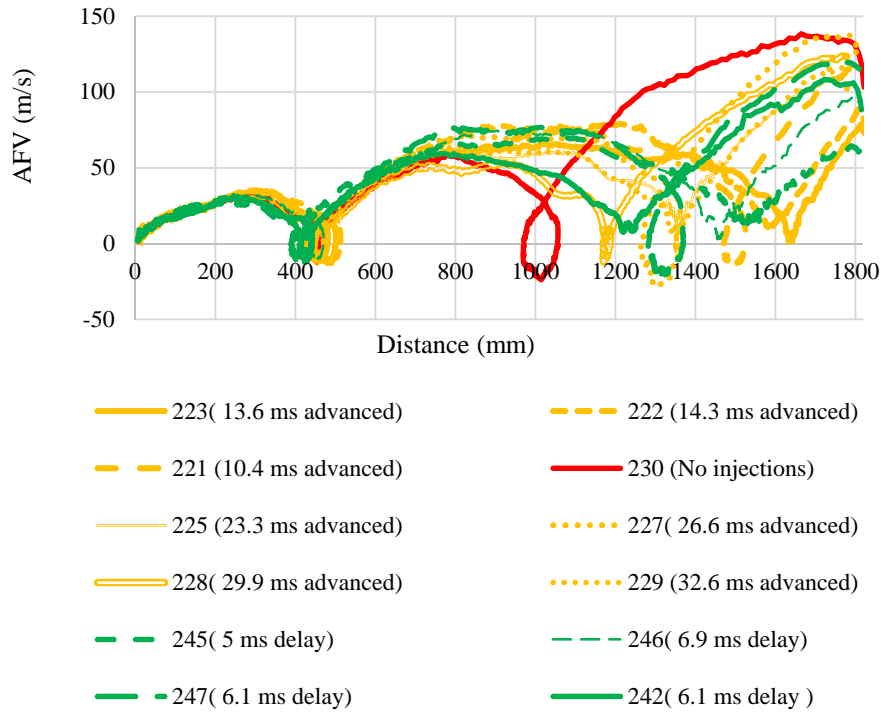
Fig. 78: Comparison of AFV for delayed and advanced air injections more than 40ms

injections. In Fig. 65 experiments 305 and 283 for very short delayed fuel injections, the first inversion, occurred around 1150mm from the ignition end. In Fig. 66 for very small advanced fuel injections (295 and 288), the first inversion, was close to 1600mm. For air injections with the same timing, this does not occur. In Fig. 79 the first inversion formed close to the end of the duct (241 and 219) for delayed and advanced below 5ms respectively.
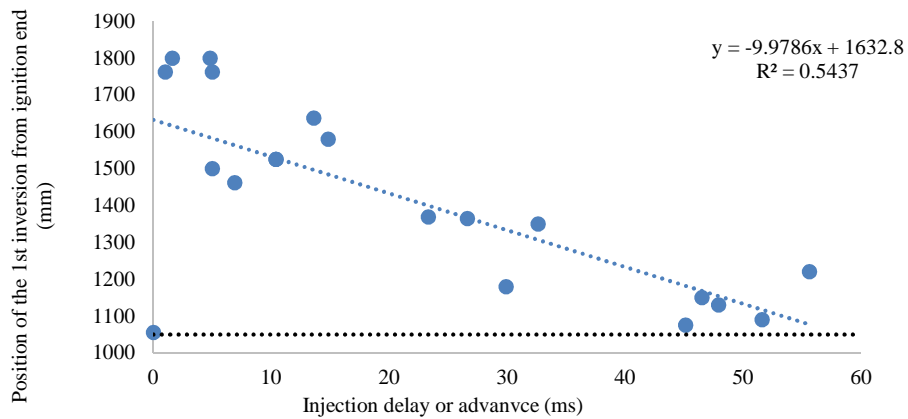
Fig. 79: Position of the first inversion for air injections below the critical mass

This value is found by dividing the duct length by the total time required to traverse the duct. It was evident that the average flame speed was significantly higher for a shorter time between air injection and ignition irrespective of being advanced or delayed. This relationship can be seen in Fig. 80 (A is used for advanced air injections and D for delayed in the Figure.) The coefficient of determination for a linear fit of the data (R^2) is 0.3434, with a negative slope of 0.1. The thick horizontal line passing through experiment number 230 shows the average flame velocity with no injection. The error of AFV is ±0.024m/s (1 in Table 11). As opposed to fuel injections the average flame speeds are significantly high when the time difference between ignition and injections were less than 5 ms. However, for air injections, the flames are faster irrespective being delayed or advanced. Experiments 219, 236, 237 and 241 show significantly fast flames which are above 30m/s. The average flame speed without injections is 26m/s. For fuel injections, average flame speeds are much lower than that for air injections.Fig. 81 shows this relationship. (R^2) is 0.06 for the fuel injections whereas it was 0.3 for air injections.

With air additions, Φ does not change very much, but for the same amount of added fuel, changes
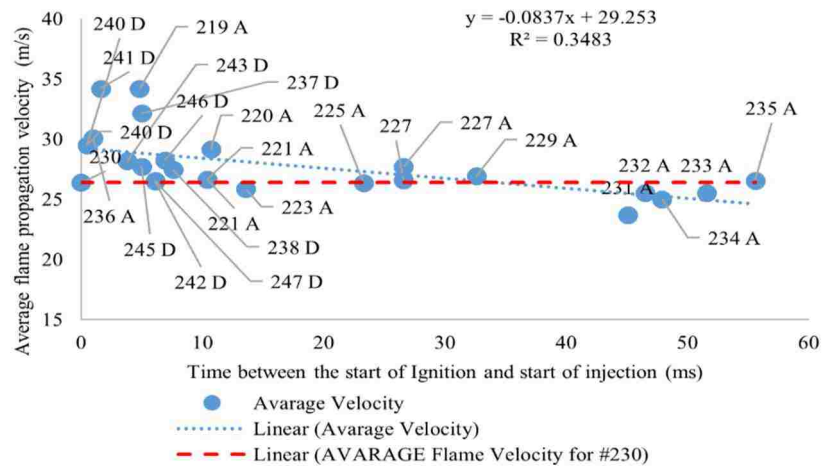
Fig. 80: The average AFV Vs delay between air injection and ignition

Φ significantly. By looking at the air and fuel injections, one can see a difference in speeds as well as how the propagation patterns change. With air injections, the local turbulence is introduced but only a small change in the composition of the mixture. However, when stratifying the mixture with fuel injections, there is a larger change in composition in addition to the local turbulence. The highest laminar flame speeds for propane occurs at an equivalence ratio of 1.1. Increasing Φ above 1.1 will reduce the laminar flame speed. One can expect slower propagating speeds for fuel injections.
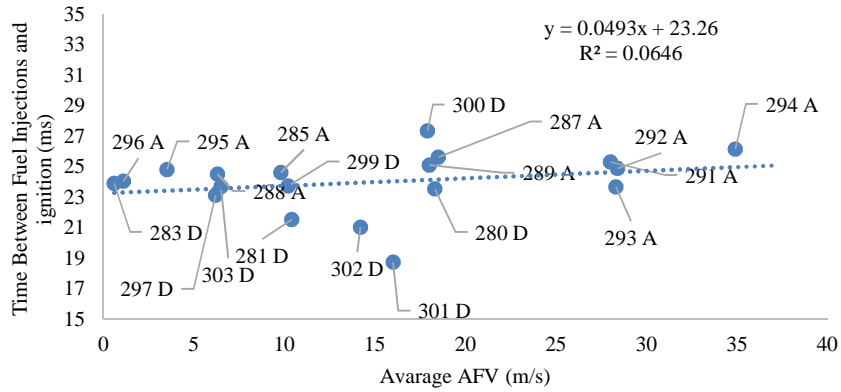
Fig. 81: Average AFV for different advanced and delayed fuels injections

5.7. MIXTURE INJECTIONS

5.7.1. Introduction

When injecting fuel or air above the critical mass, the flame propagation significantly changed. In all these injections the injector was opened when the flame was very close to the injector. The main objective of injecting a mixture is to distinguish between flow effects and mixture stratification effects.

With the experiments listed in Table 43 Appendix E - 7 an air/Propane mixture at an equivalence ratio of 1.1, is injected. This mixture is the same mixture, as the one inside the duct to form the homogeneous medium. The mixture was injected at a delay time of 17 ± 3 ms and the amount injected is varied from 54mg to 84 mg

5.7.2. Results and discussion

Similar to air injections some of the cases did not displace the tulip flame (Fig. 82) while some of the cases did displace the tulip-flame Fig. 83
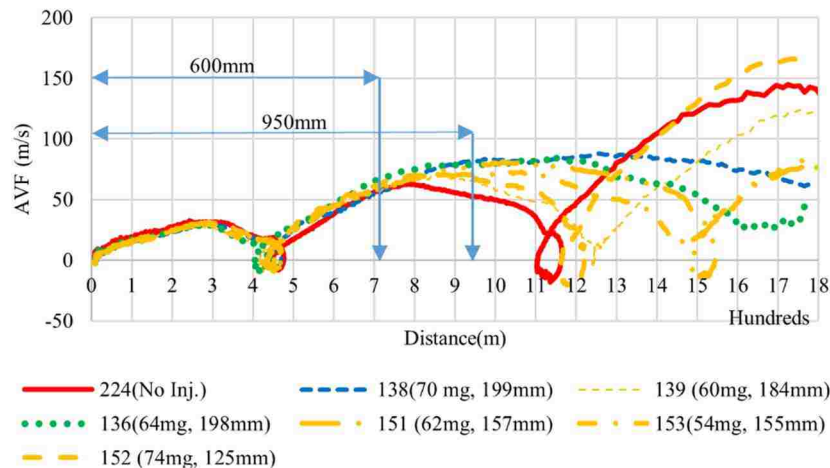
Fig. 82: Flame propagation profiles for mixture injections with no displacement of the tulip flame

The outcome of mixture injections is different from the air injections. The injected mixture mass was varied from 45 mg to 75 mg but the tulip flame displacement did not show any obvious relationship with the injected mass (Fig. 84), unlike in air injections where more than 36mg injected, displaced the tulip flame. However, when the displacement was investigated with the time it was injected, a good relationship existed. The time injected is represented by the position of the flame front at the start of injection. Fig. 85 shows this relationship. Once the mixture was injected when the flame was more than 200mm from the ignition end, the tulip flame displaced. The position of the injector is 300 mm from the ignition end. Therefore, the flame front should be within a distance of 100 mm or less when the injection starts, for the tulip-flame to be displaced. These results indicate that when the mixture is injected, the displacement of the tulip flame is caused by the local flow perturbations. However, when the air was injected, the distance of the flame front at the start of injections was the most significant factor. The difference with air injections is that the local composition contained more oxidiser in addition to the perturbations.
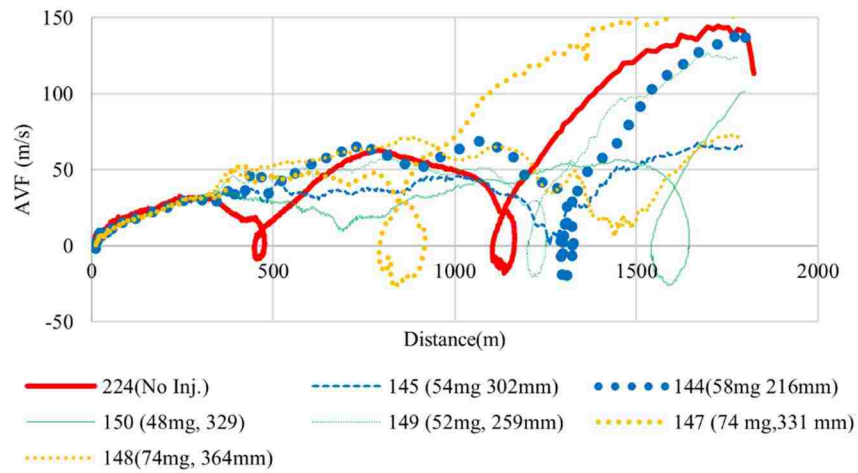
Fig. 83: Mixture injections with displacement of the tulip position
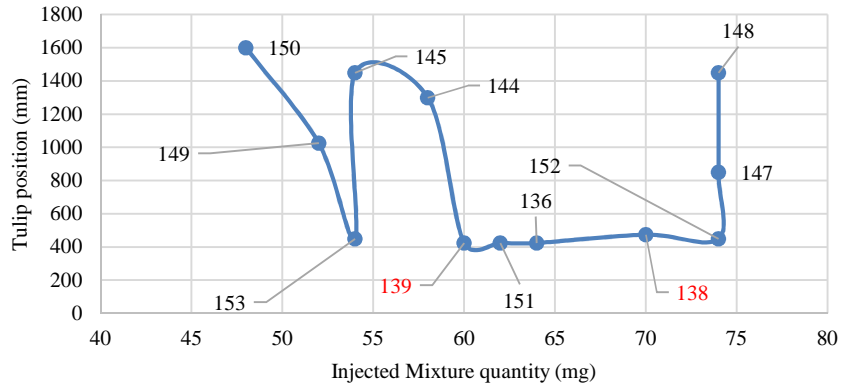
Fig. 84: Location of the tulip position Vs mass of mixture injected

95
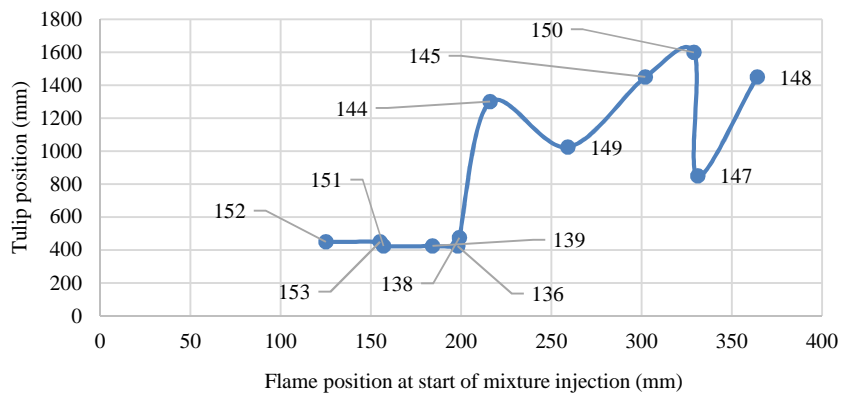
Fig. 85: Location of the tulip position Vs the position of the flame at the start of mixture injection

96

CHAPTER 6

6. SUMMARY OF RESULTS

The results demonstrate that flame propagation patterns can be significantly altered by all injections. Both the tulip flame formation and subsequent inversions can be altered or displaced. However, there are differences depending on the kind of injected gas, its mass and injection timing Fig. 86 shows the propagation patterns for injections of air fuel and mixture that severely perturbed the flame front. With air injections above the critical mass, the tulip flame has been displaced; the flame is extinguished at the first inversion. For mixture injections, no critical mass was found. However, injections that started when the flame front was within 100mm of the injector, the tulip flame position is displaced.
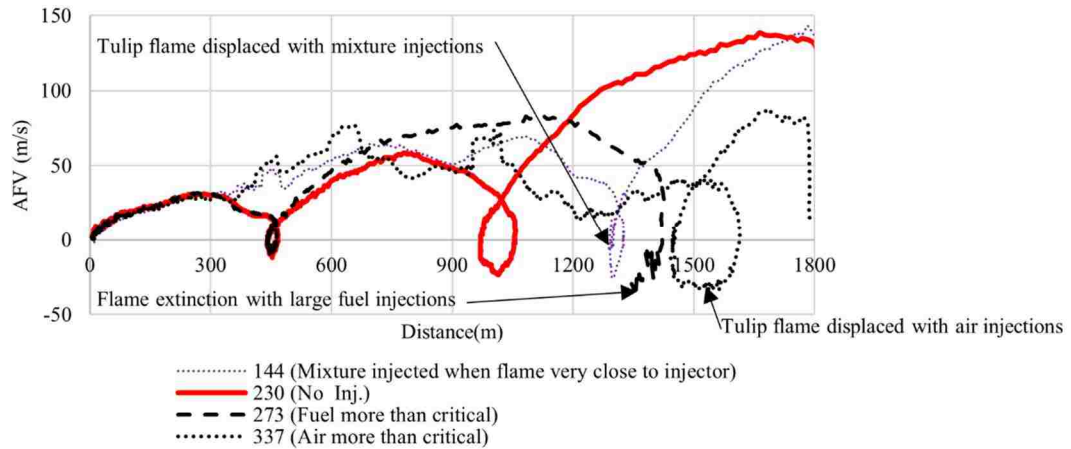
Fig. 86: Severe perturbations to the flame front by air fuel and mixture injections

Fig. 87 shows fuel injections less than the critical mass. In these trials, the first inversion was displaced. With air injections less than the critical mass, in Fig. 88 the first inversion is displaced similar to fuel injections less than the critical amount.

A closer examination of the fuel and air injections show that lines indicating the propagation patterns of fuel injections towards the end of the duct were less consistent (Fig. 87) than those of air injections (Fig. 88) The local equivalence ratio increases more for fuel additions than it is reduced with air additions. The high variation of equivalence ratios towards the end of the duct may have resulted in these inconsistencies with fuel injections.
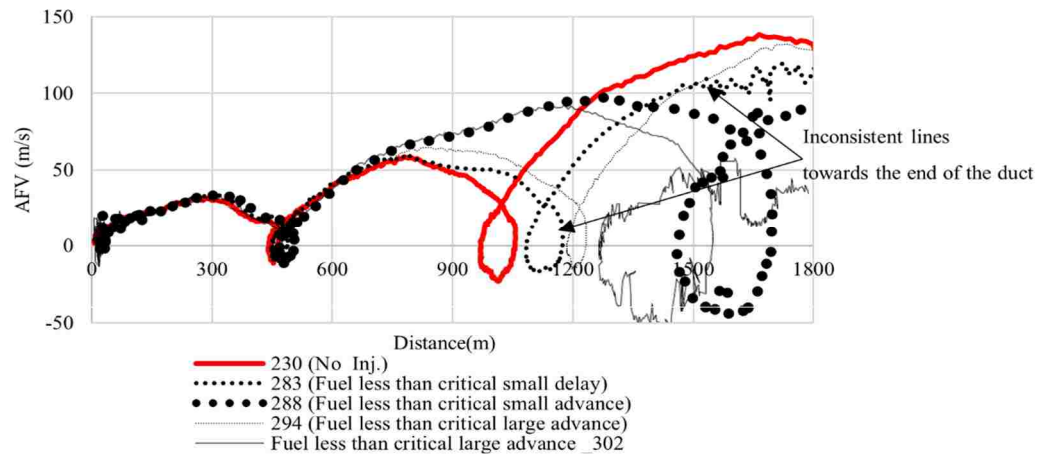
Fig. 87: Flame propagation profiles for injections with less than the critical mass of fuel injections
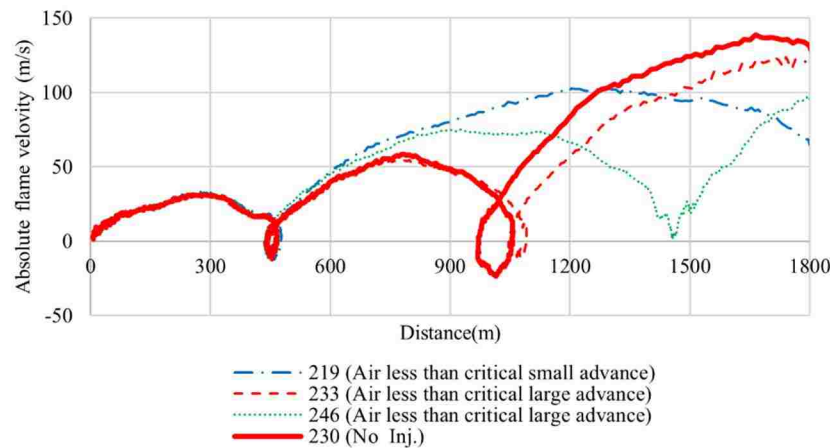
Fig. 88: Flame propagation profiles for injections with less than the critical mass of air injections

One important observation is that the flame propagation pattern reverts to its acceleration-deceleration sequencing (Leap Frog phenomenon) regardless of the severity of the level of perturbations to the flame front and the level of stratification. Flame propagations shown in cases #273 and #337 in Fig. 86 were cases where injections severely perturbed the flame front but reverted to the Leap Frog phenomenon. The very severe perturbations to the flame front similar to the above cases are shown in the image sequences in Fig. 89 for a fuel injection and Fig. 90 for an air injection.
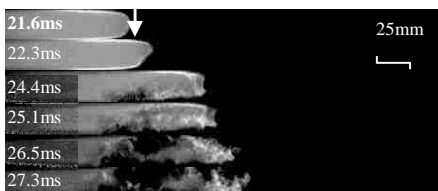
Fig. 89: Severe perturbation to the flame front by a fuel injection
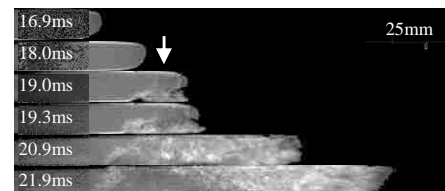
Fig. 90: Severe perturbation to the flame front by an air injection

98

In 5.1.9 the tulip formation and the subsequent inversions were analyzed. The tulip flame and the inversions occurred due to the acceleration-deceleration sequencing pattern of flame propagation. One main factor behind this pattern was identified as the R-T instability. The instability is triggered when the hot gasses start accelerating towards the cool unburnt mixture. The tulip flame and the inversions are formed with the R-T instability altering the accelerating flow, while the combustion reactions take place. At the point of formation of the tulip flame and inversions, the flame propagation comes to a halt and even propagates towards the reverse direction for a certain distance. The flame surface area increases at these points. A large volume of hot burnt gasses is generated again. This expanding hot gases creates a flow which starts accelerating again towards the cool unburnt gasses. This phenomenon repeats.

Air fuel and mixture injections with different timing as well as different masses managed to alter the position where the tulip flame or inversions occurred. However, these injections did not stop the flames from repeating Leap Frog phenomenon. The change in local equivalence ratio and the level of perturbation introduced by the gaseous injections only managed to alter the positions of the formation of the tulip flame and inversions. With very large fuel injections the flame was extinguished before the end of the duct. However, these flames also adhered to the Leap Frog and extinguished during the first inversion.

CHAPTER 7

7. UNIQUENESS OF THE STUDY, FINDINGS, CONCLUSIONS AND RECOMMENDATIONS

7.1. UNIQUENESS OF THE STUDY

The studies of flame propagation in ducts have been carried out for a long time, in fact the first such study found through the literature review was carried out in 1883. Most of these studies were concentrated on the "Leap Frog" phenomenon. Studies of flame propagation through stratified medium has been done and some of these were reported in Chapter 3. But studies on propagating flames with a stratified medium where the "Leap Frog" phenomenon is present could not be found during the literature survey. This study is unique because it analyses flame propagation with the "Leap Frog" phenomenon when the flame travels through a stratified medium.

7.2. THESIS FINDINGS

- The flame propagation in a homogeneous propane-air mixture with equivalence ratios of 0.8, 0.9, 1.0 and 1.1. show a sequence of acceleration-deceleration periods named, the "Leap-Feap" phenomenon. The first such period ends with the tulip flame formation and the subsequent periods with flame inversions. The initial acceleration period reaches a local maximum velocity, followed by a deceleration which slows down the flame until it achieves a local negative velocity. From this point, the flame starts to accelerate again reaching a new local maximum velocity, which is higher than the earlier local peak velocity in open - end cases. The peak velocity is reduced for close-end cases. This sequence repeats itself along the channel.

- In mixtures with equivalence ratios below 1.1, the tulip flame position is closer to the ignition end of the duct. In this study flames propagating in a mixture with an equivalence ratio of 1.1 had the lowest number of inversions and a mixture of equivalence ratio of 0.8 had the highest number of inversions.

- The equivalence ratio of 1.1 was chosen to be tested with air, and propane injections at 300 mm from the ignition end. These injections stratified the initial mixture. The same injection location was used to inject a portion of the initial mixture into the duct. The propane air mixture was injected to isolate the changes due to the composition variations.

- The injected air and fuel volumes are displaced downstream of the duct towards the open end induced by the propagation of the flame.

- Fuel injections enrich the initial mixture and air injections leaned-out the initial mixture. Fuel injections could increase the equivalence ratio above the upper flammability limit, but air injections do not decrease the equivalence ratio below the lower flammability limit of a propane-air mixture.

- Fuel injections of more than 34.6 mg injected when the flame was within 200 mm of the injector extinguished the flame at the first inversion. These injections started before the arrival of the flame and continued up to 10 to 40 ms after the flame passed the injection site.

- Air injections over 37 mg injected at a similar timing as in the case of fuel injections above, increase the flame speeds just after the injection site and cause the displacement of the tulip flame towards the exit end of the duct.

- A fuel mass less than 34.6 mg was injected into the duct with delayed and advanced injection timing. These injections displaced the 1st inversion.

- Fuel injection advances show a linear relationship with the position of the inversion. Small advances, less than 5 ms, displace the 1st inversions 600 mm downstream of the duct while advances above 25 ms did not displace the inversion.

- Fuel injection delays also showed a linear relationship with the position of the inversion. Delays less than 5 ms did not displace the inversion. However, delays closer to 20 ms displaced the inversion 400 mm downstream of the duct.

- For air injections less than 37 mg, unlike for fuel injections, the flame propagation responded in the same manner for advanced and delayed injections. The time between injections and ignition shows a strong linear relationship with the position of the tulip flame.

- The 1st inversion was displaced by 600 mm when the time between ignition and air injection was less than 5 ms. The 1st inversion did not change when the time between ignition and injections were larger than 40 ms.

- The AFV at 950 mm from the ignition end correlated well with the position of the 1st inversion when air and fuel were injected with different timing.

7.3. CONCLUSIONS

- The pressure variation at the closed end of the duct correlated well with the tulip flame formation as well as with the subsequent inversions. A peak pressure was observed at the time of highest negative velocity during an acceleration-deceleration period. The pressure built up gradually, up to this point, and dropped steeply right after the peak. This

101

phenomenon is repeated in every period. Since the pressure traces consisted of frequencies much below the 1st harmonic of the longitudinal oscillation frequency of the duct, it can be postulated that the acoustic pressure waves do not affect the tulip flame nor the inversions strongly.

- The flame propagation consists of a flame front which divides the higher density unburnt reactants and a lower density hot combustion products. Expanding lower density products accelerate towards the higher density fresh mixture. The conditions for the formation of the tulip-flame and the subsequent inversions are set during this acceleration period. The flame front undergoes a series of shape changes during the formation of the tulip-flame and the subsequent inversions. These shape changes are qualitatively similar to shape changes of the interface of a high-density fluid and low-density fluid when the lower density fluid is accelerated towards a higher density fluid, triggering the R-T instability. Therefore, it is postulated that the R-T instability influences the formation of the tulip flame and subsequent invasions.

- Flames terminated when fuel quantities more than 34.6 mg were injected to the propagating flame. The fuel injected behind the flame front causes the flame to extinguish at the first inversion during the reversal of the flame front. In this period the injected fuel can enrich the secondary reaction zone (section 3.4) of the flame and reduce the reaction rate in this region. The unburnt mixture penetrating the burnt region during the reverse flow at the first inversion can get mixed with the fuel from the injection and increase the equivalence ratio towards the upper flammability limit and reduce the reaction rate in the primary reaction zone as well. This reduction in reaction rates and the cooling effect from the cooler fuel can extinguish the flame counteracting effects of the extra turbulence created during the injection of fuel.

- The tulip flame was displaced towards the exit end when air quantities more than 36mg were injected to the propagating flame. The extra oxygen in the injected air is suspected to enhance the reaction rate of the secondary reaction zone in contrast to what happens with the fuel injections. This higher reaction rate increases the flame speed passing the injection site and causes the tulip-flame to be displaced further downstream of the duct. The tulip flames for equivalence ratios of 1.1 are placed further downstream of the duct than those of 0.8 or 0.9 (but not delayed in the time domain) which supports the postulate that higher reaction rates will shift the tulip-flame further downstream of the duct.

- For the propane air mixture injections, the tulip-flame is displaced downstream of the duct just as it did for air injections. However, an injected threshold mass was not determined.

Injection timing was the critical factor. Only the flames that were within 100 mm of the injection site at the start of injection displaced the tulip flame. Since the extra oxygen in the mixture was less than that in air injections, turbulence seems to be the dominating factor in increasing the reaction rate with mixtures. The closer the flame front is when the injection starts, the higher is the turbulence affecting the flame front.

- The flame propagation pattern returns to its original accelerating-decelerating sequencing pattern regardless of the severity of the perturbation to the flame front by all types of injections and the level of stratification

7.4. RECOMMENDATIONS

This study was concentrated on providing comparisons of various flame propagation patterns under many conditions. Explanations were given based on the collected data. It will be certainly helpful to gather more data to reveal more information. The following recommendations were identified for further studies.

- The velocities at the exit end of the duct, during the propagation, can reveal some interesting information. These velocities should be related to the propagating flame.

- A detailed study on the tulip flame was done for the open-end case for an equivalence ratio of 1.1 in this study; it is recommended to do the same analysis for subsequent inversions in the open- end case and for the close-end case for the tulip and inversions.

- Pressure and temperature readings at the exit end and an intermediate position along the duct is beneficial.

- The injector at 600 mm can be used to increase the range of delayed injections.

- Other means of the flow field stratification (possibly without the velocity field perturbation) should be considered.

- It is recommended to capture images from different angles and synchronize these images. These images can relate more details on the changes to the flame shapes especially at the initiation of the flame, tulip and inversion formations.

- PIV of the flow field can provide more information on the injections as well as at the tulip flame formation and inversions.

- LIF or a sampling method to determine the special variation of the mixture composition head and behind the flame front is recommended.

REFERENCES

[1] Takagi Y. A new era in spark-ignition engines featuring high-pressure direct injection. Symp. Int. Combust., vol. 27, Elsevier; 1998, 2055–68.

[2] Iwamoto Y, Noma K, Nakayama O, Yamauchi T, Ando H. Development of gasoline direct injection engine. SAE technical paper; 1997.

[3] Zheng Z, Yao M. Charge stratification to control HCCI: Experiments and CFD modeling with n-heptane as fuel. Fuel 2009;88:354–65.

[4] Lefebvre AH, Ballal DR. Gas Turbine Combustion: Alternative Fuels and Emissions, (2010). CRC Press; n.d.

[5] Gallage I, Sobiesiak A, Mohavadi Z. Flame propagation in a rectangular duct filled with stratified air and fuel mixtures. Proceedings Combust. Inst. Can. Sect., University of Saskatchewan, SK, Canada: 2015, 274–9.

[6] Salamandra GD, Bazhenova TV, Naboko IM. Formation of detonation wave during combustion of gas in combustion tube. Symp. Int. Combust., vol. 7, Elsevier; 1958, p. 851–5.

[7] Poinsot, Theory. Theoretical and Numerical Combustion 2012 NEW THIRD EDITION by Poinsot and Veynante. ELearning Cerfacs - Online Courses n.d. http://elearning.cerfacs.fr/combustion/onlinePoinsotBook/buythirdedition/index.php (accessed April 28, 2015).

[8] Veynante D, Vervisch L. Turbulent combustion modeling. Prog Energy Combust Sci 2002;28:193–266.

[9] Poinsot T, and Denis Veynante, Veynante D. Theoretical and numerical combustion. [S.l.]: T. Poinsot.; 2012.

[10] Ferziger J, Echekki T. A simplified reaction rate model and its application to the analysis of premixed flames. Combust Sci Technol 1993;89:293–315.

[11] Candel SM, Poinsot TJ. Flame stretch and the balance equation for the flame area. Combust Sci Technol 1990;70:1–15.

[12] Stone R. Introduction to internal combustion engines. vol. 2012. 1999.

[13] Ragland KW, Bryden KM. Combustion engineering. CRC Press; 2011.

[14] Kolmogorov AN. The local structure of turbulence in incompressible viscous fluid for very large Reynolds numbers. Dokl Akad Nauk SSSR, vol. 30, 1941, 299–303.

[15] Borghi R. On the structure and morphology of turbulent premixed flames. Recent Adv. Aerosp. Sci., Springer; 1985, 117–38.

[16] Peters N. Laminar flamelet concepts in turbulent flames. Comptes-Rendus 21st SympInt Comb Combust. Inst., 1986.

[17] Borghi R, Destriau M. Combustion et les flamme... Editions OPHRYS; 1998.

[18] Drazin PG. Introduction to Hydrodynamic Stability, chap. 8. Cambridge University Press; 2002.

[19] Clanet C, Searby G. First experimental study of the Darius-Landau instability. Phys Rev Lett 1998;80:3867.

[20] Matalon M. Intrinsic flame instabilities in premixed and nonpremixed combustion. Annu Rev Fluid Mech 2007;39:163–91.

[21] Sharp DH. An overview of Rayleigh-Taylor instability. Phys Nonlinear Phenom 1984;12:3–18.

[22] Rayleigh. Investigation of the Character of the Equilibrium of an Incompressible Heavy Fluid of Variable Density. Proc Lond Math Soc 1882;s1-14:170–7. doi:10.1112/plms/s1-14.1.170.

[23] Taylor G. The Instability of Liquid Surfaces when Accelerated in a Direction Perpendicular to their Planes. I. Proc R Soc Lond Math Phys Eng Sci 1950;201:192–6. doi:10.1098/rspa.1950.0052.

[24] Li S, Li H. Parallel AMR Code for Compressible MHD or HD Equations. Los Alamos Natl Lab Retrieved 2006:09–05.

[25] Kull H-J. Theory of the Rayleigh-Taylor instability. Phys Rep 1991;206:197–325.

[26] Glimm J, Grove JW, Li XL, Oh W, Sharp DH. A Critical Analysis of Rayleigh–Taylor Growth Rates. J Comput Phys 2001;169:652–77. doi:10.1006/jcph.2000.6590.

[27] Richtmyer RD. Taylor instability in shock acceleration of compressible fluids. Commun Pure Appl Math 1960;13:297–319.

[28] Meshkov EE. Instability of the interface of two gases accelerated by a shock wave. Fluid Dyn 1969;4:101–4.

[29] Rightley PM, Vorobieff P, Benjamin RF. Mushrooms and Snakes: A Visualization of Richtmyer—Meshkov Instability. Phys Fluids 1994-Present 1997;9:S6–S6.

[30] Kader AA. Methods of gas mixing, sampling and analysis. Postharvest Technol Hortic Crops Publ 2002;3311:145–8.

[31] Mallard E, Le Chatelier H. Combustion of explosive gas mixtures. AnnMine 1883:379–568.

[32] Mason W, Wheeler RV. XCII.—The "uniform movement" during the propagation of flame. J Chem Soc Trans 1917;111:1044–57.

[33] Mason W, Wheeler RV. V.—The propagation of flame in mixtures of methane and air. Part I. Horizontal propagation. J Chem Soc Trans 1920;117:36–47. doi:10.1039/CT9201700036.

[34] De Champfleur Ellis OC, Robinson H. CVII.—A new method of flame analysis. J Chem Soc Trans 1925;127:760–4. doi:10.1039/CT9252700760.

[35] Ellis O. Flame movement in gaseous explosive mixtures - some general Ideas. Fuel 1928;7:195–205.

[36] Ellis O. The propagation of flame from central ignition in tubes. Fuel 1928;7:408–15.

[37] Ellis O. Flame Movement in Gaseous explosive mixtures - VIII Propagation of a flame through a tube from ignition at one end. Fuel 1928;7:502–8.

[38] Bone WA, Fraser RP. Photographic Investigation of Flame Movements in Gaseous Explosions. Parts IV, V, and VI. Philos Trans R Soc Lond Math Phys Eng Sci 1932;230:363–85. doi:10.1098/rsta.1932.0010.

[39] Markstein GH. A Shock-tube study of flame front-pressure wave interaction. Symp. Int. Combust., vol. 6, Elsevier; 1957, p. 387–98.

[40] Dunn- Rankin DD-R, R F Sawyer, Swayer RF. Tulip flames: changes in shape of premixed flames propagating in closed tubes. Exp Fluids 1998;24:130–40. doi:10.1007/s003480050160.

[41] Dunn-Rankin D, Barr P, Sawyer R. Numerical and experimental study of "tulip" flame formation in a closed vessel. vol. 21, Elsevier; 1988, p. 1291–301.

[42] Gonzalez M. Interaction of a flame front with its self-generated flow in an enclosure: The "tulip flame" phenomenon. Combust Flame 1992;88:201–20. doi:10.1016/0010-2180(92)90052-Q.

[43] Clanet C, Searby G. On the "tulip flame" phenomenon. Combust Flame 1996;105:225–38.

[44] Gordon M. McAlary. Flame behaviour in a straight duct with a 90° curved section. M.Sc Thesis. Queens University, 1999.

[45] Battoei M, Barbour E, Mackellar S, Sobiesiak A, Ting D. Flame Inversions in a Rectanbular Duct With 90 degree Bend. Combust. Inst. Can. Sect., Windsor, Canada: 2002.

[46] Valiev DM, Kuznetsov M, Eriksson L-E, Law CK, Bychkov V. Influence of gas compression on flame acceleration in the early stage of burning in tubes. Combust Flame 2013;160:97–111.

[47] Bychkov V, Fru G, Petchenko A, Eriksson L-E. Flame acceleration in the early stages of burning in tubes. Combust Flame 2007;150:263–76.

[48] Sobiesiak A, Battoei, M., Barbour E, Mackellar S, Ting, D. Flame Inversions in a Rectangular Duct with 90°Bend. Int. Colloq. Dyn. Explos. React. Syst., University of Mining & Metallurgy, KraKow, Poland: 2003.

[49] Zhou B, Sobiesiak A, Quan P. Flame behavior and flame-induced flow in a closed rectangular duct with a 90° bend. Int J Therm Sci 2006;45:457–74. doi:10.1016/j.ijthermalsci.2005.07.001.

[50] Xiao H, Makarov D, Sun J, Molkov V. Experimental and numerical investigation of premixed flame propagation with distorted tulip shape in a closed duct. Combust Flame 2012;159:1523–38. doi:10.1016/j.combustflame.2011.12.003.

[51] Xiao H, Sun J, Chen P. Experimental and numerical study of premixed hydrogen/air flame propagating in a combustion chamber. J Hazard Mater 2014;268:132–9. doi:10.1016/j.jhazmat.2013.12.060.

[52] Xiao H, Houim RW, Oran ES. Formation and evolution of distorted tulip flames. Combust Flame 2015;162:4084–101. doi:10.1016/j.combustflame.2015.08.020.

[53] Da Cruz AP, Dean AM, Grenda JM. A numerical study of the laminar flame speed of stratified methane/air flames. Proc Combust Inst 2000;28:1925–32.

[54] Pasquier N, Lecordier B, Trinité M, Cessou A. An experimental investigation of flame propagation through a turbulent stratified mixture. Proc Combust Inst 2007;31:1567–74. doi:10.1016/j.proci.2006.07.118.

[55] Haworth D, Blint R, Cuenot B, Poinsot T. Numerical simulation of turbulent propane–air combustion with nonhomogeneous reactants. Combust Flame 2000;121:395–417.

[56] McKellar SW. Combustion of Propane-air Mixtures with Oxygenated Additives in a Closed Duct and an SI Engine. 2004.

[57] Alicat Scientific. Calibration Data Sheet. Tcson, USA: Alicat Scientific Inc.; 2007.

[58] Kistler Instrument Corporation. Kistler Operating Instructions Manual, Dual Amplifier Type 5004. 75 John Glen Drive, NY, USA.: Kistler Instrument Corporation; n.d.

[59] Kistler Group. Kistler, Engine Combustion Analysis, Engine Pressure Measurement for Research and development. Switzerland Eulachstrasse 22, 8408 Winterthur: Kistler Group; 2010.

[60] Alicat Scientific Inc. Operating Manual, 16 Series Mass and Volumetric Precision Gas Flow Meter. Tucson,USA: Alicat Scientific Inc.; n.d.

[61] Davidson TA. A simple and accurate method for calculating viscosity of gaseous mixtures 1993.

[62] Kristoffersen K. Gas explosions in process pipes. 2004.

[63] De Champfleur Ellis OC. CLXVIII.—The propagation of flame from a spark in a closed tube through a homogeneous inflammable mixture. J Chem Soc Trans 1923;123:1435–52. doi:10.1039/CT9232301435.

[64] Mason W, Wheeler RV. XCII.-The "uniform movement" during the propagation of flame. J Chem Soc Trans 1917;111:1044–57. doi:10.1039/CT9171101044.

[65] Turns SR. An introduction to combustion. vol. 287. McGraw-hill New York; 2012.

[66] Westbrook CK, Mizobuchi Y, Poinsot TJ, Smith PJ, Warnatz J. Computational combustion. Proc Combust Inst 2005;30:125–57.

[67] Richard S Figliola and Donald E Beasley. Theory and Design for Mechanical Measurements, Third Edition. Meas Sci Technol 2001;12:161–98.

[68] Moffat RJ. Describing the uncertainties in experimental results. Exp Therm Fluid Sci 1988;1:3–17.

[69] Ashcroft Inc.,. Pressure gauge installation, operation and maintenance. Stratford, CT 06614-5145 U.S.A: n.d.

[70] National Instruments Corporation. NI 6034E/6035E/6036E Family Specifications© 2003–2005 National Instruments Corporation. All rights reserved. -01. National Instruments Corporation; Dec 05.

APPENDICES

APPENDIX - A   COPYRIGHT PERMISSION FOR FIGURES FROM OUTSIDE SOURCES USED IN THE THESIS

A - 1   Fig. 3: Structure of laminar plane premixed flames; modified image published in [7] License Number 3846560719624.

A - 2   Fig. 6: Turbulent premixed combustion regimes modified diagram using modified image published in [8]

License Number 3846560719624.

A - 3   Fig. 7: Turbulent combustion regimes as a function of non-dimensional numbers; image published in [9]

Permission granted by the author and publisher Dr. Thierry Poinsot via e-mail on 17/05/2016.

A - 4   Fig. 8: Using the regime diagram to interpret operating ranges of devices; modified image published in [9] –

Permission granted by the author-publisher Dr. Thierry Poinsot via e-mail. 17/05/2016

A - 5   Fig. 9: Deviation of flow lines leading to Darius-Landau instability; image published in [19]

License Number 3846621281983.

A - 6   Fig. 10: Simulated results of the Rayleigh–Taylor instability; image published in [24]

This image is a work of a United States Department of Energy (or predecessor organization) employee, taken or made as part of that person's official duties. As work of the U.S. federal government, the image is in the public domain.

"Unless otherwise indicated, this information has been authored by an employee or employees of the University of California, operator of the Los Alamos National Laboratory under Contract No. W-7405-ENG-36 with the U.S. Department of Energy. The U.S. Government has rights to use, reproduce, and distribute this information. The public may copy and use this information without charge, provided that this Notice and any statement of authorship are reproduced on all copies. Neither the Government nor the University makes any warranty, express or implied, or assumes any liability or responsibility for the use of this information*".*

A - 7   Fig. 12: Coexistence of all morphologies- Richtmyer-Meshkov Instability: image published in [29].

A - 8   ***Fig. 13: High speed images of a propagating wave in a closed duct by Ellis in 1928: image published in [37]***

Permission granted from Elsevier by email of Mon, Oct 24, 2016

A - 9   ***Fig. 14: Initial stages of the shock wave flame and front interaction with three images showing the stages of the development of the tulip flame: image published in [39]***

License Number 3852561167649

A - 10   ***Fig. 15: The tulip shaped flame captured by Salamandra et al.: Image published in [6]***

License Number 3846650719713

A - 11   ***Fig. 16: Simplified geometric model of flame front at times between t $_{Sphere}$ and t $_{Wall}$: image published in [43]***

License Number 3852571329231

A - 12   ***Fig. 17: Normalized superposition plot of pressure at closed end, the position of center of flame tip and of tailing edge of flame skirt; as a function of time. The best fit exponential is also shown: image published in [43]***

License Number 3852571329231

APPENDIX - B   GOVERNING EQUATIONS AND NUMERICAL STUDY FOR REACTING FLOWS

To study a reacting flow field, it is required to know

- Transport properties of each particle which are the velocities in x, y and z directions
- The density.
- One more property which could be Pressure, Enthalpy, Energy or Temperature.
- Finally, the composition or mass fraction of each species should be known.

If we have N number of species, (5+N) variables needs to be revealed to define the reacting flow field, thus we need 5+N equations.

Table 29 below shows a summary of the number of equations needed to solve a reacting flow problem.

Table 29: Total number of equations to solve a reacting flow problem

Equation Number	Title	Number of equations
1	Continuity	1
2	Momentum	3
3	Total Energy	
4	Energy	
5	Enthalpy	1
6	Sensible Enthalpy	
7	Temperature	
8	Species	N
Total Number of Equations		N+5

B - 1   Equations for a reacting flow shown in Table 29

One continuity equation

$$\frac{\partial \rho}{\partial t} + \nabla(\rho u) = 0$$

(70)

$\rho = Density(m^3)$

$t = time(s)$

$u = Velocity(ms^{-1})$

3 momentum equations in the 3 directions i & j=1,2,3

$$\rho \frac{Du_i}{Dt} = \frac{\partial}{\partial x_j}\sigma_{ij}$$

$$\frac{D(\rho u_i)}{Dt} = \frac{\partial(\rho u_i)}{\partial t} + \frac{\partial(\rho u_i)u_j}{\partial x_j}$$

$u_i = Velocity\ in\ the\ direction\ i$

$\sigma_{ij}(Total\ Stress\ Tensor) = \tau_{ij} - P\delta_{ij} \quad , \delta_{ij}\begin{cases} = 1\ if\ i = j \\ = 0\ if\ i \neq j \end{cases}$

$\tau_{ij}(Viscouse\ Tensor) = -\frac{2}{3}\eta\frac{\partial u_i}{\partial x_i} + \eta\left(\frac{\partial u_i}{\partial x_j} + \frac{\partial u_j}{\partial x_i}\right)$

$\eta = Absolute\ or\ dynamic\ viscousity$

1 of the following equations

Total Energy (e_t)

$$\rho \frac{De_t}{Dt} = -\frac{\partial}{\partial x_j}q_i + \frac{\partial}{\partial x_j}\sigma_{ij}u_i$$

(72)

$q_i = \lambda\frac{\partial T}{\partial x_i} + \rho\sum_{K=1}^{N} y_k h_k V_{k_i} = Heat\ Flux\ (^W/_{m^2})$

$\lambda = Thermal\ conductivity\ \left(^W/_{m.K}\right)$

$V_{k_i} = \textbf{Diffusion Velocity of}\ k_i(^m/_s)$

$y_k = Mass\ fraction\ of\ k$

$h_k = Enthalpy\ of\ k\ (J/kg)$

Energy(e)

(73)

$$\rho \frac{De}{Dt} = -\frac{\partial}{\partial x_i}q_i + \sigma_{ij}\frac{\partial}{\partial x_j}u_i$$

Enthalpy(h)

$$\rho \frac{Dh}{Dt} = \frac{DP}{Dt} - \frac{\partial}{\partial x_j} q_i + \tau_{ij} \frac{\partial}{\partial x_j} u_i$$

(74)

Sensible Enthalpy(h_s)

$$\rho \frac{Dh_s}{Dt} = \frac{\partial}{\partial x_j} q_i \left(\lambda \frac{\partial T}{\partial x_j} \right) - \frac{\partial}{\partial x_j} \left(\rho \Sigma h_{s_k} y_k V_{ki} \right) + \tau_{ij} \frac{\partial}{\partial x_j} u_i + \frac{DP}{Dt} + \dot{\omega}_T$$

(75)

$$\dot{\omega}_T (Heat\ Release) = -\sum \Delta H^0_{f_k} \dot{\omega} k$$

$\Delta H^0_{f_k} = Chemical\ Enthalpy$

$\dot{\omega} k = mass\ reaction\ rate\ (consumption!) of\ species\ k$

Temperature (T)

$$\rho C_p \frac{DT}{Dt} = \frac{\partial}{\partial x_j} q_i \left(\lambda \frac{\partial T}{\partial x_j} \right) + \frac{DP}{Dt} + \tau_{ij} \frac{\partial}{\partial x_j} u_i - \frac{\partial T}{\partial x_j} \rho \left(\Sigma C_{p_k} y_k V_{k_i} \right) + \dot{\omega}_T{}'$$

(76)

$$\dot{\omega}_T{}' (Heat\ Release) = -\sum \left(\Delta H^0_{f_k} + hs_k \right) \dot{\omega} k$$

$hs_k = Sensible\ enthalpy$

N number of species equations (78) which are for k=1 to N we have the N+5 equations needed to define the flow

In deriving this equation, the extension of the Fick's law is used.

Fick's Law -The relationship of diffusion velocities when species 1 and 2 are present, is related as $V_1Y_1 = -D_{12}\nabla Y_1$. V denotes velocities, Y- Mass Fractions, D_{12} binary diffusion coefficient of species 1 and 2. The extension of the Fick's law uses the value D_k which is the diffusion coefficient k into the rest of the mixture and not into one of the other species; most commercial codes use this D_k value which comes from the extension of Fick's law which is $V_kY_k = -D_k\nabla Y_k$,

$$Le = \frac{D_{th}}{D_k}$$

The Lewis number is the ratio of the thermal diffusion coefficient to the mass diffusion coefficient, in most cases where the Lewis number is one we can use the thermal diffusion coefficient in place of D_k

$$\rho \frac{Dy_k}{Dt} = \nabla(\rho D_k \nabla y_k) + \dot{\omega}k$$

The number of species or N could be in the range of 3000. In simulations, a grid is created, and calculations are carried out on each node of the grid at a selected time interval. In a reacting flow the grid should be able to define at least the flame thickness hence the flame thickness controls the required mesh resolution. In turbulent reacting flows, the flame thickness could be in the range of 30 µm where you should be having time steps for calculations in the range of milliseconds. To resolve this problem using DNS with detailed chemistry it is needed to calculating 3005 equations in all the grid points (approximately 35 million for a 1cm³for a 30 µm 3D grid). If a time step of a 0.1 millisecond is used a massive computing power (100 trillion calculations per millisecond or 1 petaFLOPS) is required to resolve the flow fully. This order of computing is referred to, as PetaFLOP operations. FLOPS is the number of floating point operations per second[66].

APPENDIX - C   UNCERTAINTY ANALYSIS

Uncertainty analysis is the method of systematically quantifying the probable error. Knowing the uncertainties of the values measured helps to understand the results you receive in an experiment. It is also a powerful tool to locate the source of troubles in an experiment [31]. The analysis is done based on methods stated in "Theory and Design for Mechanical Measurements, Third Edition" by Richard S. Figliola and Donald E Beasley [67]

C - 1   *Bias Error (B)*

Bias errors are offset errors. This error remains constant during a given series of measurements. Normally these errors are provided by the equipment manufacturer.

C - 2   *Precision Errors (P)*

These errors are caused by random fluctuations. The Random error for a sample mean $S\bar{x}$ is given

$$Presision \ of \ measurd \ value \ of \ x = u1 = t_{n,p} * S_x \tag{79}$$

$$Presision \ of \ sample \ mean \ of \ x \ of \ x = u2 = t_{n,p} * S_{\bar{x}} \tag{80}$$

$$s_x = \sqrt{\sum_{i=1}^{n} \frac{(x_i - \bar{x})^2}{(n-1)}} \tag{81}$$

$$S_{\bar{x}} = \frac{s_x}{\sqrt{n}} \tag{82}$$

n-degree of freedom in the t distribution

P-Probability normally 95%.

$t_{n,p}$- t value of the Student's distribution for a P% P probability and n degrees of freedom

C - 3   *The uncertainty of a result R*

Where $R=f(x_1+x_2+\ldots\ldots+x_L)$, the uncertainty of R is given by the Kline and Mclintock[68] equation.

115

$$U_R = \pm \sqrt{\left[\left(\frac{\partial R}{\partial x_1}\right)_{\bar{x}_i} u_{x_1}\right]^2 + \left[\left(\frac{\partial R}{\partial x_1}\right)_{\bar{x}_i} u_{x_2}\right]^2 + \cdots + \left[\left(\frac{\partial R}{\partial x_i}\right)_{\bar{x}_i} u_{x_i}\right]^2} \tag{83}$$

C - 4   ***Different Measurement Stages***

The Design Stage Uncertainty.

The instrument manufacturer provides this information.

- Zero order uncertainty
- Instrument errors.

$$U_0 = \pm \frac{1}{2} * (Instrument\ resolution) \tag{84}$$

$$U_C = \pm \sqrt{\sum_{i=1}^{N} e_i^2} \tag{85}$$

e_i- errors listed by the manufacturer of the instrument.

- Design stage uncertainty.

$$U_d = \pm \sqrt{u_o^2 + u_c^2} \tag{86}$$

Single Measurement Uncertainty

This is given by combining the design stage uncertainties with the first and second order uncertainties in (79),(80).

$$U_N = \sqrt{B^2 + \sum_{i=0}^{N} u_i^2} \tag{87}$$

116

Multiple Measurement Uncertainty

The source groups of errors come from.

Table 30: Source groups of error represented by the i value

I	Source group
1	Calibration
2	Data Acquisition
3	Data Reduction.

The source precision index P is given by

$$P_i = \sqrt{p_{i1}^2 + p_{i2}^2 + \cdots + p_{ik}^2} \qquad (88)$$

For i=1,2 and 3

$$P = \sqrt{p_1^2 + p_2^2 + p_3^2} \qquad (89)$$

The source Bias limit B is given by

$$B_i = \sqrt{B_{i1}^2 + B_{i2}^2 + \cdots + B_{ik}^2} \qquad (90)$$

$$B = \sqrt{B_1^2 + B_2^2 + B_3^2} \qquad (91)$$

Uncertainty is U_x is given by

$$U_x = \sqrt{B^2 + t_{n,p} * P} \qquad (92)$$

117

APPENDIX - D   DESIGN STAGE UNCERTAINTIES OF EQUIPMENT USED

D - 1   *Design stage Uncertainty of Ashcroft type 1082 combination vacuum and pressure test gauge*

Table 31: Design errors of Ashcroft type 108 pressure gauge [69]

Notation of Uncertainty	Uncertainty Type	Description of Uncertainty provided by manufacturer[69]	Value	Unit
U_{0ASH}	Zero Order Uncertainty	±0.25 Psi	±0.25	Psi
e_{1ASH}	Instrument error due to every 40oF over 75	±0.5% of full scale. @ operating temperature of the apparatus, this error is zero	0	Psi
U_{DASH}	Design Stage	Calculated using equation (86)	±0.25 Psi	Psi

$$=$$

D - 2   *Design stage Uncertainty of Alicat scientific flow meter*

Table 32: Design errors of Alicat scientific flow meter [57]

Notation of Uncertainty	Uncertainty Type	Description of Uncertainty provided by manufacturer[40]	Value	Units
e_1	Calibration Uncertainty	±(0.8% of Reading+0.2% of full scale)		
e_2	Full-Scale Pressure Accuracy		±0.8	Psi
e_3	Temparature Accuracy	±1.5 C0	±1.5	C^0
U_{0P}	Zero Order Pressure	50% Resolution	±0.005	Psi
U_{0T}	Zero Order Temparature	50% Resolution	±0.005	C^0
U_{DT}	Design Stage Temperature		±1.500	C^0
U_{DP}	Design Stage Pressure		±0.411	Psi

D - 3   *Design stage Uncertainty of NI 6036 DAQ card for 5V range*

Table 33: Design errors of NI 6036 DAQ card for 5V range [70]

Notation of Uncertainty	Uncertainty Type	Description of Uncertainty provided by manufacturer[70]	Value	Units
e_{15V}	Absolute uncertainty for Positive 5 volts full scale	±2.337 mv	±2.337	mV
U_{05V}	Zero Order for a 16bit resolution for a 5V range	±0.0762939453125	±0.076	mV
U_{D5V}	Design Stage	Calculated using equation (86)	±2.338	mV

D - 4   Design stage Uncertainty of NI 6036 DAQ card for 10V range

Table 34: Design errors of NI 6036 DAQ card for 10V range[70]

Notation of Uncertainty	Uncertainty Type	Description of Uncertainty provided by manufacturer[70]	Value	Units
e_{110V}	Absolute uncertainty for Positive 10 volts full scale	±8.653 mv	±8.65	mV
U_{010v}	Zero Order for a 16bit resolution for a 5V range	50% of resolution	±0.15	mV
U_{D10V}	Design	Calculated using equation (86)	±8.65	mV

D - 5   Design stage Uncertainty of Kistler 6117BF Pressure transducer

Table 35: Design errors of Kistler 6117BF pressure transducer[59]

Notation of Uncertainty	Uncertainty Type	Description of Uncertainty provided by manufacturer[59]	Value	Units
e_{1PT}	Linearity	±0.5 % of Full Scale Output 200bar		

D - 6   Design stage Uncertainty of Kistler Dual Mode Amplifier type 5004

Table 36: Design stage uncertainty of Kistler Dual Mode Amplifier type 5004[58]

Notation of Uncertainty	Uncertainty Type	Description of Uncertainty provided by manufacturer[58]	Value	Units
e1	Linearity of transducer sensitivity Potentiometer	±0.5% of Full Scale (10V)	±50	mV
U_{DAmp}	Design	Calculated using equation (86)	±50	mv

APPENDIX - E   LISTS OF EXPERIMENTS AND SUMMARIES OF EXPERIMENTAL RESULTS

E - 1   List of experiments and results for all experiments without injections

Table 37: List of experiments with average correlation coefficient of the same group, *

indicates the experiment that best represent the group of experiments

Exp. #	Φ	Exit End Open/Closed	Average Correlation	Exp. #	Φ	Exit End Open/Closed	Average Correlation
15	0.8	O	0.981	47	1.0	O	0.981
16	0.8	O	0.98	51	1.0	O	0.983
17	0.8	O	0.983	48	1.0	O	0.984
18	0.8	O	0.979	43	1.0	O	0.985
24*	**0.8**	**O**	**0.983**	52	1.0	O	0.987
25	0.8	O	0.979	**50***	**1.0**	**O**	**0.990**
12	0.8	C	0.999	27	1	C	0.999
13	0.8	C	0.999	56	1	C	0.999
14	0.8	C	0.999	**60***	**1**	**C**	**0.999**
21	0.8	C	0.999	34	1.1	O	0.9885
22	0.8	C	0.999	36	1.1	O	0.9896
23*	**0.8**	**C**	**0.999**	35	1.1	O	0.9940
1	0.9	O	0.999	39	1.1	O	0.9951
2	0.9	O	0.999	42	1.1	O	0.9957
3*	**0.9**	**O**	**0.999**	**40***	**1.1**	**O**	**0.9959**
4	0.9	C	0.996	32	1.1	C	0.996
5*	**0.9**	**C**	**0.998**	**33***	**1.1**	**C**	**0.996**
6	0.9	C	0.998	37	1.1	C	0.995

Table 38: Experiments to determine the "Critical Fuel Mass" to be injected

Index	Exp. #	Flame Code (refer Table 24: Description of the flame code, to understand code)	Injected total fuel mass m_f (mg)
1	260	O_1.1_F_47mg _12.4ms_41.58Psi_132mm_260	47
2	261	O_1.1_F_44mg _10.2ms_41.06Psi_121mm_261	44
3	262	O_1.1_F_39mg _15.5ms_41.14Psi_285mm_262	39
4	263	O_1.1_F_37mg _13.8ms_41.21Psi_237mm_263	37
5	264	O_1.1_F_30mg _13.6ms_41.24Psi_172mm_264	30
6	265	O_1.1_F_32mg _12.2ms_41.24Psi_176mm_265	32
7	266	O_1.1_N_266	-
8	268	O_1.1_F_32mg _15.2ms_40.9Psi_256mm_268	32
9	269	O_1.1_F_35mg _12.9ms_40.9Psi_181mm_269	35
10	270	O_1.1_F_37mg _16.4ms_40.9Psi_244mm_270	37
11	273	O_1.1_F_35mg _16.9ms_40.64Psi_245mm_273	35
12	274	O_1.1_F_40mg _15.7ms_40.64Psi_275mm_274	40
13	275	O_1.1_F_40mg _17.6ms_40.64Psi_265mm_275	40

E - 3   *Summary of results for injecting different amounts of fuel*

Table 39: Summary of results for injecting different amounts of fuel when the flame is 120mm-300mm from flame

Exp. #	Max Injection mass flow rate(SMLPS)	Injection Mass at start of injection (mg)	Total time of flame travel (ms)	Total distance traveled by Flame (mm)	Average flame velocity (m/s)	Total injection mass (mg)	Ignition delay (mm)	Flame position at start of injection (mm)
261	1,923.99	0.61	50.00	1,028.9	21.05	47.26	12.40	132.00
262	1,917.92	0.60	54.30	1,052.9	21.51	44.34	10.20	121.00
263	1,931.49	0.60	55.20	1,063.7	21.86	38.80	15.50	285.00
264	1,761.44	0.61	83.50	1,457.3	19.30	37.34	13.80	237.00
265	1,515.67	0.61	108.50	1,821.3	17.55	30.47	13.60	172.00
266	1,488.98	0.61	106.00	1,823.0	17.35	31.52	12.20	176.00
268	1,562.63	0.60	78	1,820.4	24.38	28.58	12.8	149.00
269	1,663.00	0.60	77.50	1,815.0	25.74	31.64	15.20	256.00
270	1,759.94	0.60	76.00	1,820.1	25.55	34.61	12.90	181.00
271	1,801.76	0.60	76.00	1,337.3	18.96	37.19	16.40	244.00
272	1,861.18	1.14	75.20	1,820.1	25.26	36.76	18.30	334.00
273	1,727.91	0.56	86.00	1,822.3	21.12	35.39	20.00	358.00
274	1,699.53	0.56	63.20	1,346.1	22.85	34.78	16.60	235.00
275	1,750.65	0.23	60.60	1,222.3	22.17	40.31	15.70	275.00
276	1,699.20	0.56	61.50	1,457.3	25.58	40.09	17.60	269.00

Table 40: List of experiments to verify influence of the delay between fuel injections and ignition

Index	Exp.#	Flame Code (refer Table 24: Description of the flame code, to understand code)	Time between ignition and injection	Ignition Delay(D) or Advance (A)
1	280	O_1.1_F_24mg _18.3ms_40.61Psi_308mm_280	18.3ms	A
2	281	O_1.1_F_27mg _10.4ms_40.64Psi_94mm_281	10.4ms	A
3	283	O_1.1_F_29mg _0.6ms_40.66Psi_6mm_283	0.6ms	A
4	284	O_1.1_F_39mg _2.5ms/1.43mg_40.66Psi_284	2.5ms	D
5	285	O_1.1_F_26mg _9.8ms/8.79mg_40.53Psi_285	9.8ms	D
6	286	O_1.1_F_30mg _12.6ms/13.6mg_40.67Psi_286	12.6ms	D
7	287	O_1.1_F_25mg _18.5ms/17.33mg_40.67Psi_287	18.5ms	D
8	288	O_1.1_F_30mg _6.3ms/4.89mg_40.67Psi_288	6.3ms	D
9	289	O_1.1_F_30mg _18ms/19.9mg_40.64Psi_289	18ms	D
10	291	O_1.1_F_30mg _28ms/20.84mg_40.64Psi_291	28ms	D
11	292	O_1.1_F_30mg _28.4ms/20.7mg_40.66Psi_292	28.4ms	D
12	293	O_1.1_F_29mg _28.3ms/20.71mg_40.66Psi_293	28.3ms	D
13	294	O_1.1_F_29mg _34.9ms/20.39mg_40.66Psi_294	34.9ms	D
14	295	O_1.1_F_22mg _3.5ms_37.07Psi_19mm_295	3.5ms	A
15	296	O_1.1_F_29mg _1.1ms/0.06mg_40.68Psi_296	1.1ms	D
16	297	O_1.1_F_28mg _6.2ms_40.68Psi_39mm_297	6.2ms	A
17	299	O_1.1_F_23mg _10.2ms_40.68Psi_93mm_299	10.2ms	A
18	300	O_1.1_F_22mg _17.9ms_40.65Psi_329mm_300	17.9ms	A
19	301	O_1.1_F_27mg _16ms_40.84Psi_235mm_301	16ms	A
20	302	O_1.1_F_30mg _14.2ms_40.84Psi_169mm_302	14.2ms	A
21	303	O_1.1_F_23mg _6.5ms_40.84Psi_35mm_303	6.5ms	A
22	304	O_1.1_F_21mg _3.7ms_40.61Psi_31mm_304	3.7ms	A
23	305	O_1.1_F_20mg _0ms_40.68Psi_3mm_305	0ms	A

Table 41: List of experiments for critical air injection mass

Exp. No	Flame code (refer Table 24: Description of the flame code, to understand code)	Air mass (mg)	Position of Tulip (mm)
347	O_1.1_A_18mg _18.3ms_40.65Psi_293mm_347	18	400
345	O_1.1_A_23mg _16.2ms_40.65Psi_206mm_345	23	760
346	O_1.1_A_26mg _14.4ms_40.65Psi_152mm_346	26	1520
342	O_1.1_A_35mg _13.9ms_40.01Psi_112mm_342	35	1160
341	O_1.1_A_38mg _16.7ms_40.83Psi_173mm_341	38	400
340	O_1.1_A_38mg _16.3ms_40.86Psi_189mm_340	38	840
336	O_1.1_A_39mg _12.2ms_41.24Psi_120mm_336	39	1120
343	O_1.1_A_43mg _14.3ms_40.01Psi_290mm_343	43	760
337	O_1.1_A_65mg _11.9ms_60.37Psi_134mm_337	65	440
338	O_1.1_A_91mg _15.2ms_61Psi_146mm_338	91	1250
339	O_1.1_A_141mg _14.2ms_81Psi_180mm_339	141	440

Table 42: List of experiments for air injections with different timing

	Exp.#	Flame Code (refer Table 24: Description of the flame code, to understand code)	Delay Time	Average speed(m/s)
1	232	0_1.1_A_34mg _46.5ms/22.17mg_40.17Psi_232	46.5	17.30
2	234	0_1.1_A_37.5mg _47.9ms/23.22mg_40.14Psi_234	47.9	24.99
3	233	0_1.1_A_34mg _51.6ms/22.64mg_40.23Psi_233	51.60	25.56
4	223	0_1.1_A_35mg _13.6ms/3.87mg_40.21Psi_223	13.60	25.92
5	225	0_1.1_A_33mg _23.3ms/14.06mg_40.13Psi_225	0	26.48
6	247	0_1.1_A_34mg _6.1ms_40Psi_49mm_247	6.1	26.489
7	242	0_1.1_A_33mg _6.1ms_40.09Psi_48mm_242	6.1	26.50
8	227	0_1.1_A_34mg _26.6ms/17.59mg_40.9Psi_227	26.6	26.60
9	235	0_1.1_A_33mg _55.6ms/23.06mg_40.09Psi_235	55.60	26.67
10	221	0_1.1_A_35mg _10.4ms/1.09mg_40.66Psi_221	10.4	26.75
11	229	0_1.1_A_34mg _32.6ms/21.09mg_40.1Psi_229	32.60	26.85
12	229	0_1.1_A_34mg _32.6ms/21.09mg_40.1Psi_229	32.6	26.85
13	229	0_1.1_A_34mg _32.6ms/21.09mg_40.1Psi_229	32.6	26.85
14	231	0_1.1_A_34mg _45.1ms/22.12mg_40.14Psi_231	45.1	26.86
15	240	0_1.1_A_34mg _0.5ms_39.81Psi_5mm_240	4.9	27.14
16	238	0_1.1_A_34mg _7.6ms_40.01Psi_95mm_238	7.6	27.50
17	245	0_1.1_A_34mg _5ms_40.03Psi_50mm_245	5	27.70
18	227	0_1.1_A_34mg _26.6ms/17.59mg_40.9Psi_227	26.6	27.79
19	246	0_1.1_A_33mg _6.9ms_40.01Psi_75mm_246	6.90	28.17
20	243	0_1.1_A_34mg _3.8ms_40.09Psi_36mm_243	3.80	28.24
21	221	0_1.1_A_35mg _10.4ms/1.09mg_40.66Psi_221	14.3	29.29
22	220	0_1.1_A_34mg _10.7ms/5.15mg_39.59Psi_220	10.70	29.52
23	240	0_1.1_A_34mg _0.5ms_39.81Psi_5mm_240	0.50	29.60
24	236	0_1.1_A_34mg _1ms/0.03mg_40.18Psi_236	1	30.14
25	237	0_1.1_A_34mg _5ms_40.14Psi_48mm_237	5.00	32.20
26	230	0_1.1_N_230	4.8	34.22
27	241	0_1.1_A_33mg _1.6ms_39.79Psi_16mm_241	1.6	34.36

E - 7 *List of experiments for mixture injections*

Table 43: List of experiment to investigate displacement of the tulip flame with mixture injections

	Flame Code (refer Table 24: Description of the flame code, to understand code)	Experiment Number
1	O_1.1_M_48mg _20.9ms_29.97Psi_329mm_150	150
2	O_1.1_M_52mg _18.8ms_29.97Psi_259mm_149	149
3	O_1.1_M_54mg _12.7ms_29.95Psi_155mm_153	153
4	O_1.1_M_54mg _18.2ms_32.56Psi_302mm_145	145
5	O_1.1_M_58mg _17.6ms_32.56Psi_216mm_144	144
6	O_1.1_M_60mg _15.7ms_34.61Psi_184mm_139	139
7	O_1.1_M_62mg _14.9ms_40.82Psi_157mm_151	151
8	O_1.1_M_64mg _17.2ms_36.34Psi_198mm_136	136
9	O_1.1_M_70mg _15.4ms_41.25Psi_199mm_138	138
10	O_1.1_M_74mg _12ms_40.64Psi_125mm_152	152
11	O_1.1_M_74mg _19.8ms_40.81Psi_331mm_147	147
12	O_1.1_M_74mg _20.8ms_40.21Psi_364mm_148	148

VITA AUCTORIS

NAME: Indika Gallage

PLACE OF BIRTH: Colombo, Sri Lanka

YEAR OF BIRTH: 1969

EDUCATION: D. S. Senanayaka Collage, Colombo, Sri Lanka
                             (1976-1988),Ordinary Level, 1985; Advanced Level
                             (University Entrance), 1988
                             University of Moratuwa, Sri Lanka (1991-1995),
                             B.Sc. Eng Hons, 1995
                             University of Moratuwa, Sri Lanka (2001-2004),
                             M.Eng. (Energy Technologies), 2004